

Differentiation and crystallisation processes in A-type granites:

An experimental study of the Wangrah Suite, Australia.

Differenzierungs- und Kristallisationsprozesse in A-Typ Graniten:

Eine experimentelle Studie der Wangrah Suite, Australien.

Vom Fachbereich Geowissenschaften und Geographie

der Universität Hannover

zur Erlangung des Grades

DOKTOR DER NATURWISSENSCHAFTEN

Dr. rer. nat.

genehmigte Dissertation

von

Dipl. Min. Kevin Klimm

geboren am 16.12.1973 in Kassel

2004

Referent: Prof. Dr. F. Holtz
Korreferenten: Prof. Dr. W. Johannes
Prof. Dr. P.L. King
Tag der Promotion: 25. Mai 2004

Abstract

This study provides information on differentiation and crystallisation processes based on experimentally determined phase relations of four natural A-type granitic compositions. Each composition is representative for one major granite intrusion of the Wangrah Suite, Lachlan Fold Belt, southeastern Australia. The intrusions are Danswell Creek, Wangrah, Eastwood and Dunskeig Granite (ordered from “most mafic” to “most felsic” by increasing silica contents). The chemical variations of these granites, such as decreases of FeO, MgO, CaO, Ba and Sr with increasing SiO₂ reflect different stages of differentiation in the magmatic history of the Wangrah Suite.

Crystallisation experiments with each composition were performed at 200 MPa, in a temperature range 900-700°C and a fO_2 corresponding to the NNO-buffer to assess the role of H₂O and bulk compositions on phase relations and crystal/melt proportions. The stability fields of plagioclase, quartz and orthopyroxene are shifted to the solidus with decreasing bulk SiO₂ contents of the starting material. Biotite shows the same trend except for the Wangrah Granite composition. Biotite and K-feldspar are stable over the broadest range of temperature and aH₂O in the Wangrah Granite compared to all other granites. All compositions are ~50% crystallised at 750°C and 4-5 wt. % H₂O. Below 50% crystallisation, the crystal contents decrease from the most mafic to the most felsic composition at given P, T, aH₂O conditions. The Dunskeig Granite represents a composition close to the minimum temperature melt composition at a aH₂O between 0.5-0.7 when compared to the synthetic system Qz-Ab-Or-An-H₂O. Experimental results were compared to the natural phase compositions to constrain the water contents of the melts and the phases involved in fractionation processes in the Wangrah Suite.

The Danswell Creek Granite represents a primary waterundersaturated melt with 2.5 ±0.5 wt. % H₂O from which the more evolved granites were derived by crystal fractionation. Although orthopyroxene is not observed in the natural assemblages of the Wangrah Suite, it has influenced the early fractionation of the Wangrah Suite granites. The Eastwood Granite composition is obtained after fractionation of magnetite, orthopyroxene and plagioclase (~20 wt. %) from the Danswell Creek Granite composition and the water content increases to ~3 wt. % H₂O. A composition similar to the Dunskeig Granite is obtained after further fractionation of plagioclase, quartz, K-feldspar and biotite (~40 wt. %) from the Eastwood Granite composition (H₂O ~4.7 wt. % after fractionation). The crystallisation of the highly evolved water undersaturated granites is characterised by a rapid increase of H₂O during cooling resulting in a decrease of viscosity.

Although the most abundant Wangrah Granite composition can nearly be obtained by fractionation of orthopyroxene and plagioclase, the high K₂O content of the Wangrah Granite does not fit the differentiation trend obtained from Danswell Creek over Eastwood to Dunskeig Granite. A magma mixing process of highly crystalline low temperature magma containing substantial amounts of K-feldspar with primary high temperature magma can explain the high K₂O content of this rock and the occurrence of rapakivi-texture.

Keywords: *A-type granite, differentiation, rapakivi-texture*

Zusammenfassung

Diese Arbeit liefert Informationen zu Differenzierungs- und Kristallisationsprozessen in A-typ granitischen, magmatischen Systemen anhand von experimentell untersuchten Phasenbeziehungen von vier natürlichen A-typ granitischen Zusammensetzungen. Jede dieser vier Zusammensetzungen steht repräsentativ für eine von insgesamt vier Granitintrusionen der Wangrah Suite, Teil des Lachlan Orogens im Südosten von Australien. In der Reihenfolge des zunehmenden Silikatgehaltes handelt es sich dabei um den Danswell Creek, Wangrah, Eastwood und Dunskeig Granit. Die chemischen Variationen dieser Gesteine, wie abnehmende FeO, MgO, CaO, Ba und Sr Gehalte mit zunehmendem SiO₂-Gehalte, sind das Resultat von Differenzierungsprozessen und repräsentieren unterschiedliche Stadien in der magmatischen Differenzierung der Wangrah Suite.

Mit jeder der vier Zusammensetzungen wurden Kristallisationsexperimente bei 200 MPa, zwischen 900 bis 700°C und Sauerstoff fugazitäten entsprechend dem Ni-NiO-Puffer durchgeführt, um den Einfluss von Wasser und Ausgangszusammensetzung auf die Phasenbeziehungen und Kristall/ Schmelz-Verhältnisse zu ermitteln. Die Stabilitätsfelder von Plagioklas, Quarz und Orthopyroxen verschieben sich in Richtung des Solidus mit abnehmendem SiO₂-Gehalte der Ausgangszusammensetzung. Bis auf Experimente mit dem Wangrah Granit zeigt Biotit den gleichen Trend. Im Vergleich zu allen anderen Graniten sind Biotit und K-Feldspat in den Experimenten mit dem Wangrah Granit über den größten Temperatur- und Wassergehaltbereich der Schmelze stabil. Alle Zusammensetzungen sind bei 750°C und 4-5 Gew. % zu ca. 50% auskristallisiert. Unterhalb eines Kristallgehaltes von 50% verschieben sich die Kurven gleichen Kristallgehaltes zum Solidus mit gleichzeitig abnehmendem SiO₂-Gehalte der Ausgangszusammensetzung. Der Dunskeig Granit ist in seiner Zusammensetzung nahe der Minimumzusammensetzung im synthetischen System Qz-Ab-Or-an-H₂O bei einer Wasseraktivität zwischen 0.5-0.7. Die experimentellen Ergebnisse dieser Arbeit wurden mit den natürlichen Zusammensetzungen verglichen, um die Wassergehalte der Schmelzen und die Phasen, die in Kristallfraktionierungsprozesse involviert sind, zu bestimmen.

Der Danswell Creek Granit repräsentiert die wasseruntersättigte Primärschmelze mit einem Wassergehalt von 2.5 ± 0.5 Gew. % von der die mehr entwickelten Granite durch Kristallfraktionierung gebildet wurden. Obwohl Orthopyroxen in den natürlichen Gesteinen nicht auftritt, ist dieses Mineral Teil der ersten Fraktionierungsprozesse. Die Zusammensetzung des Eastwood Granites ist nach einer Fraktionierung von ~20 Gew. % Magnetit, Orthopyroxen + Plagioklas erreicht. Dadurch wird der Wassergehalt auf ~3 Gew. % angereichert. Eine weitere Fraktionierung von ~40 Gew. % Plagioklas, Quarz, K-Feldspat + Biotit ausgehend vom Eastwood Granit führt zur Dunskeig Granit Zusammensetzung und einer Wasseranreicherung auf ~4.7 Gew. %. Die Kristallisation der hoch entwickelten Wasser untersättigten Granite ist durch einen schnellen Anstieg des Wassergehaltes und einer dadurch bewirkten Erniedrigung der Viskosität gekennzeichnet.

Der Wangrah Granit passt mit seinem hohen K₂O-Gehalt nicht in den Differenzierungstrend vom Danswell Creek → Eastwood → Dunskeig Granit, obwohl eine Modellierung einer Orthopyroxen + Plagioklas Fraktionierung nahe an die Zusammensetzung des Wangrah Granites ist. Der hohe K₂O Gehalt und das Auftreten einer Rapakiwi-Textur in den natürlichen Gesteinen favorisieren einen Magmenmischungsprozess zwischen einem hoch entwickelten, teilkristallinen und niedrig temperierten Magma mit einem Schub hoch temperiertem primärem Magma. Das niedrig temperierte Magma muss zusätzlich eine beträchtliche Menge K-Feldspat führen, was bei den Kristallisationsexperimenten mit dem Dunskeig Granit nachgewiesen werden konnte.

Schlagerwörter: A-Typ Granit, Differenzierung, Rapakiwi-Textur

Danksagung

Die vorliegende Arbeit wurde am Institut für Mineralogie der Universität Hannover durchgeführt unter der Leitung von Prof. Dr. F. Holtz. Bei ihm möchte ich mich ausdrücklich herzlich für die interessante Aufgabenstellung, die zahlreichen Diskussionen und die intensive Betreuung bedanken. Mit seinem enormen Hintergrundwissen hat er mich in entscheidenden Phasen wieder fokussiert.

Bei Prof. Dr. W. Johannes möchte ich mich für die Übernahme des Koreferates und der Initiierung des Projektes bedanken.

Many thanks to Dr. Penny King for the scientific discussions and the quick help with questions and Bruce Chappell for providing the natural samples.

Vielen, vielen Dank an Otto Diedrich, der mich mit seiner Geschwindigkeit und Präzision der Probenpräparation immer wieder beschämt hat. Ebenso vielen Dank auch an Willi Hurkuck und Bettina „Werkstattmaus“ Aichinger für die technische Unterstützung.

Jürgen Koepke, Matthias Hahn und Magnus Johansson danke ich für die Unterstützung an der Mikrosonde.

Bei Antje Wittenberg, Fleurice Parat, und Markus Nowak möchte ich mich für Ihr Interesse und der Erkenntnis, dass da alle durch müssen, bedanken.

Dank auch an Marcus Freise für den fast 10-jährigen gemeinsamen Weg, und dass man sich auf Dich verlassen kann.

Dominik, Fred, Piero, Francesco, Marc, und Ronnie danke ich für das ein oder andere, rein wissenschaftliche, Pils.

Kuss und Gruß an Antje, die mich mit großem Verständnis häufig aus 6 km geistiger Tiefe sanft zum Boden der Realität zurück geführt hat.

Table of contents

1. Experimental determination of phase relations in A-type granites: The conditions of the primary magma and the beginning of differentiation ...	1
1.1. Introduction	1
1.2. Granites of the Wangrah Suite and starting material	3
1.3. Experimental techniques	6
1.4. Experimental results	10
1.4.1. Phase relations	10
1.4.2. Phase compositions	11
1.4.3. Plagioclase	12
1.4.4. Orthopyroxene	13
1.4.5. Hornblende and biotite	14
1.5. Discussion	15
1.5.1. Determination of initial water content in A-type melts of the Wangrah Suite	15
1.5.2. Role of orthopyroxene	16
1.5.3. Differentiation by fractional crystallisation	18
1.5.4. Stability of hornblende	19
1.6. Conclusions	21
2. Differentiation processes in A-type granites: Crystal fractionation vs. magma mixing.....	23
2.1. Introduction	23

2.2. Granites of the Wangrah Suite and starting material	25
2.3. Methods and experimental techniques	29
2.4. Experimental results	34
2.4.1. Phase relations	34
2.4.2. Phase compositions	36
2.4.3. Phase proportions	45
2.5. Discussion and applications of experimental results	48
2.5.1. Comparison of experimentally determined phase relations	48
2.5.2. Projection of natural compositions in the ternary system and implications for the crystallisation sequence	51
2.5.3. Differentiation by fractional crystallisation	54
2.5.4. Crystallisation and differentiation paths of the Wangrah Suite	60
2.5.5. Viscosity of melts	63
2.5.6. Crystallisation of the Wangrah granite AB422	65
2.6. Conclusions: Crystal fractionation vs. magma mixing	74
3. References	77

1. Experimental determination of phase relations in A-type granites: The conditions of the primary magma and the beginning of differentiation

1.1. Introduction

Metaluminous to weakly peraluminous A-type granites are characterized by high SiO₂, Ga/Al, Fe/Mg, Zr, Nb, Y and REE (except Eu) and low CaO, (Loiselle & Wones, 1979; Collins et al., 1982; Whalen et al., 1987; King et al., 1997). This discrimination is clear for the less evolved A-type granites, but the more felsic, fractionated A-type granites (SiO₂ > 72 wt. %) have chemical characteristics that are similar to felsic, fractionated I-type granites (King et al., 1997; King et al., 2001). In contrast to I-type granites with similar SiO₂ contents, A-type granites contain Fe-rich mafic minerals.

Both the chemistry and mineralogy of A-type granites are likely influenced by the source rock composition (e.g., fluid-absent; Creaser et al., 1991) and conditions such as high temperature, low pressure and/or oxygen fugacity (fO_2) (Anderson & Bender, 1989; King et al., 1997; Patiño Douce, 1997; Dall'Agnol et al., 1999). A-type granitic magmas can have water contents of several wt. %, like other types of granitic magmas (Clemens et al., 1986; King et al., 1997; Dall'Agnol et al., 1999), although the water content of the source is likely low. Generally, they evolved under relatively reduced conditions with fO_2 less than the nickel-nickel oxide buffer ($fO_2 < NNO$; Frost & Frost, 1997; King et al., 1997), but relatively oxidized A-type granites are known also (Anderson & Bender, 1989; Dall'Agnol et al., 1999). Consequently the fractionation paths of granitic systems depend strongly on both the prevailing water activity (aH_2O) and fO_2 (e.g., Dall'Agnol et al., 1999).

Crystal fractionation is likely one of the major differentiation mechanism in A-type granitic systems (Collins et al., 1982; Clemens et al., 1986; Chappell et al., 1987; Whalen et al., 1987; Creaser et al., 1991; King et al., 1997; King et al., 2001). However, the influence of aH_2O and

fO_2 on the phase relations of A-type granitic magmas is poorly known and has been examined in only two experimental studies (Clemens et al., 1986; Dall'Agnolet al., 1999).

Clemens et al. (1986) determined phase relations of a felsic amphibole-bearing A-type granite from southeastern Australia. The experiments were conducted at 100 MPa, 725 to 1000°C and fO_2 0.3 log units above the fayalite-magnetite-quartz buffer (FMQ+0.3). They suggested that the experiments indicated that A-type granites melt at ~830°C at 100 MPa, with an initial water content of 2.4 to 4.3 wt. %. However, in these experiments amphibole did not crystallise and an unusual 'cusp' was observed for the plagioclase out curve. Dall'Agnolet al. (1999) conducted phase-equilibrium experiments on an A-type granite from the eastern Amazonian craton (Brazil) at 300 MPa, 700 to 900°C and for fO_2 s of NNO+2.5 and NNO-1.5. Dall'Agnolet al. (1999) concluded that the melt temperature was in the range of 800 to 870°C, with an initial water content of 4.5 to 6.5 wt. % and slightly oxidizing fO_2 conditions of ~NNO+0.5. They also demonstrated that Fe-rich mafic minerals are favoured at lower temperatures and lower fO_2 .

Both experimental studies were performed with only one composition of the chosen A-type granitic plutons. Because fractionation processes lead to the formation of different bulk granitic compositions within one suite, these experimental results provide only information on one part of the crystallisation history. Thus, the phase relations in compositions representing different stages of fractionation were not examined. To understand the evolution of A-type granites it is necessary to examine several chemical compositions within one suite. This paper presents new experimental results on phase relations in A-type granitic compositions representing different fractionation stages of the Wangrah Suite (south eastern Australia, LFB). The chemical variation among the granites from the Wangrah Suite likely result from fractional crystallisation processes, based on trace element abundances. King et al. (2001) proposed that fractional crystallisation of plagioclase and mafic minerals could account for the chemistry of the suite, combined with

reactions involving mafic minerals (e.g., pyroxene \rightarrow amphibole \rightarrow biotite). The experimental results are used to clarify the processes of evolution of an A-type granitic magma.

1.2. Granites of the Wangrah Suite and starting material

The geology, petrology and geochemistry of the granites from the Wangrah Suite have been described by King et al. (2001). Within the LFB, the Wangrah Suite is a typical A-type granitic association. Four representative analyses of granites from the Wangrah Suite are listed in Table 1.1. The chemical variations, such as decreases in Ba and Sr with increasing SiO_2 , are likely the result of crystal fractionation from an initial composition close to that of AB412 at 100 to 200 MPa, with H_2O contents of the melt in the range 2-5 wt. % (King et al., 2001). Figure 1.1 shows the fractionation trend of decreasing MgO and CaO contents with increasing SiO_2 contents of different granite samples from the Wangrah Suite.

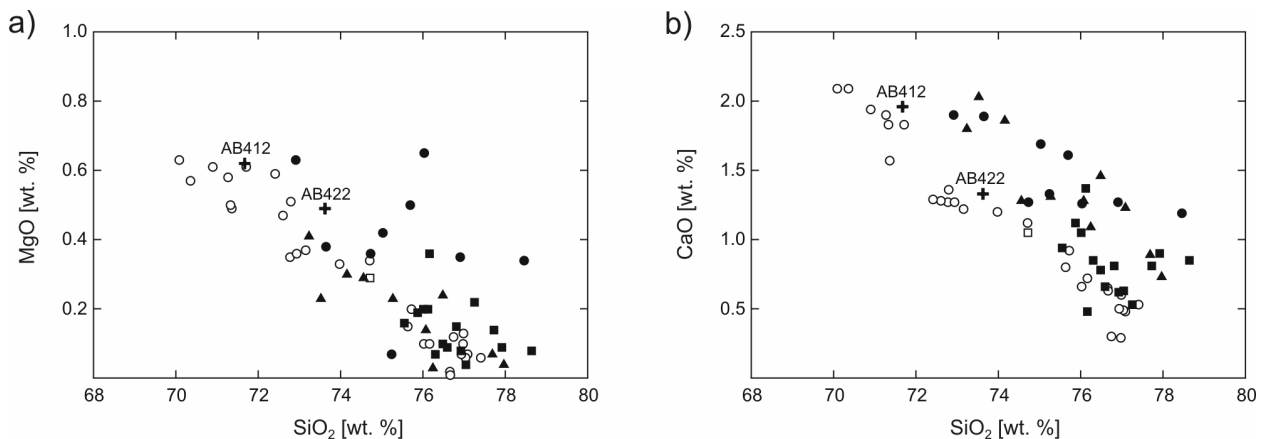


Figure 1.1: Harker-diagram of a) MgO and b) CaO versus SiO_2 . Symbols: open circles = A-type granites from the Wangrah Suite (after King, 1992; King et al., 2001); open square = average of 55 A-type samples from LFB after King et al. (1997); crosses = A-type samples, used as starting material in this study; filled symbols = composition of glasses from experiments with a melt H_2O content of >6 wt. % (filled circles), 4 to 6 wt. % (filled triangles) and <4 wt. % (filled squares).

Within a suite K_2O and Na_2O actually do not change much (Table 1.1). Zircon saturation temperatures were calculated after Watson & Harrison (1983) as 897°C for the more mafic composition AB412, 843°C for AB422 and 764°C for the most felsic composition AB401. The

fO_2 was calculated to be in the range of NNO-2.4 to NNO-4.7. It can be noted that the method used to calculate fO_2 in the natural samples assumed that the biotite had not re-equilibrated and therefore they were minimum estimates.

Table 1.1: Compositions of natural rocks and synthesized glasses

	Wangrah-Suite									
	Natural ¹				Normalized					
	AB412	AB422	AB421	AB401	AB412			AB422		
				Natural ¹	glass	σ	Natural ¹	glass	σ	
<i>wt. %</i>					n=10			n=11		
SiO ₂	70.45	72.53	75.32	76.67	71.67	71.89	0.40	73.62	73.85	0.44
TiO ₂	0.54	0.37	0.15	0.09	0.55	0.55	0.04	0.38	0.38	0.05
Al ₂ O ₃	13.26	13.08	12.71	12.10	13.49	13.60	0.11	13.28	13.42	0.17
FeO	4.06	2.50	1.62	0.92	4.13	4.14	0.15	2.54	2.58	0.13
MnO	0.08	0.05	0.06	0.02	0.08	0.07	0.06	0.05	0.05	0.04
MgO	0.61	0.48	0.23	0.05	0.62	0.62	0.02	0.49	0.46	0.01
CaO	1.93	1.31	0.90	0.53	1.96	1.96	0.02	1.33	1.32	0.06
Na ₂ O	3.39	3.32	3.36	3.25	3.45	3.38	0.10	3.37	3.34	0.14
K ₂ O	3.98	4.88	4.61	5.12	4.05	3.79	0.11	4.95	4.62	0.10
P ₂ O ₅	0.18	0.12	0.05	0.01	-	-		-	-	
rest	0.23	0.17	0.12	0.09	-	-		-	-	
Total	98.71	98.81	99.13	98.85	100.00	100.00		100.00	100.00	
<i>ppm</i>										
F	n.d.	1040	670	n.d.						
Rb	146	228	216	187						
Sr	128	87	56	14						
Ba	505	215	148	61						
Zr	535	313	190	116						
Nb	26	21	20	11						
Ga	22.2	21.2	19.6	22.4						
Y	75	64	77	125						
La	64	53	28	24						
Ce	145	121	63	64						
Sm	14.2	10.2	8.6	15.3						
Eu	2.85	1.40	1.15	0.71						
Yb	7.8	7	8.6	12.8						
Zn	81	52	52	28						
Zr-sat. T [°C] ²	897	843	806	764						

¹ Source of data: King et al. (2001): AB412 sample of Danswell Creek granite; AB422 sample of Wangrah granite; AB421 sample of Eastwood granite; AB401 sample of Dunskeig granite.

² Calculated zircon saturation temperatures after Watson & Harrison (1983).

The compositions chosen as starting material for the experiments were AB412 and AB422. AB412 comes from Danswell Creek granite and AB422 comes from the Wangrah granite which are part of the Wangrah Suite (King et al, 2001). Both granites contain hornblende, biotite, ilmenite, zircon and apatite. AB412 also contains minor titanite. The occurrence of hornblende in AB422 is variable, but generally less than 3 modal percent. Anorthite contents of plagioclase cores are An₃₀ or less for AB412 and AB422. The amount of hornblende decreases from AB412 to AB422. The compositions of plagioclase and hornblende are given in Tables 1.2 and 1.3, respectively.

Table 1.2: Representative compositions of natural and experimental plagioclase

Sample	Natural				Experimental			
	AB412		AB422		AB412		AB422	
Run/T [°C]	core	rim	core	rim	35/850	29/800	36/850	30/800
cH ₂ O [wt. %] ¹					2.6	3.8	2.5	3.9
logfO ₂ [ΔNNO]					-0.59	-0.30	-0.60	-0.30
<i>wt. %</i>								
SiO ₂	62.07	63.82	61.92	64.40	61.15	60.59	63.70	64.00
Al ₂ O ₃	23.98	22.96	22.96	22.68	23.93	22.53	21.76	23.53
Fe ₂ O ₃	0.16	0.09	0.09	0.13	1.22	1.73	0.58	0.43
CaO	5.47	4.26	4.26	3.64	5.94	5.8	5.37	5.18
Na ₂ O	8.82	9.63	7.77	8.88	6.59	6.84	5.92	6.93
K ₂ O	0.24	0.17	0.35	0.39	1.01	1.06	1.61	1.37
Total	100.74	100.93	99.92	100.12	100.14	99.10	99.12	101.52
<i>Structural formula (8O)</i>								
Si	2.739	2.800	2.746	2.834	2.727	2.746	2.847	2.794
Al	1.247	1.187	1.261	1.176	1.258	1.204	1.146	1.211
Fe ³⁺	0.005	0.003	0.003	0.004	0.041	0.059	0.020	0.014
Ca	0.259	0.200	0.269	0.172	0.284	0.282	0.257	0.243
Na	0.755	0.819	0.668	0.758	0.570	0.601	0.513	0.587
K	0.014	0.010	0.020	0.022	0.058	0.062	0.091	0.076
<i>mol %</i>								
An	25.2	19.5	28.1	18.0	31.2	29.8	29.8	26.8
Ab	73.5	79.5	69.8	79.7	62.5	63.7	59.5	64.8
Or	1.3	0.9	2.1	2.3	6.3	6.5	10.6	8.4

¹ Concentration of water in the residual glass after experiment.

Table 1.3: Representative compositions of natural and experimental hornblende

Sample	Natural		Experimental					
	AB412	AB422	AB412					
Run/T [°C]			1/800	25/800	7/800	13/750	23/750	15/700
cH ₂ O [wt. %] ¹			6.4	5.2	4.6	6.2	5.2	6.5
logfO ₂ [ΔNNO]			±0	-0.09	-0.19	±0	-0.19	±0
<i>wt. %</i>								
SiO ₂	43.33	42.63	47.21	44.74	45.30	46.64	49.21	44.90
TiO ₂	1.02	1.30	0.96	1.39	0.94	1.07	0.86	1.05
Al ₂ O ₃	8.27	8.26	7.19	8.21	8.11	7.38	6.95	8.84
FeO	28.67	27.48	16.95	17.53	21.41	19.10	20.65	21.81
MnO	1.17	0.97	0.60	0.49	0.59	0.55	0.66	0.76
MgO	4.46	4.50	12.43	10.79	9.10	10.57	7.88	8.03
CaO	10.00	11.02	10.01	9.79	8.39	10.06	8.05	10.35
Na ₂ O	1.56	1.45	1.42	1.45	1.49	1.39	1.32	1.41
K ₂ O	0.91	1.14	0.40	0.50	0.55	0.54	0.67	0.68
H ₂ O	1.92	1.91	2.01	1.95	1.94	1.99	1.98	1.96
Total	101.31	100.66	99.18	96.84	97.82	99.29	98.23	99.79
<i>Structural formula (23O)</i>								
Si	6.769	6.703	7.044	6.884	6.988	7.027	7.451	6.850
Al	1.522	1.531	1.265	1.489	1.474	1.311	1.241	1.590
Fe	3.745	3.613	2.116	2.257	2.762	2.415	2.615	2.782
Mg	1.039	1.055	2.765	2.476	2.093	2.374	1.778	1.826
Mn	0.155	0.129	0.076	0.063	0.077	0.070	0.084	0.098
Ti	0.120	0.154	0.108	0.161	0.109	0.121	0.098	0.121
Ca	1.674	1.857	1.600	1.614	1.386	1.623	1.306	1.692
Na	0.472	0.442	0.411	0.434	0.111	0.407	0.387	0.416
K	0.181	0.229	0.076	0.098	0.108	0.103	0.129	0.133
XMg	0.22	0.23	0.57	0.52	0.43	0.50	0.40	0.40

¹ Concentration of water in the residual glass after experiment.

1.3. Experimental techniques

The natural rock powders (AB412 and AB422) were melted twice in a Pt crucible at 1600°C and 1 atm, with grinding between the two melting steps. The glass compositions were determined by electron microprobe analysis and are similar to the natural rock composition (Table 1.1). The anhydrous glasses were ground down manually in an agate mortar. 90 wt. % glass and 10 wt. % ±0.2 fluid were loaded in welded gold capsules. The amount of added fluid was low to avoid undesirable effects of incongruent dissolution of silicate in the fluid. The water activity (aH₂O) of the experimental charges was varied by adding a fluid composed of a mixture

of H₂O and CO₂. CO₂ was added as silver oxalate (Ag₂C₂O₄). The mole fraction of water in the added fluid phase was varied in a range of $X_{H_2O_{initial}} = 0.4$ to 1.0. It is emphasized that this $X_{H_2O_{initial}}$ is different from the final X_{H_2O} because H₂O is preferential dissolved in silicate melts.

Crystallisation experiments, covering the temperature interval 700 to 850°C, were performed at 200 MPa in cold seal pressure vessels (CSPV) with water as the pressure medium. The high temperature experiments at 900°C were performed in an internally heated pressure vessel (IHPV) equipped with an H₂ membrane developed by Berndt et al. (2002) and an Ar-H₂ mixture as the pressure medium. Run duration varied with temperature: 32 days for runs at 700 and 750 °C, 8 days at 800 and 850°C, and 6 days at 900°C. The oxygen fugacity (fO_2) was monitored by adding a solid Ni-NiO buffer in the vessel for experiments conducted with CSPV. These vessels are made of Ni-alloy, which allows to perform long run duration with the solid buffer technique at $fO_2 = NNO$. In the IHPV experiments, the fO_2 was controlled by loading 2 bars H₂ and 960 bars Ar in the vessel at room temperature. The final total pressure at 900°C was 1930 bars and the partial pressure of H₂ was 10.2 bars (measured with the Shaw membrane). The fO_2 was calculated using the H₂O dissociation constant of Robie et al. (1978), fugacity coefficients for H₂ from Shaw & Wones (1964) and for H₂O from Burnham et al. (1969). Because water activity and water fugacity (f_{H_2O}) varies in the experiments (as a function of the mole fraction of water in the charge), fO_2 is not strictly constant at given P and T. In our experiments fO_2 ranges from NNO to NNO-1.05 (see Tables 1.4 and 1.5).

After the runs, a H-O or a H-O-C fluid phase was detected qualitatively in all charges by weight loss and freezing in a cold trap cooled by liquid nitrogen (for CO₂) and weight loss after heating up to 105°C (for H₂O). However, because of the too low amount of added fluid, the final X_{H_2O} of the fluids after the experiments could not be analysed quantitatively by this method. The phases were identified and their compositions were determined by electron microprobe

(Cameca SX 100 at the University of Hannover). Crystalline phases were analysed with 15 kV acceleration voltage, 10 nA sample current and 10 s total counting time. Analytical conditions for glasses to minimize the migration of alkali during glass analysis were 15 kV, 6 nA and 5 s total counting time and the beam was defocused up to 20 μm when possible (lowest value was 5 μm , Na was measured first). The H_2O contents of the glasses were estimated with microprobe analyses following the difference method described by Devine et al (1995).

Table 1.4: Experimental results for the composition **AB412** at 200 MPa and $\log f_{\text{O}_2} \sim \text{NNO}$

Run	T [°C]	Duration [days]	$\text{XH}_2\text{O}_{\text{in}}^1$	Results (+ Gl, Fl, Fe-Ti oxide) ²	cH_2O in glass (wt. %) ³	$\text{cH}_2\text{O}_{\text{calculated}}$ (wt. %) ⁴	ΔNNO^5
15	700	32	1.00	Hbl, Bt, Pl (An28.1Or4.3), (Mnz)	6.5	6.36	± 0
21	700	32	0.80	Bt, Pl (An20.4Or8.1), Kfs (An1.7Or72.7), Qz	5.1	-	-0.19
13	750	32	1.00	Hbl, Bt, Pl (An39.7Or2.6), (Mnz), (Zrn)	6.2	6.28	± 0
23	750	32	0.80	Hbl, Bt, Pl (An30.3Or5.8), Qz	5.2	-	-0.19
43	750	8	0.70	Opx (En29.6Wo5.2), Bt, Pl (An26.0Or5.8), Qz	4.5	-	-0.31
1	800	8	1.00	Hbl, Bt, (Mnz)	6.4	6.20	± 0
25	800	8	0.90	Hbl, Bt, Pl (An39.2Or3.7), (Mnz)	5.2	-	-0.09
7	800	8	0.80	Hbl, Bt, Pl (An36.1Or3.6)	4.6	-	-0.19
29	800	8	0.71	Opx (En35.3Wo4.7), Bt, Pl (An29.8Or6.5), Qz	3.8	-	-0.30
11	800	8	0.60	Opx (En34.9Wo4.6), Bt, Pl (An25.3Or9.4), Kfs (An3.6Or66.7), Qz	3.3	-	-0.44
33	800	8	0.50	Opx (En27.4Wo6.2), Bt, Pl (An20.9Or12.5), Kfs (An3.2Or63.1), Qz	2.8	-	-0.60
3	850	8	1.00	Opx (En52.0Wo2.6)	6.2	6.12	± 0
27	850	8	0.90	Opx (En51.8Wo2.7)	5.2	-	-0.09
5	850	8	0.80	Opx (En46.7Wo3.3), Pl (An46.7Or3.3)	4.7	-	-0.19
31	850	8	0.71	Opx (En42.6Wo5.1), Pl (An36.4Or11.4)	3.4	-	-0.30
9	850	8	0.59	Opx (En33.5Wo5.5), Pl (An33.7Or6.5)	3.1	-	-0.46
35	850	8	0.51	Opx (En32.6Wo4.1), Pl (An31.2Or6.3)	2.6	-	-0.59
19	850	8	0.38	Opx (n.a.), Pl (An22.9Or12.2), Kfs (An3.8Or58.7)	1.8	-	-0.84
39 ⁶	900	6	1.00		6.0	6.04	-0.30
40 ⁶	900	6	0.69	Opx (En45.5Wo4.9)	3.9	-	-0.62
41 ⁶	900	6	0.42	Opx (En38.3Wo4.3), Pl (An39.0Or5.8)	1.8	-	-1.05

¹ $\text{XH}_2\text{O}_{\text{in}} = \text{H}_2\text{O}/(\text{H}_2\text{O} + \text{CO}_2)$ loaded in the capsule (in moles).

² Phases present in run products. Phases in parentheses: accessory Minerals identified by backscattered electron microscopy. Mineral abbreviations as given by Kretz (1983). Ilmenite and/or titanomagnetite plus glass and fluid are present in all runs. n.a. = not analyzed due to small grain size.

³ Water contents of glasses determined using the difference method (Devine et al., 1995). Numbers in italics indicate charges in which the melt water content was estimated using results of other charges with similar $\text{XH}_2\text{O}_{\text{in}}$.

⁴ Water solubilities for water saturated conditions after Holtz et al. (2001), calculated with a water solubility of 6.20 wt. % H_2O at 800°C, 200 MPa and a temperature dependence for water solubility of -16×10^{-4} wt. % $\text{H}_2\text{O}/^\circ\text{C}$.

⁵ $\Delta\text{NNO} = \log f_{\text{O}_2}(\text{experiment}) - \log f_{\text{O}_2}(\text{NNO})$ (Chou, 1987). For water saturated experiments at temperatures between 700 and 850°C in the CSPV the $f_{\text{O}_2} = \text{NNO}$. For the water saturated experiment at 900°C in the IHPV the f_{O_2} is calculated by using the equation $f_{\text{O}_2} = (f_{\text{H}_2\text{O}}/(K_w \times P_{\text{H}_2}))^2$ with $f_{\text{H}_2\text{O}}$ from Burnham et al. (1969), K_w from Robie et al. (1978) and the experimental P_{H_2} . For H_2O -undersaturated charges, a maximum possible f_{O_2} is calculated as $\log f_{\text{O}_2} = \log f_{\text{O}_2}(\text{aH}_2\text{O}=1) + 2\log \text{XH}_2\text{O}_{\text{in}}$.

⁶ $P_{\text{total}} = 193 \text{ MPa}$; $P_{\text{H}_2} = 10.2 \text{ bar}$.

Table 1.5: Experimental results for the composition **AB422** at 200 MPa and $\log f_{\text{O}_2} \sim \text{NNO}$

Run	T [°C]	Duration [days]	XH ₂ O _m ¹	Results (+ Gl, Fl, Fe-Ti oxide) ²	cH ₂ O in glass (wt. %) ³	cH ₂ O _{calculated} (wt. %) ⁴	ΔNNO ⁵
16	700	32	1.00	Bt, (Mnz)	6.4	6.36	±0
22	700	32	0.80	Bt, Pl (An17.4Or9.3), Kfs (An0.9Or71.9), Qz	5.1	-	-0.19
14	750	32	1.00	Bt, (Mnz)	6.4	6.28	±0
24	750	32	0.79	Bt, Pl (An24.5Or7.7), Kfs (An1.9Or74.1), Qz	5.1	-	-0.20
2	800	8	1.00	Bt, (Mnz)	6.2	6.20	±0
26	800	8	0.90	Bt	5.2	-	-0.09
8	800	8	0.79	Bt, Pl (An32.3Or6.7)	4.5	-	-0.20
30	800	8	0.71	Opx (En31.6Wo6.8), Bt, Pl (An26.8Or8.4)	3.9	-	-0.30
12	800	8	0.59	Opx (n.a.), Bt, Pl (An20.6Or12.8), Kfs (An3.2Or68.6)	3.3	-	-0.46
34	800	8	0.50	Opx (n.a.), Bt, Pl (n.a.), Kfs (n.a.), Qz	2.5	-	-0.60
4	850	8	1.00	Bt, (Mnz)	6.2	6.12	±0
28	850	8	0.90	Opx (En53.7Wo2.1), Bt	5.2	-	-0.09
38	850	8	0.81	Opx (En47.6Wo2.9), Bt	4.5	-	-0.18
37	850	8	0.69	Opx (En39.7Wo5.9), Bt, Pl (An39.2Or6.2)	3.8	-	-0.32
10	850	8	0.60	Opx (En39.0Wo5.8), Pl (An32.5Or7.5)	3.2	-	-0.44
36	850	8	0.50	Opx (n.a.), Pl (An29.8Or10.6)	2.5	-	-0.60
20	850	6	0.40	Opx (n.a.), Pl (n.a.), Kfs (An3.1Or63.1), Qz	1.8	-	-0.80

¹⁻⁵ see footnote Table 4.

Six hydrous rhyolitic glasses (with 0.2 to 7.15 wt. % H₂O) whose H₂O contents were determined by Karl Fischer titration with an uncertainty of ±0.15 wt. % H₂O (Holtz et al., 1995) were used as standard glasses. The standard glasses and the experimental glasses were measured during the same analytical session. The precision of the method can be tested for water saturated experiments. The results obtained by the difference method are identical within ±0.2 wt. % H₂O to water solubilities at 200 MPa determined in subaluminous rhyolitic glasses (water solubility calculated after Holtz et al., 2001; for comparison see Tables 1.4 and 1.5). In experiments with a high crystal content, the glasses could not be analysed correctly. In this case, the water contents (given in italics in Tables 1.4 and 1.5) have been estimated using results of other charges with similar XH₂O_{initial}.

The high temperature run 39 was checked for iron-loss of the sample to the Au-capsule by mass balance calculations. The calculations show that no significant iron-loss occurred in agreement with observations in experiments with more iron-rich compositions (e.g. hydrous

basalts) at much higher temperatures and $fO_2 \leq NNO$ (1050°C; Spulber & Rutherford, 1983; Sisson & Grove, 1993).

1.4. Experimental results

1.4.1. Phase relations

Details concerning the experimental conditions and run products are listed in Tables 1.4 and 1.5. The results of the crystallisation experiments are shown in phase diagrams (Figure 1.2). The phase diagrams are isobaric T- cH_2O_{melt} sections where cH_2O_{melt} is the H_2O content (determined by microprobe) of the coexisting melt in weight percent. The solidus curve and the water-saturation curve have been drawn on the basis of the experimental results in the subaluminous granitic system (Holtz et al., 2001).

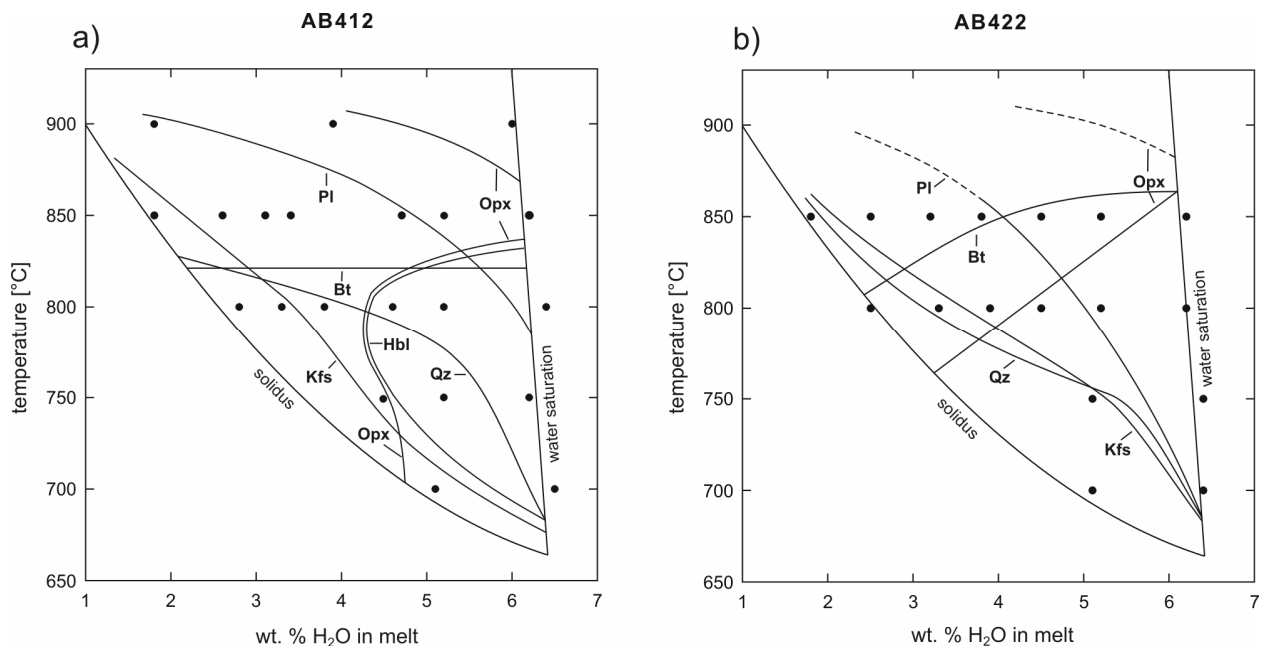


Figure 1.2: Temperature – melt H_2O content phase diagram at 200 MPa and $fO_2 \sim NNO$ for a) composition AB412 and b) composition AB422. Mineral abbreviations as given by Kretz (1983). Stability curves are labelled with mineral names lying inside their stability field. Uncertain portions of stability curves are indicated by dashed lines. Titanomagnetite is present in all runs.

For both compositions, orthopyroxene and Fe-Ti oxides are the liquidus phases. On the basis of our experiments it is difficult to distinguish whether orthopyroxene or oxide are on the liquidus (except for composition AB412 at $a_{\text{H}_2\text{O}} = 1$ where oxide crystallises before orthopyroxene; see Figure 1.2). The orthopyroxene stability is mainly restricted to high temperatures above 750°C. Orthopyroxene may also be observed at lower temperature but only close to the solidus and at water undersaturated conditions. In both compositions K-feldspar is a near-solidus phase.

In the less evolved composition AB412, liquidus conditions have only been obtained at 900°C. The crystallisation of orthopyroxene is followed by that of plagioclase and biotite (except for melts with very high water contents). At high temperatures $\geq 900^\circ\text{C}$ the plagioclase stability is limited to melts with low H_2O contents (≤ 2 to 3 wt. %). Biotite occurs at temperatures below 850°C. Within the resolution of our experiments, the stability of biotite is independent of the water content (or $a_{\text{H}_2\text{O}}$) of the coexisting melt and is only limited by the temperature. Hornblende is observed up to temperatures of 800 to 850°C and in melts with H_2O contents greater than 4 to 5 wt. %. The hornblende stability field does not extend to the solidus.

When compared to AB412 the plagioclase stability curve in AB422 is shifted to lower temperatures and to melts with lower H_2O contents. Plagioclase has not been observed at H_2O -saturated conditions in AB422. As in AB412, biotite stability in AB422 is only slightly dependent on $a_{\text{H}_2\text{O}}$. However, it is slightly shifted to higher temperatures ($>850^\circ\text{C}$) for melt H_2O contents >4 wt. %. No hornblende has been observed.

1.4.2. Phase compositions

In this study the near-liquidus phases (orthopyroxene and plagioclase) crystallise at temperatures close to the zircon saturation temperatures of the samples (Table 1.1), thus these phases are likely involved in crystal fractionation. The coexisting melt compositions and the

composition of biotite and hornblende are of special interest because we wanted to investigate the effect of changing $a_{\text{H}_2\text{O}}$ and f_{O_2} on their compositions. Fe-Ti oxides are present in all runs. Due to the small grain size ($\leq 1 \mu\text{m}$), ilmenite or titanomagnetite or both could be identified only qualitatively.

1.4.3. Plagioclase

The composition of plagioclase depends on $a_{\text{H}_2\text{O}}$ and temperature. Representative plagioclase analyses are listed in Table 1.2. In Figure 1.3 the anorthite (An) content of the experimental plagioclase is presented as a function of the H_2O content of the coexisting melt and temperature.

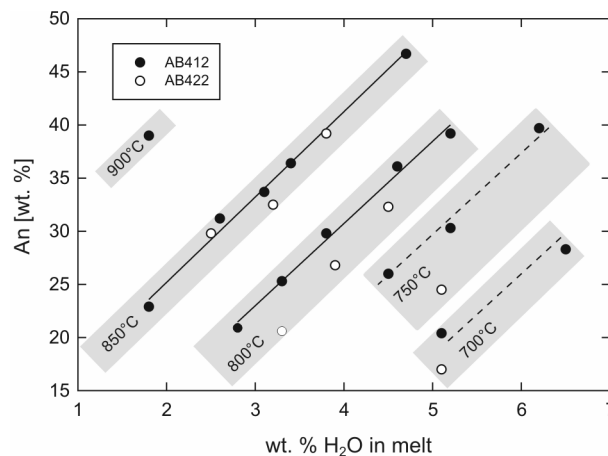


Figure 1.3: An content of experimental plagioclase as a function of melt H_2O content and temperature. Solid lines are linear fits for AB412 at 800 and 850°C. Dashed lines for 700 and 750°C have been constructed considering that the linear fits for given T are parallel in the diagram. Grey fields indicate experimental temperatures.

As pointed out in several studies (e.g. Housh & Luhr, 1991), the An-content decreases with decreasing temperature and melt H_2O content (or $a_{\text{H}_2\text{O}}$). The An contents of plagioclase in both compositions are similar at a given temperature and melt H_2O content. The maximum An content is An ~47 for AB412 and An ~39 for AB422 at 850°C and melt H_2O contents around 4-5 wt. %.

1.4.4. Orthopyroxene

Representative orthopyroxene analyses are listed in Table 1.6.

Table 1.6: Representative compositions of experimental orthopyroxene

Sample	Experimental							
	AB412				AB422			
Run/T [°C]	40/900	41/900	35/850	31/850	11/800	37/850	38/850	30/800
cH ₂ O [wt. %] ¹	3.9	1.8	2.6	3.4	3.3	3.8	4.5	3.9
logfO ₂ [ΔNNO]	-0.62	-1.05	-0.59	-0.30	-0.44	-0.32	-0.18	-0.30
<i>wt. %</i>								
SiO ₂	51.02	51.73	50.19	52.28	50.54	49.68	50.41	50.83
TiO ₂	0.26	0.33	0.79	0.32	0.97	0.31	0.25	0.19
Al ₂ O ₃	1.09	1.78	1.69	2.66	4.57	1.43	0.99	1.28
FeO	28.01	30.51	35.07	26.82	29.64	30.02	28.24	31.95
MnO	0.98	1.05	0.90	0.88	1.24	0.89	0.97	1.53
MgO	15.03	12.05	9.85	12.93	9.59	12.82	15.76	9.74
CaO	2.27	1.89	1.56	2.14	2.03	2.67	1.32	2.93
Na ₂ O	0.09	0.24	0.18	0.28	1.08	0.13	0.01	0.14
K ₂ O	0.17	0.33	0.30	0.47	0.73	0.16	0.06	0.20
Total	98.91	99.89	100.53	98.78	100.38	98.10	98.02	98.79
<i>Structural formula (6O)</i>								
Si	1.992	2.016	1.989	2.023	1.964	1.982	1.985	2.031
Al ^{IV}	0.012	0.000	0.011	0.000	0.036	0.018	0.015	0.000
Al ^{VI}	0.038	0.081	0.068	0.121	0.173	0.049	0.031	0.060
Fe	0.915	0.995	1.162	0.868	0.963	1.002	0.930	1.068
Mg	0.875	0.700	0.582	0.746	0.555	0.762	0.925	0.580
Mn	0.032	0.035	0.030	0.029	0.041	0.030	0.032	0.052
Ti	0.008	0.010	0.024	0.009	0.028	0.009	0.007	0.006
Ca	0.095	0.079	0.066	0.089	0.085	0.114	0.056	0.126
Na	0.007	0.018	0.014	0.021	0.081	0.010	0.001	0.011
K	0.008	0.016	0.015	0.023	0.036	0.008	0.003	0.010
XMg	0.49	0.41	0.33	0.46	0.37	0.43	0.50	0.35

¹ Concentration of water in the residual glass after experiment.

For both compositions, it can be noted that the decrease of fO_2 results in a decrease of the Mg/Mg+Fe (XMg) ratio in orthopyroxene (Figure 1.4b). The trend observed in Figure 1.4 at given T is related to the change of aH₂O, which is directly linked to fO_2 (see above). Because both, the fO_2 and aH₂O, are changing simultaneously, the individual effect of these two

parameters on the XMg is difficult to determine. However, increasing T results in an increase of the XMg for given fO_2 (aH₂O).

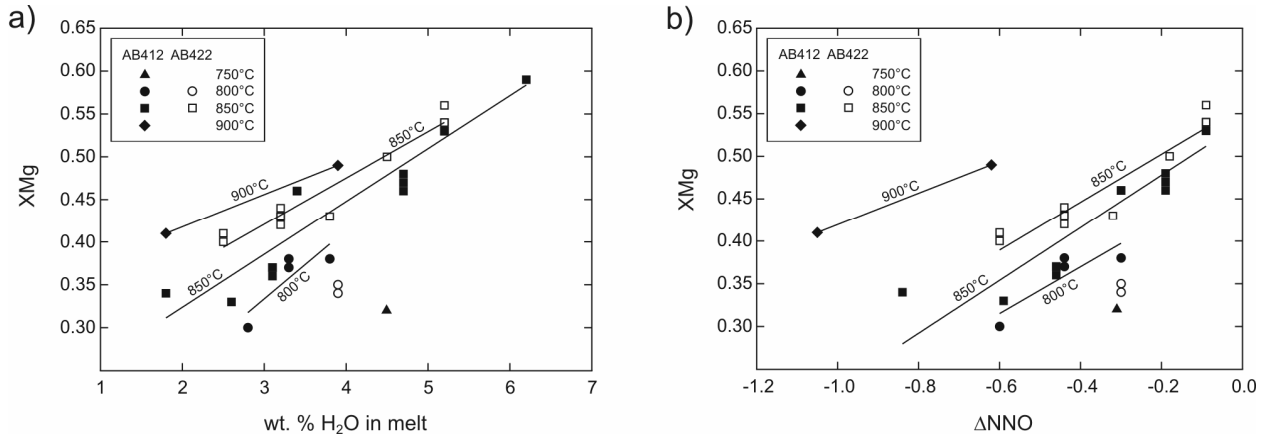


Figure 1.4: XMg of experimental orthopyroxene as a function of a) melt H₂O content and b) log fO_2 . Solid lines are linear fits for XMg at constant temperatures.

1.4.5. Hornblende and biotite

Representative analyses of synthetic hornblende are listed in Table 1.3. All are calcic amphiboles, being either ferro-edenite at 700°C or edenite at 800°C (Leake et al., 1997). The XMg increases significantly with T at constant cH₂O_{melt} and approximately constant fO_2 , with values ranging from XMg = 0.40 to 0.57. As observed for orthopyroxene, the XMg decreases also with simultaneously decreasing fO_2 and cH₂O_{melt} at constant temperature.

Biotite crystals are small for the water-undersaturated charges ($\leq 1 \mu\text{m}$) and most analyses can only be used qualitatively. Although the analyses of biotite are of lower quality, the XMg decreases from 0.55 to 0.35 at 800°C with decreasing fO_2 from NNO to NNO-0.6. Thus, the effect of T and fO_2 on the XMg is qualitatively similar in biotite and hornblende. The results also confirm that the XMg of coexisting biotite and hornblende is similar.

1.5. Discussion

1.5.1. Determination of initial water content in A-type melts of the Wangrah Suite

The least evolved magma composition found in the Wangrah Suite is close to composition AB412 (King et al., 2001). Thus, we use it as an analog for the primary magma from which the more evolved magmas, like AB422, were derived. We assume that AB412 was emplaced at near-liquidus conditions, based on high zircon saturation temperatures, and euhedral zircon crystals that appear to have been melt precipitated.

The initial water content of the primary melt can be constrained by the composition and stability of plagioclase. As shown above, the An content of plagioclase varies with melt H₂O content and temperature. In the natural rock, plagioclase cores are \leq An₃₀, which represents the composition of the first plagioclase crystallizing from the melt at high temperature. Assuming near-liquidus conditions, An₃₀ plagioclase should start to crystallise at temperatures below the zircon saturation temperature (897°C for AB412). Figure 1.2a shows that plagioclase starts to crystallise between 900 and 850°C, with water content range from 2 to 5 wt. % H₂O, respectively. Using the linear correlation between An content of plagioclase and melt H₂O content in Figure 1.3 the water content must be less than 3 wt. % H₂O to crystallise first plagioclase with An₃₀ at temperatures above 850°C. If the water content is higher than 3 wt. % H₂O (at T \geq 850°C) the crystallizing plagioclase is more calcic with An content $>$ An₃₀ which is not reproduced in the natural samples. Thus, the initial water content of the primary melt is constrained to have been from 2 to 3 wt. % H₂O.

The low water content of melts during differentiation is confirmed by the composition of melts obtained experimentally. In Figure 1 experimental melts with melt H₂O contents $<$ 4 wt. %, 4 to 6 wt. % and $>$ 6 wt. % are compared with natural bulk rock compositions. It can be noted that the CaO content of water saturated melt compositions ($>$ 6 wt.%) are systematically higher than those analysed in natural rocks (for a given SiO₂ content). In contrast melts with a melt H₂O

content <4 wt. % plot on the differentiation trend in Figure 1.1. Some water saturated melt compositions have also higher MgO content than the natural rocks (for a given SiO₂ content). Thus, experimental residual melts are close to natural compositions at water undersaturated conditions.

1.5.2. Role of orthopyroxene

The experimental results show that orthopyroxene is a liquidus phase for both compositions. However, orthopyroxene is never found in the natural samples suggesting that this mineral back-reacted during crystallisation. It can also be noted that coexisting orthopyroxene and hornblende are not found in the experiments. This does not rule out the coexistence of both minerals, but the possible field of coexisting orthopyroxene and hornblende would be small in the T- cH₂O diagram. For high melt water contents (>4 wt. %) the phase diagram for composition AB412 suggests that the orthopyroxene-out boundary coincides with the hornblende-in boundary, which may indicate that the breakdown reaction of orthopyroxene is accompanied by the formation of hornblende. However, the breakdown of orthopyroxene to form amphibole at lower temperatures has also been observed in studies on Ca-rich systems (e.g. Conrad et al. 1988). At lower water content (and for composition AB422) Fe and Mg released by the breakdown of orthopyroxene are incorporated in biotite. It is possible that the orthopyroxene in the granites back-reacted while the magma cooled, because orthopyroxene is observed in some volcanic rocks associated with A-type granites (e.g., the Comerong Volcanics which are comagmatic with the Monga A-type granite; Wyborn and Owen, 1986). In any case, orthopyroxene and the prevailing fO_2 have to be taken into account to model the differentiation path of AB412 to AB422 at temperatures between 900 and 850°C.

As shown above the composition of orthopyroxene is strongly influenced by the fO_2 . Thus, the composition of the natural orthopyroxene may differ from that obtained experimentally. To

model the differentiation path of AB412 to AB422, we have estimated the FeO and MgO contents of orthopyroxene for realistic fO_2 conditions. The fO_2 of the experiments (NNO to NNO-1.05) is more oxidizing than the minimum fO_2 estimated by King et al. (2001; NNO-2.4 to NNO-4.7).

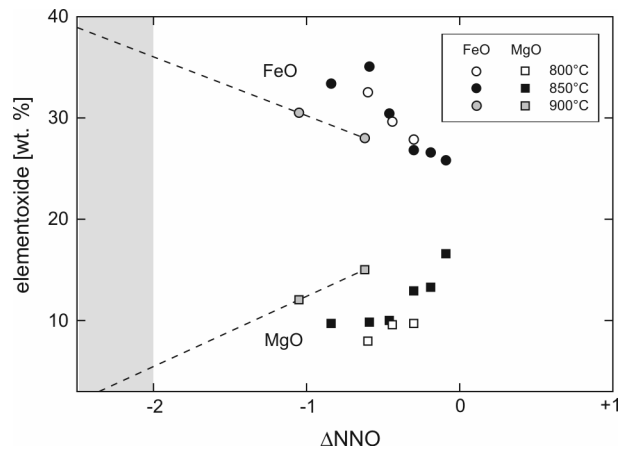


Figure 1.5: FeO (squares) and MgO (circles) contents of experimental orthopyroxene at 200 MPa as a function of $\log fO_2$. Dashed lines are linear extrapolations to constrain FeO and MgO contents at 900°C at more reducing fO_2 . Grey box: geologically relevant fO_2 .

Figure 1.5 shows that, for a given temperature, the FeO and MgO contents of orthopyroxene show trends with the highest FeO contents (~35 wt. %) at low fO_2 (aH₂O), which is in agreement with Dall’Agnol et al. (1999). An orthopyroxene composition with FeO = 38 wt. % and MgO = 4 wt. % has been used to model the differentiation of the Wangrah Suite. Such a composition is close to the most FeO rich orthopyroxenes obtained in this study (low temperature runs at 800°C). It can be noted that the orthopyroxenes obtained at high temperature (900°C) contain less FeO; however, an extrapolation of the 900°C data to lower fO_2 indicates that FeO content of 38 wt. % is realistic for orthopyroxenes crystallizing at geologically relevant conditions (high temperature and $fO_2 < \text{NNO-2.2}$).

1.5.3. Differentiation by fractional crystallisation

To model the differentiation from AB412 to AB422 we have used the phase relations in Figure 1.2 and the zircon saturation temperatures of 897°C and 843°C, respectively (these temperatures are assumed to correspond to the liquidus temperatures). The initial water content in AB412 melt is assumed to be 2 to 3 wt. % H₂O (see above). Between 900 and 850°C for 2.5 wt. % H₂O in the melt only orthopyroxene and plagioclase are stable in AB412 and AB422 (Figure 1.2). Thus, in this temperature range, only these two minerals should be involved in a differentiation process by fractional crystallisation. Mass balance calculations show that after extracting 4.7 wt. % FeO-rich orthopyroxene (FeO = 38 wt. %, see above) and 8.5 wt. % plagioclase (An₃₀) from AB412, a residual melt composition corresponding to composition AB422 is obtained (Table 1.7). The water content of the residual melt would be 2.3 to 3.5 wt. %, depending on the starting water content.

Table 1.7: Representative compositions of experimental glasses and calculated composition after subtracting 4.7 wt. % orthopyroxene and 8.5 wt. % plagioclase from AB412.

Sample	Normalized						Calculated ¹
	AB412		AB422				
Run/T [°C]	9/850	35/850	1/800	23/750	2/800	24/750	
cH ₂ O [wt. %]	3.1	2.6	6.4	5.2	6.2	5.1	
ΔNNO	-0.46	-0.59	±0	-0.19	±0	-0.20	
<i>wt. %</i>							
SiO ₂	76.29	77.71	75.02	77.67	75.23	77.95	74.03
TiO ₂	0.23	0.27	0.18	0.08	0.15	0.07	0.63
Al ₂ O ₃	12.66	12.25	13.86	12.95	13.41	12.46	13.13
FeO	1.28	1.54	1.34	0.84	1.55	0.79	2.29
MnO	0.07	0.05	0.04	0.05	0.06	0.04	0.03
MgO	0.07	0.14	0.42	0.07	0.07	0.04	0.48
CaO	0.85	0.81	1.69	0.89	1.33	0.73	1.49
Na ₂ O	3.51	2.55	3.56	2.74	3.54	2.64	3.28
K ₂ O	5.04	4.69	3.89	4.70	4.65	5.29	4.64
Total	100.00	100.00	100.00	100.00	100.00	100.00	100.00

¹ for the compositions of orthopyroxene and plagioclase, see text.

It can be noted that the residual melt compositions obtained in run 35 and run 9 (AB412, T= 850°C, 2.6 and 3.1 wt. % H₂O; Table 7) are not similar to the composition AB422. In addition the amount of crystals observed experimentally is higher than the amount calculated in the fractional crystallisation model above ($\geq 25\%$). This can be explained by the difference in fO_2 between natural and experimental conditions. Less orthopyroxene needs to fractionate to obtain composition AB422, if this mineral contains more FeO as would be expected at NNO-2.4 to NNO-4.7. In addition it has been shown that the upper stability of plagioclase is shifted to lower temperatures with decreasing fO_2 (Dall'Agnol et al., 1999).

1.5.4. Stability of hornblende

In our H₂O-saturated experiments, both the composition and thermal stability of hornblende depend on fO_2 . The experimental hornblende compositions are close to the natural hornblende compositions except for the Fe/Mg ratio (Table 1.3). The natural hornblendes are invariably ferro-edenites (Leake et al., 1997) because of the lower fO_2 during crystallisation of the granite compared to the more oxidizing fO_2 in the experiments.

In Figure 1.6, the stability field of experimental hornblende obtained in this study at $fO_2 \sim$ NNO is compared to the study of Dall'Agnol et al. (1999) at more oxidizing ($fO_2 \sim$ NNO+2.5) and more reducing ($fO_2 \sim$ NNO-1.5) conditions. At NNO+2.5 hornblende crystallises above 850°C and the hornblende stability field does not extend to the solidus. At NNO and NNO-1.5 the stability field of hornblende is restricted to lower temperatures (between 800 to 850°C). Thus, with decreasing fO_2 the hornblende stability field is shifted towards lower temperature. The stability field of hornblende extends to the solidus only at the most reduced fO_2 (NNO-1.5).

It is known that the stability of hornblende depends strongly on the water content of the melt (e.g. Naney, 1983). The crystallisation of hornblende in A-type granites requires a relatively high water content of the melt of at least 4 to 5 wt. % H₂O, in agreement with Dall'Agnol et al.

(1999). This contrasts with the other mafic hydrous mineral, e.g. biotite, which is found to be stable for water contents as low as 2 - 2.5 wt. % (Dall'Agnol et al., 1999; Figure 1.2). Thus, it is emphasized that the two hydrous Fe-Mg bearing minerals (biotite and hornblende) have markedly different phase boundaries in the T- cH₂O diagrams in agreement to previous studies (e.g. Conrad et al., 1988; Dall'Agnol et al., 1999). Hornblende is not necessarily crystallizing in early magmatic stages and biotite may occur prior to hornblende in the crystallisation sequence of magmatic rocks, depending on the melt H₂O content.

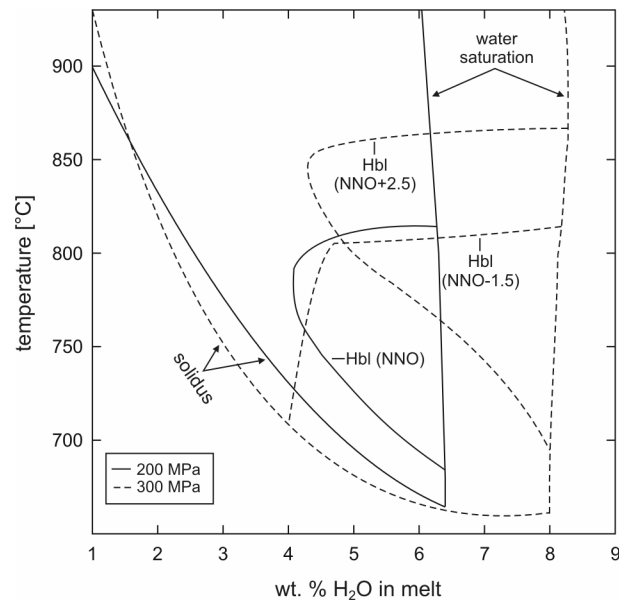


Figure 1.6: Comparison of hornblende stability fields as a function of T and melt H₂O content for the composition AB412 at 200 MPa and $fO_2 = \text{NNO}$ (solid line) with experimental results of Dall'Agnol et al. (1999) at 300 MPa and $fO_2 = \text{NNO-1.5}$ and NNO+2.5 (dashed lines).

Hornblende can not be an early phase in the crystallisation sequence of the Wangrah Suite because of the relatively low initial melt H₂O content of 2 to 3 wt. %. Assuming such an initial water content, the required melt H₂O content to form hornblende (~4.5 wt. %) is only attained after crystallisation of 35 to 55 wt. % of anhydrous minerals from the magma.

Finally, our results allow us to constrain the influence of bulk composition on the stability of hornblende. Hornblende crystallises only in the less differentiated composition AB412 with a CaO content of 2.0 wt. %. The starting material in the study of Dall'Agnol et al. (1999; CaO =

2.2 wt. %) is close to composition AB412. They observe hornblende at reduced and oxidized conditions. Clemens et al. (1986) conducted experiments at 100 MPa with a starting composition (CaO = 1.3 wt. %) close to composition AB422. They did not observe hornblende in the experiments but this is most likely due to the low pressure (below 100 MPa the maximum H₂O content of the melt is <4.5 wt. %). However, in our experiments at 200 MPa with the more felsic composition AB422 (CaO = 1.3 wt. %) hornblende is also never observed. The synthesis with the previous experimental results may indicate that the crystallisation of hornblende in A-type granites is probably limited to the less felsic granitic compositions with CaO contents of the melt of >1.3 wt. %. It must be noted that hornblende has not been observed in experiments with composition AB422 but it is present in small quantities in the natural assemblage (~0 - 3 modal %).

1.6. Conclusions

In this study the investigation of phase relationships of two compositions representing different degrees of differentiation, the combination of geochemical data and phase stability fields and the comparison of natural and experimental phase compositions were used to determine the water content of the primary melt and the mechanism of differentiation in the Wangrah Suite. The water content of the less differentiated melt was constrained between 2 to 3 wt. % H₂O. Thus, the Wangrah Suite A-type granites are H₂O undersaturated but not exceptionally H₂O-poor, in agreement with previous workers (King et al., 1997; King et al., 2001). Compared to other A-type granites, the water content of the less differentiated melts are similar (Clemens et al., 1986; 2.4 to 4.3 wt. %) or lower (Dall'Agnolet al., 1999; 4.5 to 6.5 wt. %).

Although orthopyroxene is not observed in the natural rocks, this mineral influenced the early differentiation of A-type granites of the Wangrah Suite. The back reaction of orthopyroxene can

be related to the appearance of hornblende if the water and CaO content of the residual melt is high enough. The stability of hornblende is also dependent on fO_2 . Decreasing fO_2 decreases the upper thermal stability of hornblende and extends the lower stability of hornblende to the solidus.

The differentiation of the high temperature magmas of the Wangrah Suite is controlled by fractionation of orthopyroxene and plagioclase. Assuming geologically relevant fO_2 conditions a mass balance calculation show that the more felsic composition AB422 can be obtained after the crystallisation of 4.7 wt. % iron-rich orthopyroxene plus 8.5 wt. % plagioclase (An30) from the less evolved composition AB412. Using zircon saturation temperatures, this crystallisation is caused by a temperature decrease of approximately 50°C (897 to 843°C).

This fractionating assemblage composed of mainly orthopyroxene and plagioclase is compositionally close to anorthosite, mangerite or ferrodiorite, rocks which are commonly associated with A-type granites, especially in Precambrian shields (e.g., Haapala & Rämö, 1992; Frost et al., 1999). This is an alternative explanation to that proposed by Patiño Douce (1997) who pointed out that plagioclase and orthopyroxene assemblages associated to A-type granites may represent the solid residual assemblage resulting from low pressure melting of calc-alkaline granitoids (e.g. tonalite).

2. Differentiation processes in A-type granites: Crystal fractionation vs. magma mixing

2.1. Introduction

The term A-type granite, as proposed by Loiselle & Wones (1979) to distinguish high $K_2O + Na_2O$, anhydrous and anorogenic granitic rocks from calc-alkaline I-type granites, has been subject of much controversial debate on the origin of these rocks. Less evolved metaluminous to weakly peraluminous A-type granites are characterized by high SiO_2 , Ga/Al , Fe/Mg , Zr , Nb , Y and REE (except Eu) and low CaO (Loiselle & Wones, 1979; Collins et al., 1982; Whalen et al., 1987; Eby, 1990; King et al., 1997) but more felsic, fractionated A-type granites have similar compositional characteristics similar to fractionated I-type granites (King et al., 1997, 2001). A-type granite magma can be generated by partial melting of crustal igneous rocks of tonalitic to granodioritic compositions (e.g., Skjerlie & Johnston, 1992, 1993; Cullers et al., 1993; Patiño Douce, 1997; Dall'Agnol et al., 1999) or of a part of the lithosphere from which a previous melt had been extracted (e.g., Collins et al., 1982; Whalen et al., 1987) but direct derivation by extreme fractionation from basaltic magma is discussed as well (Turner et al., 1992; Frost & Frost, 1997; Vander Auwera et al., 2003). However, A-type magmatism is accompanied by high heat flux caused by deeper mafic magmatism (e.g. Emslie & Stirling, 1993; Frost & Frost, 1997; Turner & Foden, 1996; Haapala & Rämö, 1992). The primary magmas are not strictly anhydrous and can have water contents of several weight percents, similar to other types of granitic magma (Clemens et al., 1989; King et al., 2001; Dall'Agnol et al., 1999; Bogaerts et al., 2003) but the change of melt H_2O contents is poorly known.

Crystal fractionation is one of the major differentiation processes in A-type granitic systems (Collins et al., 1982; Clemens et al., 1986; Chappell et al., 1987; Whalen et al., 1987; Creaser et al., 1991; King et al., 1997; King et al., 2001). Previous fractionation models in A-type granitic

systems (e.g., Lumbers et al., 1991; Martin et al., 1994; Rajesh, 2000; Asrat & Barbey, 2003) are based on geochemical observations in the natural rocks without respect to mineral compositions and abundances in the parent magma at modelled physical conditions. This is due to the sparse experimental data in natural A-type granitic systems (Clemens et al., 1986; Dall'Agnol et al., 1999) giving insufficient information about crystal-melt equilibrium at varied temperatures, pressures, volatile contents (e.g. H₂O, F), oxygen fugacities (fO_2) or bulk compositions.

Another controversial debate has focussed on the interpretation of the rapakivi texture which is a common feature in A-type granites, especially in Proterozoic A-type granites (rapakivi-texture is defined here as the occurrence of plagioclase-mantled K-feldspar ovoids and two generations of quartz in a more fine-grained matrix). The formation of rapakivi texture is attributed to bimodal magma-mixing processes (Hibbard, 1981; Wark & Stimac, 1992), subsolvus re-equilibration reactions (Dempster et al., 1993) or decompression of partly crystallised water undersaturated magmas (Nekvasil, 1991; Eklund & Shebanov, 1999). However, all models have in common that particular processes must occur during and after crystallisation (Haapala & Rämö, 1999). Thus, understanding the formation of rapakivi-texture is an important key to model crystallisation processes in many A-type granites.

Generally crystal-melt equilibrium experiments are performed with the goal of constraining parameters such as primary water content in the melt, temperature, pressure and fO_2 (e.g., Clemens et al., 1986; Dall'Agnol et al., 1999). Clemens et al. (1986) and Dall'Agnol et al. (1999) performed experiments using one bulk composition, assumed to be representative of a studied pluton. Thus, these studies provide only information on only one part of the crystallisation history because fractionation processes may lead to the formation of different bulk granitic composition within one suite.

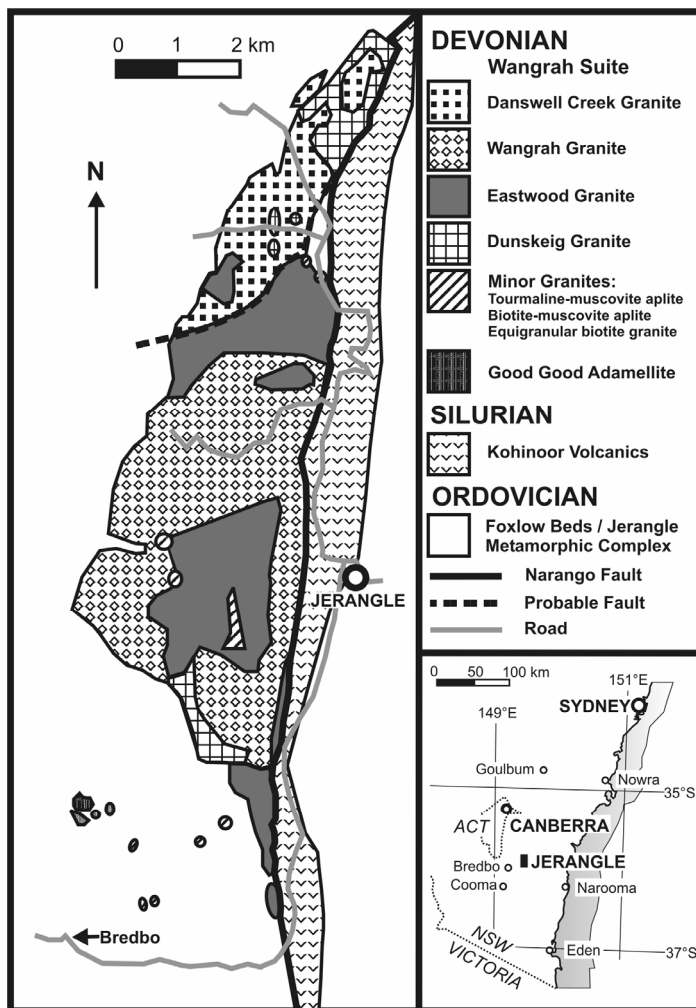
This study discusses the experimentally determined T versus melt H₂O phase diagrams of four granite compositions from the A-type granite Wangrah Suite, Lachlan Fold Belt, SE

Australia. The four compositions (Danswell Creek, Wangrah, Eastwood and Dunskeig Granite) were interpreted to result from crystal fractionation processes, based on major and trace element distributions (King et al., 2001). However, King et al. (2001) noted that Rb showed trends that were difficult to explain via this process. The experimental data are used to test this hypothesis and to constrain the nature, amount and composition of fractionating minerals as well as the differentiation processes from the parental water undersaturated granitic magma (Danswell Creek) to the most felsic magma (Dunskeig) at shallow level conditions. Changing water activities ($a_{\text{H}_2\text{O}}$) during crystal fractionation can be modelled and are taken into account to discuss the evolution of physical properties of magmas (viscosity) assuming isobaric crystallisation. The results indicate that the four experimentally investigated bulk compositions can not represent a simple crystal fractionation trend. At least one composition, representing the main granite within the Wangrah Suite (Wangrah Granite, with relative high K_2O content), may be the result of interaction between highly evolved partly crystallised magmas with primary undifferentiated granitic magmas, leading to the formation of rapakivi-textures.

2.2. Granites of the Wangrah Suite and starting material

The Wangrah Suite occurs over an area of 23 km² in the Lachlan Fold Belt, near Jerangle, in SE-Australia (Figure 2.1). It outcrops with a pod-like shape along the Narongo fault and consists of four major granite intrusions; Danswell Creek Granite, Wangrah Granite, Eastwood Granite and Dunskeig Granite (ordered by increasing silica content). The geology, petrology and geochemistry of the Wangrah Suite have been described in detail by King (1992) and King et al. (2001). The granites emplaced at shallow level (100-200 MPa) at reducing f_{O_2} of NNO – 2.4 to NNO – 4.7 (King et al., 2001). In the following section, a brief summary of petrographic and petrological features important for the understanding of the crystallisation of the Wangrah Suite are given.

The Danswell Creek Granite is a white, equigranular medium grained monzogranite containing hornblende, biotite, ilmenite, zircon, apatite and minor titanite. Anorthite contents of plagioclase vary from An_{30} to An_{10} . Among the Wangrah Suite granites the Danswell Creek Granite has the highest modal abundance of mafic minerals (biotite, ilmenite and hornblende; 8 to 10.5 %) and the lowest abundance of K-feldspar (21 to 35 %).



The Wangrah Granite is the most abundant rock of the Wangrah Suite. It is a pink-grey to white monzogranite containing hornblende, biotite, ilmenite, zircon and apatite. The rock is distinguished by a variably porphyritic texture with K-feldspar and quartz phenocrysts set in a groundmass of K-feldspar, quartz, plagioclase and biotite \pm hornblende. K-feldspar often shows

ovoid crystal form and is often rimmed (partly and completely) by plagioclase displaying local rapakivi texture. Two generations of quartz can be identified within the rock, which is typical for many rapakivi granites (e.g., Eklund & Shebanov, 1999). Anorthite contents of plagioclase vary from An₃₀ to An₁₀. Modal abundance of the minerals depend on the distribution of phenocrysts. K-feldspar is enriched up to 47 % in samples displaying rapakivi-texture coupled with the lowest plagioclase contents of 18 %. In samples with a few (or none) K-feldspar phenocrysts plagioclase is the most abundant phase (up to 49 %) and the amount of K-feldspar in the matrix is 13 %. Quartz and mafic mineral abundance is relatively constant with 23-30 % quartz and 5-12 % mafic minerals.

The Eastwood Granite is a fine-grained red annite monzogranite containing biotite, ilmenite, zircon and apatite with sparse K-feldspar and quartz phenocrysts. K-feldspar is the most abundant phase (up to 40 %) while plagioclase and quartz occur in approximately equal proportions (25-30 %). Mafic minerals are subordinate with 3-7 %. Anorthite content of plagioclase vary from An₂₅ to An₅.

The most evolved rock of the Wangrah Suite is the brick red equigranular Dunskeig Granite. This rock is characterized by the highest amount of K-feldspar (40-50 %) and the lowest distribution of mafic minerals <3 %. Biotite is conspicuous and occurs either as large single euhedral (8 mm) or interstitial crystals. Anorthite content of plagioclase is An₁₃ to An₅. The Dunskeig Granite could represent a carapace of a deeper pluton because it outcrops topographically higher than the other granites (King et al., 2001).

Five representative chemical analyses of the Wangrah Suite are listed in Table 2.1. Except sample AB408, these compositions were used as starting material for crystallisation experiments. The samples AB412, AB422, AB421 and AB401 come from the Danswell Creek, Wangrah, Eastwood and Dunskeig granites, respectively. As emphasized above, the chemical variations, such as decreasing FeO, MgO, CaO, Sr and Ba with increasing SiO₂ are likely to be the result of

crystal fractionation processes (King et al., 2001). The primary melt composition is assumed to be close to the most mafic compositions of the Danswell Creek Granite (e.g. AB412, King et al., 2001). In a previous experimental study, the initial water content in the primary melt was constrained to be 2-3 wt. % based on plagioclase stability and composition (see §1.5.1). In §1.5.3. it was also emphasised that orthopyroxene, besides plagioclase, was part of the first fractionating mineral assemblage, although this mineral was not found in the natural rock.

Table 2.1: Compositions of natural rocks and synthesised glasses

	Wangrah Granites ¹					Enclaves ¹		Starting glass compositions								
	AB412	AB422	AB408	AB421	AB401	GVP	MGE	AB412 ²		AB422 ²		AB421		AB401		
								n=10	σ	n=11	σ	n=10	σ	n=14	σ	
<i>wt. %</i>																
SiO ₂	70.45	72.53	73.71	75.32	76.67	71.27	66.39	71.89	0.40	73.85	0.44	75.65	0.39	77.56	0.44	
TiO ₂	0.54	0.37	0.29	0.15	0.09	0.41	1.00	0.55	0.04	0.38	0.05	0.17	0.04	0.10	0.02	
Al ₂ O ₃	13.26	13.08	12.68	12.71	12.10	13.37	13.97	13.60	0.11	13.42	0.17	13.04	0.19	12.39	0.33	
FeO	4.06	2.50	2.11	1.62	0.92	2.64	4.73	4.14	0.15	2.58	0.13	1.71	0.09	1.13	0.11	
MnO	0.08	0.05	0.04	0.06	0.02	0.05	0.06	0.07	0.06	0.05	0.04	0.06	0.05	0.06	0.06	
MgO	0.61	0.48	0.31	0.23	0.05	0.52	1.37	0.62	0.02	0.46	0.01	0.19	0.02	0.04	0.02	
CaO	1.93	1.31	1.10	0.90	0.53	1.48	3.00	1.96	0.02	1.32	0.06	0.96	0.05	0.51	0.04	
Na ₂ O	3.39	3.32	3.06	3.36	3.25	3.27	3.47	3.38	0.10	3.34	0.14	3.40	0.16	3.45	0.17	
K ₂ O	3.98	4.88	4.98	4.61	5.12	5.01	4.02	3.79	0.11	4.62	0.10	4.80	0.15	4.76	0.16	
P ₂ O ₅	0.18	0.12	0.08	0.05	0.01	0.13	0.22	-	-	-	-	-	-	-	-	
rest	0.23	0.17	-	0.12	0.09	0.17	0.19	-	-	-	-	-	-	-	-	
Total	98.71	98.81	98.36	99.13	98.85	98.32	98.42	100.00		100.00		100.00		100.00		
Qz	34.5	33.9	37.0	38.3	38.6	32.2	27.4									
Ab	36.0	32.6	29.5	31.5	29.3	32.7	40.2									
Or	29.5	33.5	33.5	30.2	32.2	35.0	32.5									
Ab/An	3	4	5	6	10	4	3									
<i>ppm</i>																
F	n.d.	1040	n.d.	670	n.d.	n.d.	n.d.									
Rb	146	228	216	216	187	233	177									
Sr	128	87	76	56	14	101	168									
Ba	505	215	220	148	61	260	205									
Zr	535	313	270	190	116	301	340									
Nb	26	21	17	20	11	21	20									
Ga	22.2	21.2	20.4	19.6	22.4	22	23									
Y	75	64	56	77	125	64	59									
La	64	53	66	28	24	63	51									
Ce	145	121	133	63	64	127	121									
Zn	81	52	44	52	28	52	82									
Zr-sat. T [°C] ³	897	843	834	806	764	839	-									

¹Source of data: King (1992); King et al. (2001): AB412 sample of Danswell Creek Granite; AB422 and AB408 samples of Wangrah Granite; AB421 sample of Eastwood Granite; AB401 sample of Dunskeig Granite.

²after §1

³Calculated zircon saturation temperatures after Watson & Harrison (1983).

Enclaves are present within all observed granite types and range from mafic to felsic compositions with distinct phenocrysts. The most important features of two types of enclaves as identified by King (1992) are summarised in the following.

Microgranular enclaves (MGE) are the most common enclaves found in all granite types except the Dunskeig Granite. They are more mafic in bulk composition compared to AB412 (Table 2.1) and appear as a dark rock with grain size <1 mm. They may also contain scarce phenocrysts of K-feldspar, plagioclase and quartz. In some cases K-feldspar in the enclaves crosses the margin between the granite and the enclave. Matrix plagioclase is more calcic than in the other phases with An_{20-35} . Ferro-edenite is present throughout the enclaves and often has cores of augite.

The grey, variable porphyritic phase (GVP) consists of phenocrysts (K-feldspar, quartz and plagioclase) set in a fine groundmass containing feldspars, quartz, hornblende and biotite. K-feldspar phenocrysts are often mantled by plagioclase as found in the Wangrah Granite. The matrix plagioclase is normally zoned from An_{30} to An_{10} . The modal proportions of minerals depend on the distribution of phenocrysts varying dramatically on a meter scale but in the range of the Wangrah Granite. The GVP is observed as rounded boulders in the Wangrah and Dunskeig granites. Bulk composition of the GVP is close to AB422 for K_2O and to AB412 for SiO_2 , FeO and CaO (Table 2.1).

Besides the enclaves sparse tholeiitic basalt dykes can be found in all granites except the Eastwood granites. The margins of the dykes show evidence for intrusion while the surrounding granite was partially crystalline.

2.3. Methods and experimental techniques

The natural rock powders (AB412, AB422, AB421 and AB401) were melted twice in a Pt crucible at 1600°C and 1 atm, with grinding in an agate mortar between the two melting steps.

The glass compositions were determined by electron microprobe analysis and are similar to the natural rock composition (Table 2.1). The anhydrous glasses were ground and then 90 wt. % glass and 10 ± 0.2 wt. % fluid were loaded in welded gold capsules. The amount of added fluid was low to avoid undesirable effects of incongruent dissolution of silicate in the fluid. The water activity ($a_{\text{H}_2\text{O}}$) of the experimental charges was varied by adding a fluid composed of a mixture of H_2O and CO_2 . CO_2 was added as silver oxalate ($\text{Ag}_2\text{C}_2\text{O}_4$). The mole fraction of water in the added fluid phase was varied in a range of $X_{\text{H}_2\text{O}_{\text{initial}}} = 0.4$ to 1.0. It is emphasized that this $X_{\text{H}_2\text{O}_{\text{initial}}}$ is different from the final $X_{\text{H}_2\text{O}}$ because H_2O is preferentially dissolved in silicate melts.

Crystallisation experiments with AB412 and AB422 have been performed and described in §1 at 200 MPa and the products will not be described in detail here. However, most of the experimental results are given in Table 2.2. For these experiments, the phase proportions have been calculated within the frame of this study using the phase compositions given in §1.

Crystallisation experiments with AB421 and AB401, covering the temperature interval 700 to 850°C, were performed at 200 MPa in cold seal pressure vessels (CSPV) with water as the pressure medium. Run duration varied with temperature: 16 to 32 days for runs at 700 to 750 °C, 8 days at 800 and 850°C. The oxygen fugacity (f_{O_2}) was monitored by adding a solid Ni-NiO buffer in the vessel for experiments conducted with CSPV. These vessels are made of Ni-alloy, which allows to perform long run duration with the solid buffer technique at $f_{\text{O}_2} = \text{NNO}$. Because water activity and water fugacity ($f_{\text{H}_2\text{O}}$) varies in the experiments (as a function of the mole fraction of water in the charge), f_{O_2} is not strictly constant at given P and T. In our experiments f_{O_2} ranges from NNO to NNO-1.05 log units (Table 2.2).

After the runs, a H-O or a H-O-C fluid phase was detected qualitatively in all charges by weight loss and freezing in a cold trap cooled by liquid nitrogen (for CO_2) and weight loss after heating up to 105°C (for H_2O). However, because of the too low amount of added fluid, the final

Table 2.2: Experimental results and calculated proportion of phases (wt. %) at 200 MPa and $\log f_{O_2} \sim NNO$

Run	T [°C]	Duration [days]	$X_{H_2O}^1$	ΔNNO^2	$c_{H_2O}^3$ [wt. %]	Results (+Fl) ⁴								Σf^{25}	
						gl	pl	kfs	qz	ox	bt	hbl	opx		fay
<i>AB412^b</i>															
15	700	32	1.00	±0	6.5	75.94	13.39	-	-	2.59	7.51	0.56	-	-	0.18
13	750	32	1.00	±0	6.2	90.46	4.82	-	-	3.51	0.42	0.78	-	-	0.03
23	750	32	0.80	-0.19	5.2	65.49	17.94	-	6.38	1.97	5.11	3.11	-	-	0.15
1	800	8	1.00	±0	6.4	94.17	-	-	-	2.98	1.37	1.48	-	-	0.12
25	800	8	0.90	-0.09	5.2	87.27	6.49	-	-	3.07	1.59	1.57	-	-	0.10
7	800	8	0.80	-0.19	4.6	83.79	10.02	-	-	2.66	0.50	3.02	-	-	0.16
29	800	8	0.71	-0.30	3.8	70.87	19.49	-	2.13	2.20	1.32	-	3.98	-	0.13
33	800	8	0.50	-0.60	2.8	53.14	26.58	1.88	8.27	1.00	3.79	-	5.34	-	0.29
3	850	8	1.00	±0	6.2	96.69	-	-	-	2.15	-	-	1.16	-	0.12
27	850	8	0.90	-0.09	5.2	95.94	-	-	-	2.62	-	-	1.44	-	0.24
5	850	8	0.80	-0.19	4.7	95.53	-	-	-	1.66	-	-	2.71	-	0.24
31	850	8	0.71	-0.30	3.4	81.27	13.12	-	-	2.23	-	-	3.37	-	0.34
9	850	8	0.59	-0.46	3.1	77.35	14.63	-	-	1.03	-	-	6.99	-	0.28
35	850	8	0.51	-0.59	2.6	72.93	19.36	-	-	0.98	-	-	6.72	-	0.12
19	850	8	0.38	-0.84	1.8	65.60	23.73	0.97	-	1.57	-	-	8.12	-	0.98
39	900	6	1.00	-0.30	6.0	98.70	-	-	-	1.30	-	-	-	-	0.18
40	900	6	0.69	-0.62	3.9	97.18	-	-	-	1.33	-	-	1.48	-	0.13
41	900	6	0.42	-1.05	1.8	81.46	12.86	-	-	1.50	-	-	4.18	-	0.07
<i>AB422^b</i>															
16	700	32	1.00	±0	6.4	92.13	-	-	-	0.45	7.41	-	-	-	0.37
14	750	32	1.00	±0	6.4	94.81	-	-	-	1.62	3.57	-	-	-	0.07
24	750	32	0.79	-0.20	5.1	43.38	23.80	7.67	15.67	0.01	9.47	-	-	-	0.05
2	800	8	1.00	±0	6.2	95.99	-	-	-	0.71	3.30	-	-	-	0.05
26	800	8	0.90	-0.09	5.2	95.22	-	-	-	1.63	3.14	-	-	-	0.31
8	800	8	0.79	-0.20	4.5	91.01	4.92	-	-	1.19	2.88	-	-	-	0.08
30	800	8	0.71	-0.30	3.9	79.57	13.64	-	-	1.49	3.62	-	1.68	-	0.15
12	800	8	0.59	-0.46	3.3	71.66	16.46	1.96	3.60	0.56	0.66	-	5.10	-	0.13
34	800	8	0.50	-0.60	2.5	40.35	20.16	19.11	15.79	0.10	3.69	-	0.80	-	0.21

Table 2.2: Continued

Run	T [°C]	Duration [days]	XH ₂ O _n ¹	ΔNNO ²	cH ₂ O ³ [wt. %]	Results (+Fl) ⁴									ΣF ⁵
						gl	pl	kfs	qz	ox	bt	hbl	opx	fay	
4	850	8	1.00	±0	6.2	98.09	-	-	-	0.77	1.14	-	-	-	0.14
28	850	8	0.90	-0.09	5.2	97.02	-	-	-	0.78	0.90	-	1.30	-	0.12
38	850	8	0.81	-0.18	4.5	96.77	-	-	-	1.20	1.36	-	0.68	-	0.18
37	850	8	0.69	-0.32	3.8	93.21	3.71	-	-	1.25	0.12	-	1.71	-	0.10
10	850	8	0.60	-0.44	3.2	90.94	6.29	-	-	0.46	-	-	2.31	-	0.54
36	850	8	0.50	-0.60	2.5	86.18	10.18	-	-	0.48	-	-	3.16	-	0.12
20	850	6	0.40	-0.80	1.8	47.30	17.99	17.84	12.98	1.10	-	-	2.78	-	0.16
AB421															
61	700	32	1.0	±0	6.3	95.10	-	-	-	0.05	4.85	-	-	-	0.41
60	700	32	0.80	-0.19	5.2	15.08	23.34	30.90	27.78	1.28	1.63	-	-	-	0.01
76	725	32	0.89	-0.10	5.8	96.93	-	-	-	0.57	2.51	-	-	-	0.26
77	725	32	0.80	-0.19	5.4	85.37	8.15	-	4.21	0.70	1.57	-	-	-	0.09
65	750	16	0.90	-0.09	5.8	94.41	-	-	-	0.32	5.27	-	-	-	0.48
64	750	16	0.71	-0.30	4.9	45.73	12.23	21.78	18.25	0.95	1.06	-	-	-	0.16
80	760	32	0.80	-0.19	5.1	92.84	4.80	-	-	0.82	1.55	-	-	-	0.10
84	775	32	0.69	-0.32	4.2	91.31	5.90	-	-	0.72	1.97	-	0.10	-	0.02
85	775	32	0.57	-0.49	3.9	90.00	7.80	-	-	0.63	1.36	-	0.22	-	0.05
75	800	8	0.89	-0.10	5.1	99.75	-	-	-	0.25	-	-	-	-	0.27
74	800	8	0.79	-0.20	4.5	99.30	-	-	-	0.20	-	-	0.50	-	0.34
73	800	8	0.71	-0.30	3.9	98.10	-	-	-	0.22	-	-	1.68	-	0.81
72	800	8	0.60	-0.32	3.2	93.91	4.38	-	0.12	0.21	-	-	1.38	-	0.04
52	800	8	0.51	-0.59	2.7	87.67	8.76	-	1.92	0.30	-	-	1.35	-	0.07
59	850	8	0.71	-0.30	3.8	99.80	-	-	-	0.20	-	-	-	-	0.25
58	850	8	0.59	-0.46	3.0	98.97	-	-	-	1.03	-	-	-	-	0.87
57	850	8	0.49	-0.62	2.5	93.82	4.78	-	-	0.21	-	-	1.19	-	0.27
56	850	8	0.42	-0.75	2.1	90.18	5.40	-	2.14	0.48	-	-	1.80	-	0.10
AB401															
62	700	32	1.0	±0	6.3	98.17	-	-	-	0.32	1.50	-	-	-	0.09
63	700	32	0.81	-0.18	5.1	35.23	10.23	30.01	22.97	0.66	0.89	-	-	-	0.00

Table 2.2: Continued

Run	T [°C]	Duration [days]	XH ₂ O _{in} ¹	ΔNNO ²	cH ₂ O ³ [wt. %]	Results (+Fl) ⁴									Σr ²⁵
						gl	pl	kfs	qz	ox	bt	hbl	opx	fay	
78	725	32	0.90	-0.09	6.0	99.19	-	-	-	0.68	0.13	-	-	-	0.20
79	725	32	0.80	-0.19	5.5	63.58	7.79	14.49	13.47	0.63	0.04	-	0.00	-	0.02
66	750	16	0.91	-0.08	5.1	45.89	7.45	26.85	18.66	0.75	0.40	-	-	-	0.01
67	750	16	0.71	-0.30	4.0	43.68	11.48	23.61	19.98	0.66	0.59	-	-	-	0.03
81	760	32	0.90	-0.09	5.0	99.66	-	-	-	0.34	-	-	-	-	0.12
82	760	32	0.78	-0.22	4.6	99.61	-	-	-	0.39	-	-	-	-	0.10
83	760	32	0.68	-0.33	4.2	75.27	8.15	5.86	9.75	0.33	0.63	-	-	-	0.01
86	775	32	0.69	-0.32	4.2	100.00	-	-	-	-	-	-	-	-	-
87 ⁷	775	32	0.58	-0.47	3.4	77.65	12.28	1.22	8.94	0.44	-	-	0.16	-	0.01
87 ⁷	775	32	0.58	-0.47	3.4	76.98	12.28	0.76	8.75	0.42	-	-	-	0.14	0.01
71	800	8	0.88	-0.11	4.9	100.00	-	-	-	-	-	-	-	-	-
70	800	8	0.75	-0.25	4.1	100.00	-	-	-	-	-	-	-	-	-
69	800	8	0.61	-0.43	3.2	99.77	-	-	-	0.23	-	-	-	-	0.08
68	800	8	0.51	-0.59	2.7	89.20	5.97	-	4.30	0.52	-	-	-	-	0.02

¹XH₂O_{in} = H₂O/(H₂O + CO₂) loaded in the capsule (in moles).

²ΔNNO = log fO₂ (experiment) – log fO₂ (NNO; Chou, 1987). For water saturated experiments at temperatures between 700 and 850°C in the CSPV the fO₂ = NNO. For H₂O-undersaturated charges, a maximum possible fO₂ is calculated as log fO₂ = log fO_{2(aH₂O=1)} + 2log XH₂O_{in}. Details for 900°C runs see §1.

³Water contents of glasses determined using the difference method (Devine et al., 1995).

⁴Phases present in run products. When present, amount of crystals was calculated by mass balance calculation with least squares minimisation (Le Maitre, 1976). Runs with 100 wt. % glass were above the liquidus. Mineral abbreviations as given by Kretz (1983): Fl: fluid; gl: glass; pl: plagioclase; kfs: K-feldspar; qz: quartz; ox: Fe-Ti-oxide; bt: biotite; hbl: hornblende; opx: orthopyroxene; fay: fayalite. Fluid was present in all runs.

⁵Sum of residual squares obtained by the mass balance calculations.

⁶Experimental results in §1.

⁷Calculated with opx or fay because mineral textures indicate breakdown reaction of opx producing fay.

XH₂O of the fluids after the experiments could not be analysed quantitatively by this method.

The phases were identified and their compositions were determined by electron microprobe (Cameca SX 100 at the University of Hanover). Crystalline phases were analysed with 15 kV acceleration voltage, 10 nA sample current and 10 s total counting time. To minimise the migration of alkali during glass analysis the analytical conditions were 15 kV, 6 nA and 5 s total counting time and the beam was defocused up to 20 μm when possible (lowest value was 5 μm , Na was measured first). The H₂O contents of the glasses were estimated with microprobe analyses following the difference method described by Devine et al. (1995). Six hydrous rhyolitic glasses (with 0.2 to 7.15 wt. % H₂O) whose H₂O contents were determined by Karl Fischer titration with an uncertainty of ± 0.15 wt. % H₂O (Holtz et al., 1995) were used as standard glasses. The standard and experimental glasses were measured during the same analytical session. The precision of the method can be tested for water saturated experiments. The results obtained by the difference method are identical within ± 0.2 wt. % H₂O to water solubilities at 200 MPa determined in subaluminous rhyolitic glasses (§1). In charges with lower melt fraction this error might be higher but is expected to be within ± 0.5 wt. % H₂O.

2.4. Experimental results

2.4.1. Phase relations

The results of the crystallisation experiments for AB421 and AB401 are represented in phase diagrams (Figure 2.2). The experimentally determined phase diagrams of AB412 and AB422 are not presented here (see Figure 1.2) but the results for nearly all compositions are listed in Table 2.2. The phase diagrams are isobaric T- cH₂O_{melt} sections where cH₂O_{melt} is the H₂O content of the glasses (wt. %) determined by the deficit in the microprobe total. The solidus curve represents the locus of the Qz-Ab-Or-H₂O solidus for a given aH₂O after Holtz et al. (2001) lowered by $\sim 25^\circ\text{C}$ to account for the weakly peraluminous character of the starting material

(Johannes & Holtz, 1996). The water-saturation curve has been drawn on the basis of the experimental results in the subaluminous granitic system (Holtz et al., 2001) with a maximum water solubility of 6.2 wt. % at 800 °C, 200 MPa and a temperature dependence of -16×10^{-4} wt. % $\text{H}_2\text{O} / ^\circ\text{C}$.

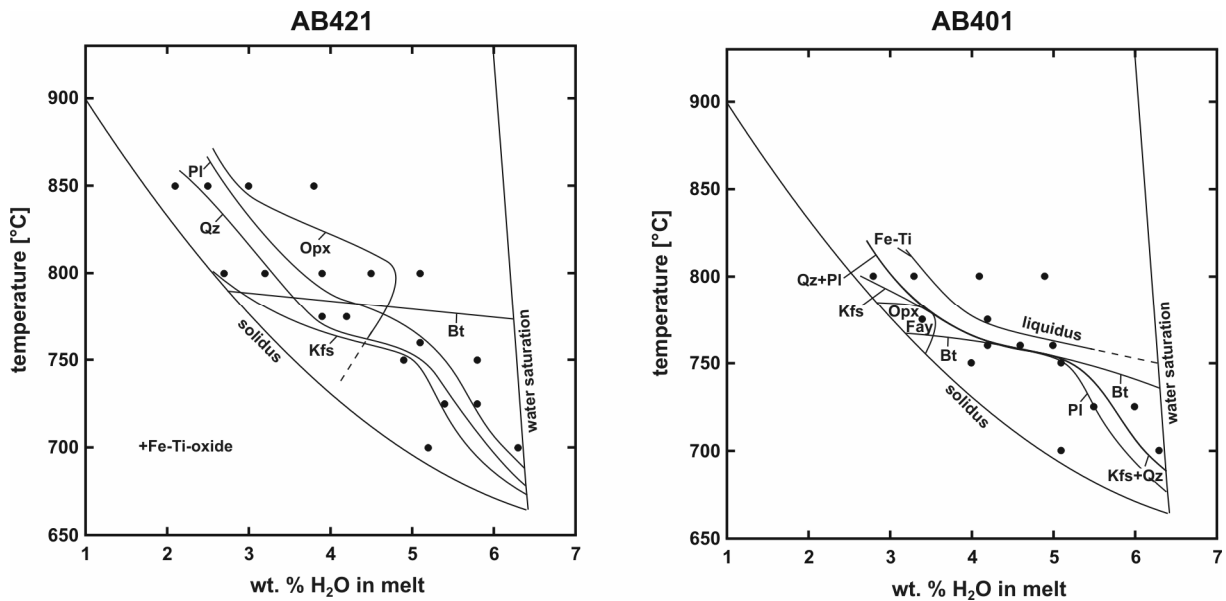


Figure 2.2: Phase relations for composition AB421 and composition AB401 as a function of temperature – melt H_2O content at 200 MPa and $f\text{O}_2 \sim \text{NNO}$. Solid dots represent experimental charges at given run conditions. Mineral abbreviations as given by Kretz (1983). Stability curves are labelled with mineral names lying inside their stability field. Uncertain portions of stability curves are indicated by dashed lines.

In the most felsic composition AB401 liquidus conditions were attained at melt H_2O contents ≥ 4 wt. % and temperatures ≥ 775 °C. For both compositions Fe-Ti oxides are the liquidus phases. In the less evolved composition AB421 near liquidus conditions could only be obtained at 850°C with a H_2O content of the melt > 3 wt. % and at 800 °C with ≥ 5 wt. % H_2O , respectively. With decreasing temperatures and for water content of the melt < 3.5 wt. % H_2O , the crystallisation of Fe-Ti-oxide is followed by orthopyroxene, plagioclase and quartz. The orthopyroxene stability field is restricted to high temperatures above 750°C and melt H_2O contents < 5 wt. %. Biotite occurs at 775 °C and below. Within the resolution of our experiments the biotite stability is not or slightly affected by a H_2O . When compared to AB421 biotite crystallises at lower temperatures

in AB401 (750 to 760 °C). In AB401 the crystallisation of Fe-Ti-oxide is followed by quartz + plagioclase at H₂O contents of the melt <3.5 wt. %. At H₂O contents of the melt between 3.5 to 5 wt. %, quartz, plagioclase, K-feldspar and biotite crystallise nearly simultaneously in the temperature range 750-775°C, approximately 15 °C below the liquidus. At H₂O contents >5 wt. % Fe-Ti-oxide crystallisation is followed by biotite and quartz + K-feldspar. Orthopyroxene plus olivine (fayalite) were observed in only one experiment at 775 °C and ~3.5 wt. % H₂O close to the solidus. In this experiment orthopyroxene crystals show dissolution reaction and fayalite crystal show idiomorph shapes, indicating a reaction with breakdown of orthopyroxene producing fayalite.

In both compositions at water saturated conditions plagioclase, quartz and K-feldspar crystallise below 700 °C, slightly above the estimated solidus.

2.4.2. Phase compositions

Phase compositions obtained for AB412 and AB422 are given in §1. In the following only phase composition obtained for AB421 and AB401 are described. Compositions of plagioclase, K-feldspar and orthopyroxene are give in Tables 2.3, 2.4 and 2.5, respectively.

Feldspars

Plagioclase and K-feldspar analyses are listed in Tables 2.3 and 2.4. The Anorthite content of plagioclases synthesised from AB421 decrease with decreasing temperature and melt H₂O content (or aH₂O). Assuming an analytical error of ±0.5 wt. % H₂O for melt H₂O contents, these Anorthite contents are similar to those obtained for AB412 and AB422 (§1) at identical temperatures and melt H₂O contents (Figure 2.3a). In runs with AB401 the Anorthite content of plagioclase, ranging from An09 to An12, shows no variation with temperature or water content of the melt. In contrast to the other compositions, the Or-contents of plagioclases in AB401 can

be relatively high especially for plagioclases crystallising at lower aH₂O (Figure 2.3b) which may be related to the low CaO content of the bulk composition and the shape of the feldspar solvus in the Ab-rich field of the An-Ab-Or diagram.

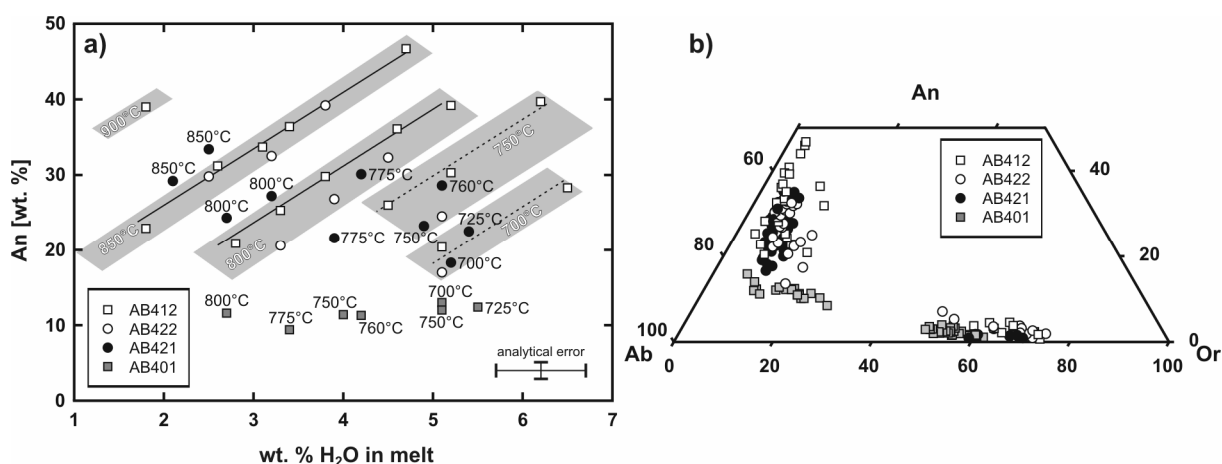


Figure 2.3: Compositions of feldspars. a) An content of plagioclase (average of analyses) as a function of melt H₂O content and temperature. Grey fields with white numbers indicate experimental temperatures for AB412 and AB422. Black numbers indicate run temperatures AB421 and AB401. Solid lines are linear fits for AB412 at 800 and 850°C. Dashed lines for 700 and 750°C have been constructed considering that the linear fits for given T are parallel in the diagram. The analytical error represents the maximal obtained standard deviation of plagioclase analyses of AB421 and AB401 (vertical bar, see Table 2.3) and the maximal error of water content determination (horizontal bar). b) plagioclase and K-feldspar compositions (all analyses) reported in the normative Ab-An-Or triangular diagram (in wt. %). Data for AB412 and AB422 (open squares and open circles) after §1. An content of experimental plagioclase of AB421 (filled circles) and AB401 (grey squares).

Orthopyroxene

As already mentioned in §1 a decrease of temperature and/or fO_2 results in a decrease of the XMg (Mg/Mg+Fe) in mafic minerals. At constant T, an increase of aH₂O results in an increase of fO_2 . Thus, the aH₂O and fO_2 change simultaneously and the individual effects of these two parameters on the XMg is difficult to determine. The XMg variation range of orthopyroxene compositions is lower for AB421 (0.29-0.42, Table 2.5) than for AB412 (0.30-0.59) and AB422 (0.30-0.56) but XMg is similar in the three compositions for identical T and aH₂O. Thus, the orthopyroxene composition in the studied systems depends on the prevailing run conditions and not on the starting bulk composition.

Table 2.3: Compositions of experimental plagioclase (wt. %) at 200 MPa and $\log f_{O_2} \sim NNO$

AB421																				
Run	60		77		64		80		84		85		72		52		57		56	
T [°C]	700	σ	725	σ	750	σ	760	σ	775	σ	775	σ	800	σ	800	σ	850	σ	850	σ
cH ₂ O ¹	5.2	n=6	5.4	n=6	4.9	n=3	5.1	n=5	4.2	n=7	3.9	n=5	3.2	n=7	2.7	n=1	2.5	n=5	2.1	n=4
SiO ₂	64.93	1.13	63.19	0.61	64.78	0.61	61.91	0.14	61.57	0.43	64.10	0.84	62.65	1.11	64.70		62.30	1.27	63.51	1.01
Al ₂ O ₃	21.81	0.69	22.91	0.45	21.82	0.43	23.70	0.41	24.05	0.45	22.63	0.25	23.07	0.98	22.87		23.51	0.89	22.76	0.43
Fe ₂ O ₃ ²	0.46	0.15	0.39	0.13	0.59	0.05	0.33	0.05	0.31	0.03	0.31	0.05	0.34	0.08	0.28		0.36	0.05	0.30	0.18
CaO	3.62	0.19	4.54	0.32	4.36	0.35	5.81	0.17	6.13	0.35	4.30	0.14	5.33	0.49	4.87		6.50	0.56	5.71	0.44
Na ₂ O	7.91	0.19	7.72	0.15	6.81	0.15	7.38	0.12	7.25	0.05	7.39	0.17	7.07	0.31	7.31		6.40	0.30	6.77	0.20
K ₂ O	1.58	0.19	1.38	0.21	1.66	0.31	0.94	0.05	0.92	0.08	1.88	0.16	1.20	0.25	1.67		1.14	0.22	1.31	0.26
Total	100.30		100.12		100.02		100.06		100.23		100.61		99.65		101.70		100.20		100.36	
An	18.3	1.1	22.5	1.5	23.4	1.4	28.6	0.8	30.1	1.4	21.6	1.0	27.2	1.9	24.3		33.4	2.2	29.2	1.7
Ab	72.2	0.6	69.4	0.8	66.0	1.9	65.8	0.6	64.5	1.0	67.1	0.5	65.4	1.4	65.9		59.6	1.7	62.8	0.6
Or	9.5	1.1	8.1	1.2	10.6	1.0	5.5	0.4	5.4	0.5	11.2	0.8	7.3	1.8	9.9		7.0	1.5	8.0	1.8
AB401																				
Run	63		79		66		67		83		87		68							
T [°C]	700	σ	725		750	σ	750	σ	760	σ	775	σ	800	σ						
cH ₂ O ¹	5.1	n=5	5.5	n=1	5.1	n=3	4.0	n=4	4.2	n=4	3.4	n=3	2.7	n=2						
SiO ₂	65.62	0.45	65.24		65.12	0.40	66.22	0.49	66.09	0.45	66.65	0.36	66.38	0.02						
Al ₂ O ₃	21.57	0.38	21.16		20.83	0.22	20.43	0.61	20.59	0.51	20.36	0.17	20.72	0.00						
Fe ₂ O ₃ ²	0.31	0.11	0.20		0.34	0.03	0.21	0.03	0.41	0.19	0.16	0.02	0.18	0.07						
CaO	2.64	0.34	2.54		2.48	0.21	2.28	0.19	2.27	0.19	1.88	0.16	2.29	0.15						
Na ₂ O	8.65	0.12	7.85		7.93	0.31	7.73	0.42	7.76	0.16	7.23	0.05	7.65	0.10						
K ₂ O	1.66	0.27	3.12		3.19	0.12	3.08	0.55	3.20	0.41	4.31	0.25	3.10	0.12						
Total	100.44		100.12		99.89		99.95		100.31		100.58		100.32							
An	13.0	1.7	12.4		12.0	1.0	11.4	1.0	11.3	0.9	9.4	0.9	11.6	0.6						
Ab	77.2	0.4	69.4		69.6	1.2	70.1	2.9	69.8	1.5	65.1	0.3	69.8	0.3						
Or	9.7	1.6	18.2		18.4	0.9	18.4	3.5	18.9	2.4	25.6	1.2	18.6	0.9						

¹Water contents of residual glasses determined using the difference method (Devine et al., 1995).²Total Fe as Fe₂O₃.

Table 2.4: Compositions of experimental K-feldspar (wt. %) at 200 MPa and $\log f_{O_2} \sim NNO$

Run	AB421				AB401											
	60	64	63	79	66	67	83	87	63	79	66	67	83	87		
T [°C]	700	750	700	725	750	750	760	775								
cH ₂ O ¹	5.2	4.9	5.1	5.5	5.1	4.0	4.2	3.4								
SiO ₂	65.96	66.47	66.76	66.17	66.88	66.56	66.20	66.76								
Al ₂ O ₃	18.58	18.67	18.71	19.13	18.82	18.70	18.91	18.89								
Fe ₂ O ₃ ²	0.27	0.24	0.12	0.21	0.13	0.11	0.34	0.19								
CaO	0.26	0.34	0.38	0.64	0.46	0.39	0.49	0.64								
Na ₂ O	3.34	4.08	4.40	4.64	5.06	4.59	4.81	5.15								
K ₂ O	11.42	9.73	9.58	9.19	8.66	9.29	9.42	8.46								
Total	99.83	99.52	99.95	99.97	100.01	99.64	100.16	100.08								
An	1.3	1.8	1.9	3.2	2.3	2.0	2.4	3.2								
Ab	30.4	38.2	40.3	42.1	45.9	42.0	42.7	46.5								
Or	68.3	60.0	57.8	54.7	51.8	56.0	54.9	50.3								

¹Water contents of residual glasses determined using the difference method (Devine et al., 1995).

²Total Fe as Fe₂O₃.

Table 2.5: Compositions of experimental orthopyroxene (wt. %) at 200 MPa and $\log f_{\text{O}_2} \sim \text{NNO}$

Run	AB421																AB401	
	84		85		74		73		72		52		57		56		775	
T [°C]	775	σ	775	σ	800	σ	800	σ	800	σ	800	σ	850	σ	850	σ	87	σ
ΔNNO^1	-0.32	n=4	-0.49	n=4	-0.20	n=5	-0.30	n=6	-0.32	n=6	-0.59	n=3	-0.62	n=4	-0.75	n=3	-0.47	n=2
SiO ₂	50.05	0.14	48.32	0.45	50.18	0.28	50.00	0.59	51.04	1.15	50.38	0.47	50.50	0.36	52.33	0.23	49.06	0.37
TiO ₂	0.11	0.02	0.13	0.02	0.12	0.03	0.13	0.02	0.12	0.01	0.19	0.01	0.11	0.03	0.13	0.02	0.10	0.02
Al ₂ O ₃	1.06	0.05	1.18	0.21	0.66	0.08	0.92	0.21	1.81	0.57	2.29	0.11	0.90	0.21	2.01	0.28	0.99	0.12
FeO ²	33.44	0.22	36.51	1.17	32.27	0.32	32.57	0.95	32.23	1.61	35.58	0.76	31.74	0.33	30.48	0.66	34.47	0.66
MnO	1.82	0.08	2.16	0.04	1.70	0.12	1.67	0.08	1.61	0.13	1.66	0.06	1.60	0.04	1.64	0.03	1.54	0.02
MgO	11.12	0.11	8.52	0.30	12.87	0.15	11.98	0.43	9.88	0.77	8.84	0.11	12.74	0.27	12.12	0.51	9.27	0.40
CaO	1.21	0.02	1.13	0.33	1.13	0.09	1.24	0.10	1.35	0.15	1.27	0.19	1.30	0.13	1.23	0.12	0.76	0.07
Na ₂ O	0.08	0.01	0.04	0.01	0.05	0.02	0.05	0.03	0.17	0.18	0.19	0.01	0.04	0.01	0.24	0.10	0.17	0.10
K ₂ O	0.15	0.02	0.12	0.08	0.06	0.01	0.08	0.05	0.37	0.22	0.32	0.02	0.07	0.01	0.40	0.07	0.23	0.10
Total	99.04		98.11		99.04		98.66		98.58		100.73		99.01		100.58		96.60	
XMg	0.37	0.00	0.29	0.01	0.42	0.00	0.40	0.01	0.35	0.01	0.31	0.01	0.42	0.01	0.41	0.01	0.32	0.01
En	34.9	0.3	27.4	1.0	39.2	0.3	37.3	1.3	32.8	1.1	28.6	0.5	39.3	0.7	38.7	1.2	30.6	0.6
Fs	62.1	0.3	69.8	1.7	58.1	0.3	59.7	1.3	63.2	0.2	67.6	1.0	57.7	0.8	57.5	1.5	66.8	0.3
Wo	2.7	0.1	2.6	0.7	2.5	0.2	2.8	0.2	3.2	0.3	3.0	0.5	2.9	0.3	2.8	0.3	1.8	0.1

¹ $\Delta\text{NNO} = \log f_{\text{O}_2} (\text{experiment}) - \log f_{\text{O}_2} (\text{NNO}; \text{Chou}, 1987)$.

²Total Fe as FeO.

Table 2.6: Compositions of experimental glasses (wt. %, normalised to 100) of AB421 at 200 MPa and $\log f_{O_2} \sim NNO$

Run	61	σ	60	σ	76	σ	77	σ	65	σ	64	σ	80	σ	84	σ	85	σ
T [°C]	700	n=6	700	n=8	725	n=8	725	n=6	750	n=6	750	n=10	760	n=7	775	n=7	775	n=6
SiO ₂	77.66	0.34	77.36	0.46	77.10	0.40	76.91	0.42	78.06	0.41	76.92	0.35	77.66	0.39	77.80	0.42	76.93	0.31
TiO ₂	0.06	0.02	0.08	0.03	0.06	0.03	0.07	0.04	0.09	0.04	0.08	0.03	0.12	0.02	0.11	0.03	0.09	0.02
Al ₂ O ₃	12.68	0.20	13.01	0.20	12.97	0.08	13.00	0.20	12.75	0.06	13.40	0.20	12.75	0.13	12.44	0.15	12.81	0.25
FeO ¹	0.90	0.04	1.10	0.14	0.93	0.10	1.03	0.26	0.59	0.14	1.15	0.22	0.85	0.12	0.99	0.19	1.11	0.14
MnO	0.02	0.02	0.08	0.07	0.08	0.04	0.10	0.09	0.04	0.04	0.12	0.07	0.01	0.01	0.01	0.01	0.06	0.05
MgO	0.07	0.04	0.03	0.03	0.09	0.04	0.07	0.03	0.04	0.03	0.01	0.01	0.04	0.02	0.08	0.02	0.05	0.03
CaO	0.81	0.09	0.47	0.06	0.78	0.05	0.53	0.08	0.74	0.10	0.33	0.04	0.66	0.06	0.63	0.08	0.39	0.04
Na ₂ O	3.21	0.14	3.06	0.15	3.14	0.17	3.06	0.09	3.17	0.19	3.14	0.27	3.00	0.25	2.99	0.13	2.99	0.14
K ₂ O	4.59	0.16	4.82	0.11	4.84	0.11	5.22	0.16	4.52	0.11	4.85	0.15	4.91	0.16	4.96	0.09	5.57	0.09
Total	100.00		100.00		100.00		100.00		100.00		100.00		100.00		100.00		100.00	
cH ₂ O ²	6.3		5.2		5.8		5.4		5.8		4.9		5.1		4.2		3.9	
Qz	41.7	1.5	41.9	1.4	40.6	1.8	39.5	0.7	42.9	1.2	41.0	2.5	41.9	1.2	41.8	0.8	38.5	1.2
Ab	29.2	1.4	27.7	1.3	28.6	1.6	27.6	0.7	28.6	1.7	28.4	2.4	27.1	2.2	27.0	1.2	26.7	1.3
Or	29.1	1.0	30.4	0.7	30.8	0.7	32.9	1.0	28.5	0.9	30.6	0.9	30.9	1.2	31.2	0.6	34.8	0.5
Run	75	σ	74	σ	73	σ	72	σ	52	σ	59	σ	58	σ	57	σ	56	σ
T [°C]	800	n=14	800	n=7	800	n=9	800	n=10	800	n=9	850	n=11	850	n=14	850	n=12	850	n=9
SiO ₂	76.88	0.38	76.89	0.32	76.70	0.34	77.03	0.35	76.95	0.32	76.99	0.28	76.98	0.36	77.15	0.42	77.33	0.33
TiO ₂	0.14	0.02	0.14	0.04	0.14	0.05	0.15	0.03	0.16	0.04	0.15	0.03	0.15	0.02	0.16	0.02	0.17	0.03
Al ₂ O ₃	12.68	0.20	12.67	0.18	12.65	0.26	12.72	0.14	12.76	0.11	12.75	0.15	12.74	0.15	12.68	0.15	12.65	0.24
FeO ¹	1.42	0.22	1.33	0.13	1.36	0.21	1.20	0.18	1.22	0.13	1.41	0.16	1.36	0.14	1.29	0.21	1.19	0.19
MnO	0.07	0.04	0.09	0.09	0.04	0.02	0.01	0.01	0.05	0.05	0.05	0.04	0.05	0.05	0.07	0.06	0.03	0.06
MgO	0.16	0.04	0.15	0.03	0.15	0.03	0.09	0.03	0.09	0.03	0.18	0.03	0.19	0.03	0.17	0.02	0.16	0.03
CaO	0.81	0.07	0.83	0.10	0.79	0.09	0.59	0.07	0.49	0.03	0.85	0.04	0.87	0.07	0.79	0.03	0.62	0.04
Na ₂ O	3.14	0.16	3.17	0.19	3.41	0.11	3.30	0.23	3.02	0.09	3.04	0.11	3.11	0.08	3.13	0.11	3.04	0.09
K ₂ O	4.71	0.18	4.74	0.21	4.76	0.15	4.92	0.14	5.26	0.19	4.58	0.10	4.55	0.09	4.56	0.17	4.81	0.08
Total	100.00		100.00		100.00		100.00		100.00		100.00		100.00		100.00		100.00	
cH ₂ O ²	5.1		4.5		3.9		3.2		2.7		3.8		3.0		2.5		2.1	
Qz	40.8	1.9	40.5	2.1	38.4	1.6	39.2	1.7	39.6	1.3	42.2	0.8	41.9	1.0	41.9	1.7	41.7	1.0
Ab	28.9	1.4	29.1	1.8	31.2	1.0	29.8	2.0	27.2	0.8	28.2	1.1	28.7	0.7	28.8	1.0	27.7	0.8
Or	30.3	1.1	30.4	1.3	30.4	0.9	31.0	1.0	33.2	1.1	29.6	0.7	29.4	0.6	29.3	1.1	30.6	0.6

¹Total Fe as FeO.²Water contents determined using the difference method (Devine et al., 1995).

Table 2.7: Compositions of experimental glasses (wt. %, normalised to 100) of AB401 at 200 MPa and $\log f_{O_2} \sim NNO$

Run	62	s	63	s	78	s	79	s	66	s	67	s	81	s	82	s	83	s
T [°C]	700	n=8	700	n=11	725	n=7	725	n=7	750	n=6	750	n=11	760	n=10	760	n=8	760	n=10
SiO ₂	78.44	0.19	77.83	0.27	77.98	0.45	77.66	0.25	78.09	0.28	77.78	0.41	77.71	0.35	77.79	0.22	77.38	0.30
TiO ₂	0.06	0.05	0.07	0.04	0.07	0.03	0.09	0.02	0.07	0.02	0.09	0.04	0.06	0.02	0.07	0.03	0.08	0.04
Al ₂ O ₃	12.27	0.11	12.63	0.19	12.57	0.14	12.38	0.13	12.52	0.21	12.45	0.18	12.52	0.15	12.50	0.19	12.62	0.20
FeO ¹	0.64	0.14	0.90	0.09	0.74	0.09	0.84	0.09	0.86	0.23	0.70	0.06	0.75	0.12	0.75	0.13	0.86	0.13
MnO	0.00	0.01	0.02	0.01	0.03	0.01	0.04	0.04	0.06	0.01	0.00	0.00	0.07	0.04	0.06	0.04	0.06	0.04
MgO	0.01	0.01	0.01	0.01	0.05	0.03	0.04	0.04	0.04	0.02	0.00	0.00	0.06	0.03	0.04	0.02	0.03	0.02
CaO	0.40	0.04	0.32	0.05	0.42	0.03	0.43	0.09	0.33	0.07	0.35	0.05	0.42	0.06	0.42	0.06	0.34	0.07
Na ₂ O	3.37	0.28	3.57	0.15	3.11	0.15	3.44	0.17	3.34	0.20	3.62	0.25	3.35	0.13	3.34	0.22	3.45	0.17
K ₂ O	4.81	0.12	4.66	0.12	5.03	0.15	5.07	0.10	4.70	0.22	5.00	0.12	5.05	0.14	5.02	0.16	5.19	0.17
Total	100.00		100.00		100.00		100.00		100.00		100.00		100.00		100.00		100.00	
cH ₂ O ²	6.3		5.1		6.0		5.5		5.1		4.0		5.0		4.6		4.2	
Qz	40.7	2.0	39.6	1.3	41.1	1.4	38.3	1.8	41.2	2.1	37.6	2.4	39.1	1.3	39.3	1.6	37.5	1.4
Ab	29.7	2.4	31.6	1.2	27.7	1.4	30.4	1.5	29.7	1.8	31.8	2.2	29.7	1.2	29.6	1.8	30.5	1.4
Or	29.6	0.8	28.8	0.7	31.2	0.9	31.3	0.6	29.1	1.3	30.6	0.7	31.2	0.8	31.1	1.0	32.0	1.0
Run	86	s	87	s	71	s	70	s	69	s	68	s						
T [°C]	775	n=9	775	n=11	800	n=7	800	n=9	800	n=10	800	n=13						
SiO ₂	77.86	0.32	77.38	0.31	77.58	0.30	77.88	0.37	77.81	0.39	77.68	0.44						
TiO ₂	0.07	0.03	0.10	0.03	0.10	0.03	0.09	0.03	0.10	0.02	0.09	0.03						
Al ₂ O ₃	12.50	0.17	12.54	0.12	12.34	0.19	12.20	0.20	12.35	0.24	12.45	0.20						
FeO ¹	0.69	0.17	0.87	0.11	1.00	0.13	0.94	0.17	1.01	0.17	0.71	0.14						
MnO	0.06	0.03	0.05	0.04	0.07	0.01	0.04	0.01	0.00	0.00	0.05	0.05						
MgO	0.06	0.03	0.06	0.02	0.05	0.02	0.04	0.02	0.06	0.04	0.06	0.03						
CaO	0.41	0.04	0.30	0.07	0.43	0.06	0.46	0.03	0.44	0.06	0.33	0.06						
Na ₂ O	3.37	0.12	3.33	0.19	3.47	0.23	3.48	0.16	3.46	0.18	3.49	0.25						
K ₂ O	4.97	0.17	5.38	0.12	4.94	0.12	4.87	0.17	4.75	0.17	5.14	0.14						
Total	100.00		100.00		100.00		100.00		100.00		100.00							
cH ₂ O ²	4.2		3.4		4.9		4.1		3.2		2.7							
Qz	39.4	1.0	37.5	1.7	38.5	1.7	39.0	1.5	39.6	2.1	37.7	1.9						
Ab	29.8	1.1	29.4	1.6	30.9	1.9	30.9	1.4	30.8	1.5	30.7	2.2						
Or	30.7	0.9	33.1	0.6	30.6	0.8	30.1	1.1	29.5	1.0	31.6	1.0						

¹Total Fe as FeO.²Water contents determined using the difference method (Devine et al., 1995).

Oxides

Oxide minerals are present in all runs except in liquidus experiments with composition AB401. The very small crystal size ($\leq 2 \mu\text{m}$), especially in water undersaturated charges, makes it difficult to obtain reliable analyses. However, when the crystal size was large enough to allow accurate analysis, a systematical change in composition could be observed with changing experimental conditions. All oxides are identified as magnetite. A maximum TiO_2 content of ~ 15 wt. % is observed at 900°C and $a_{\text{H}_2\text{O}} = 1.0$ in composition AB412 (§1). Decreasing run temperature and/or $a_{\text{H}_2\text{O}}$ result in decreasing TiO_2 (~ 3 wt. %) with increasing FeO (max. $\text{FeO}_{\text{total}} = 85$ wt. %). Al_2O_3 content is up to ~ 2 wt. %. MgO increases with temperature from 0.1 wt. % at 700°C to 1.1 wt. % at 850°C . The MnO content of magnetite is < 1 wt. % irrespective of the experimental conditions. An influence of the starting glass composition on the compositions of Fe-Ti-oxides could not be determined.

Biotite

Biotite crystals are very small in water undersaturated charges with high crystal contents. Although the analyses of biotite are of lower quality, the XMg decreases from 0.5 to 0.3 with decreasing temperature and decreasing f_{O_2} in agreement with Dall'Agnol et al. (1999). TiO_2 of experimental biotite is ≤ 3 wt. %.

Fayalite

Sparse idiomorph fayalite crystals with XMg = 0.23 (MnO = 1.6 wt. %) were only detected in run 87 with composition AB401 at near solidus conditions (775°C , 3.4 wt. % H_2O in melt).

Experimental glasses

Quenched glass compositions of AB421 and AB401 normalised to 100 wt. % (anhydrous) are reported in Tables 2.6 and 2.7. The glass compositions of experiments performed with AB12, AB422, AB421 and AB401 are presented in Figure 2.4 (element oxide versus melt H₂O contents in wt. %).

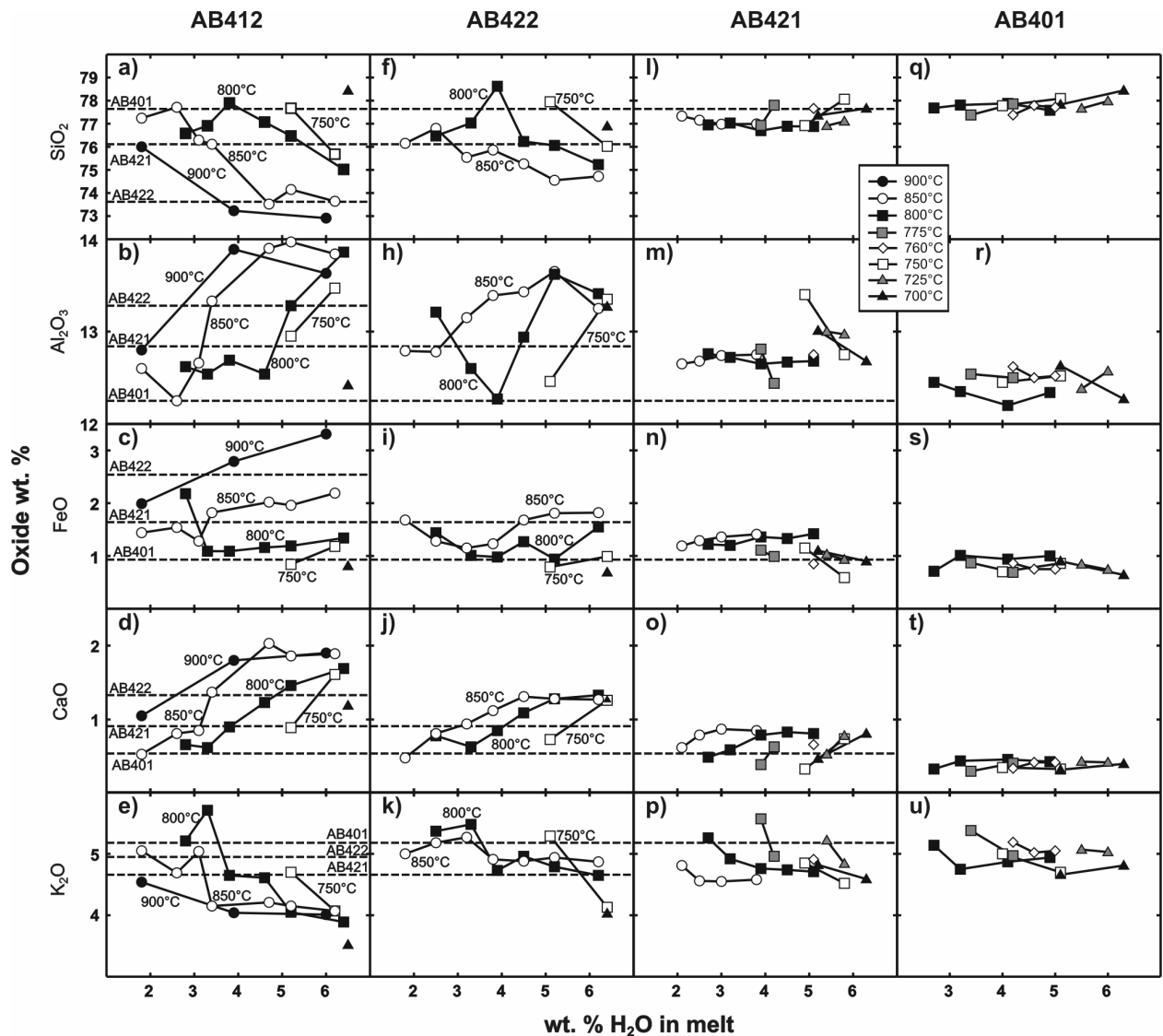


Figure 2.4a-u: Variations of selected element oxide concentrations (y-axis) of experimental glasses of all runs (in wt. %) as a function of melt H₂O content (x-axis), temperature (symbol legend in box) and starting composition (vertical columns). Data for AB412 and AB422 taken from §1. Dashed horizontal lines indicate the starting bulk compositions of AB422, AB421 and AB401. TiO₂, MgO and MnO are not presented because of their low abundance in the bulk compositions. Na₂O is not presented because it does not vary much over the Wangrah Suite granites.

Glass compositions from experiments near to or above liquidus temperatures are always close to the starting bulk composition. In general SiO_2 and K_2O contents increase with decreasing temperature and $a_{\text{H}_2\text{O}}$. Al_2O_3 , FeO and CaO contents decrease with decreasing temperature and $a_{\text{H}_2\text{O}}$. The broadest variation of glass composition with melt H_2O contents and temperature is observed for the most mafic composition AB412 (Figure 2.4a-e). The residual glass compositions of the most evolved composition AB401 (Figure 2.4q-u) are always close to the initial bulk composition and show little variation with changing experimental run conditions.

Figure 2.4 can be used to illustrate the effect of decreasing water activity on melts coexisting with mineral phases. For example, in AB412 at 800°C , SiO_2 increases up to ~ 78 wt. % with decreasing $c_{\text{H}_2\text{O}}$ down to ~ 3.5 wt. % (Figure 2.4a, black squares) as a result of crystallisation of phases with lower SiO_2 concentrations than the starting bulk composition (see Table 2.2, runs 1, 25 and 7). With further decrease of $c_{\text{H}_2\text{O}}$ (< 3.5 wt. %) the SiO_2 content of the melt decreases. In these latter experiments quartz coexists with the glasses. Thus, the decrease of SiO_2 cannot be related to an increase in SiO_2 activity but most probably results from changing activity-composition relationships. The role of plagioclase crystallisation due to the decrease of $a_{\text{H}_2\text{O}}$ is illustrated in Figure 2.4j. The maximum CaO contents of melts are similar to the bulk compositions and decrease as soon as plagioclase starts to crystallise (e.g., at 850°C and $c_{\text{H}_2\text{O}} < 4$ wt. %). The $a_{\text{H}_2\text{O}}$ influences the distribution of CaO between melt and plagioclase as well as the proportions of liquid and solid. Thus, the decreasing $a_{\text{H}_2\text{O}}$ leads to a decrease of CaO in both melt and plagioclase with decreasing $a_{\text{H}_2\text{O}}$ (see also Figure 2.3a) and an increase of the ratio solid/liquid.

2.4.3. Phase proportions

Phase proportions have been determined by mass balance calculations with least squares minimization (Le Maitre, 1976) to constrain crystal/melt proportions in the experimental

products of compositions AB412, AB422, AB421 and AB401 (Table 2.2). Calculations have been performed using the compositions of the experimental phases, in particular glass, of the corresponding experiment. Phase proportions were not calculated for runs in which the glass composition is determined with a high uncertainty (due to small melt fractions; e.g., runs 21, 22; in §1). If present, biotite and magnetite have to be taken into account for mass balance calculations, but, as mentioned above, some magnetite and biotite analyses are of poor quality due to the small grain sizes, especially in water undersaturated experiments. In this case stoichiometric analyses of minerals from neighbouring charges were used to extrapolate the FeO-TiO₂ contents (for magnetite) and FeO-MgO contents (for biotite) at the relevant experimental conditions. Calculations with corrected magnetite and biotite compositions have a least squares fit with slightly better residuals than those performed with uncorrected ones. However, the comparison of calculated weight proportions with corrected and uncorrected data shows that there is no significant change of phase proportions, especially for plagioclase, K-feldspar and quartz (less than 5%). All calculations have been carried out with glass analyses normalised to 100 wt. % (on anhydrous basis). Residuals are always below unity suggesting that no major phase has been overlooked and that quenched glasses have been analysed correctly (i.e. no significant alkali-loss, reasonable totals).

The calculated crystal contents are plotted in the experimentally determined phase diagrams (Figure 2.5). Phase proportion curves mainly depend on the appearance of the SiO₂-rich phases plagioclase, alkali feldspar and quartz and reflect the shape of the stability curves of tectosilicates. As expected, the lowest crystal contents are observed at near liquidus conditions (high T and cH₂O). Consequently, within one bulk composition, the amount of plagioclase, quartz or K-feldspar increases towards the solidus with decreasing aH₂O at constant temperatures or with decreasing temperature at constant aH₂O, respectively (Table 2.2). The ratio of these phases is a function of the bulk composition. In AB412 plagioclase dominates the

mode (up to 27 wt. %). K-feldspar dominates the mode in the most felsic composition AB401 (up to 30 wt. %). Maximum amounts of mafic minerals decrease from ~11 wt. % (AB412) to ~9.5 (AB422), 5.5 wt. % (AB421) and <2 wt. % (AB401).

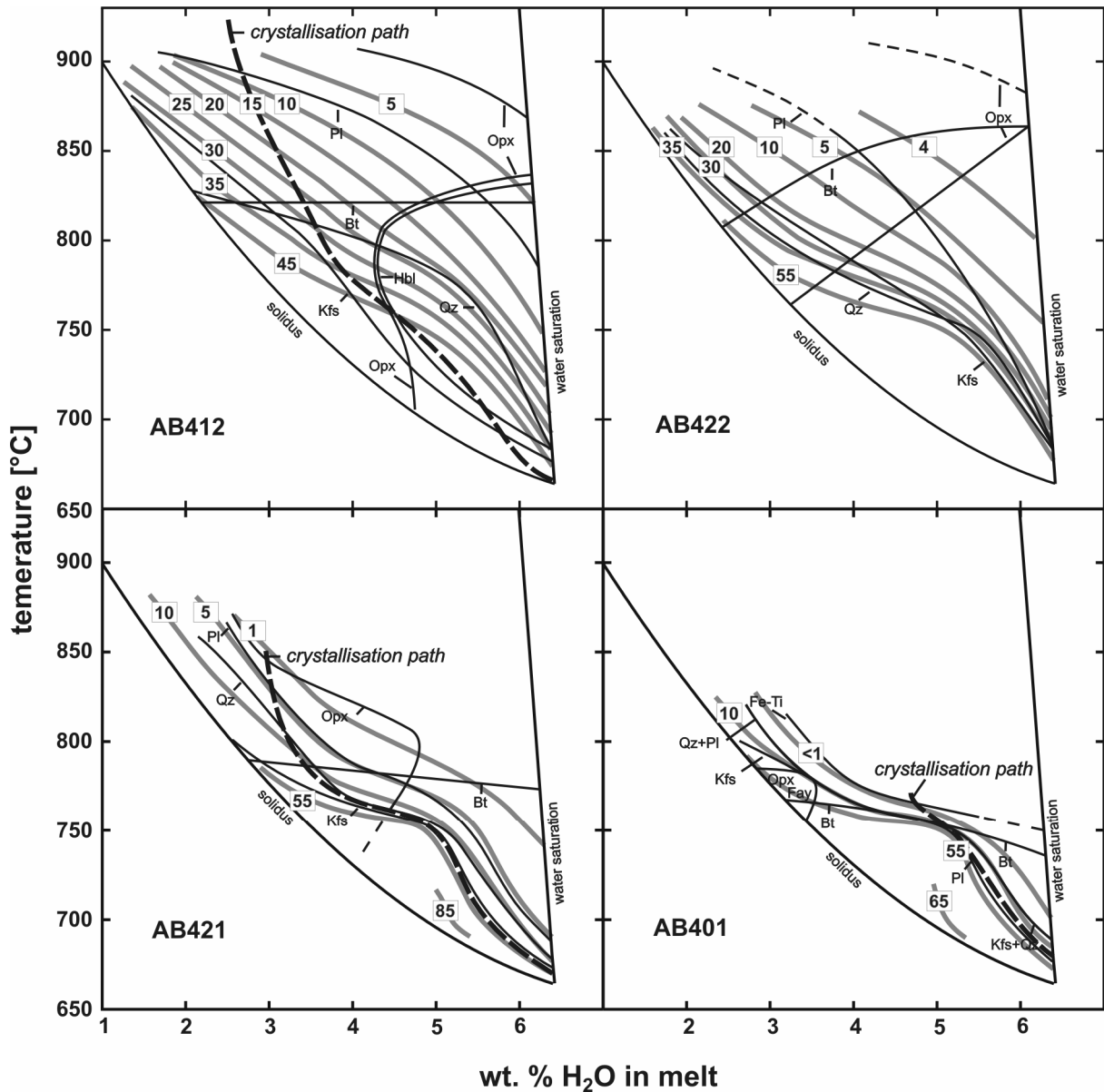


Figure 2.5: Comparison of calculated crystal contents in the experimentally determined temperature versus melt H₂O contents phase diagrams of AB412, AB422, AB421 and AB401. Grey lines with numbers in boxes represent the calculated crystal content (in wt. %) as given in Table 2. Note the depression of crystal content curves from AB412 to AB401 with decreasing liquidus temperature for crystal contents below ~50 wt. % but all compositions are ~50 wt. % crystallised at temperatures ~750 °C with H₂O contents of the melt of 4-5 wt. %. Dashed curves represent the calculated crystallisation paths for a closed system with initial water contents of 2.5 wt. % (AB412), 3 wt. % (AB421) and 4.7 wt. % (AB401) with H₂O as the only volatile.

At water saturated conditions a crystal content of 5 wt. % is observed in AB412 at ~825 °C (Figure 2.5). In the more felsic compositions this crystal content of 5 wt. % is attained at lower temperatures (750 °C for AB422, 750-700 °C for AB421 and <700 °C for AB401). Thus, the temperature interval between liquidus and solidus is >200°C for composition AB412 and <100°C for the most felsic composition AB401 (at $a_{\text{H}_2\text{O}} = 1$). This depression of crystal contents to lower temperatures with increasing felsic character of the starting composition is also observed for experiments at $a_{\text{H}_2\text{O}} < 1$ as long as the crystal contents are relatively low (below ~50 wt. %). However, it can be noted that the curve representing the 50 wt. % crystal boundary (Figure 2.5) does not differ significantly in the four investigated compositions, in particular for AB422, AB421 and AB401. A crystal content of ~50 wt. % is observed at 750 °C with H_2O contents of the melt of 4 to 5 wt. % in these compositions.

2.5. Discussion and applications of experimental results

This study provides information on phase relations at emplacement conditions (200 MPa, King et al., 2001) of the whole compositional variation of the Wangrah Suite. In the following section the experimental results and the chemical compositions of natural bulk rocks and minerals are used to model crystal fractionation processes, to understand the mechanisms leading to chemical variations and to constrain the physical properties (viscosity, density) of the magmas.

2.5.1. Comparison of experimentally determined phase relations

As mentioned above, besides temperature and $a_{\text{H}_2\text{O}}$, phase stabilities are a function of bulk rock composition (increasing felsic character from AB412 to AB401). A comparison of mineral stability curves for main rock forming minerals is presented in Figure 2.6.

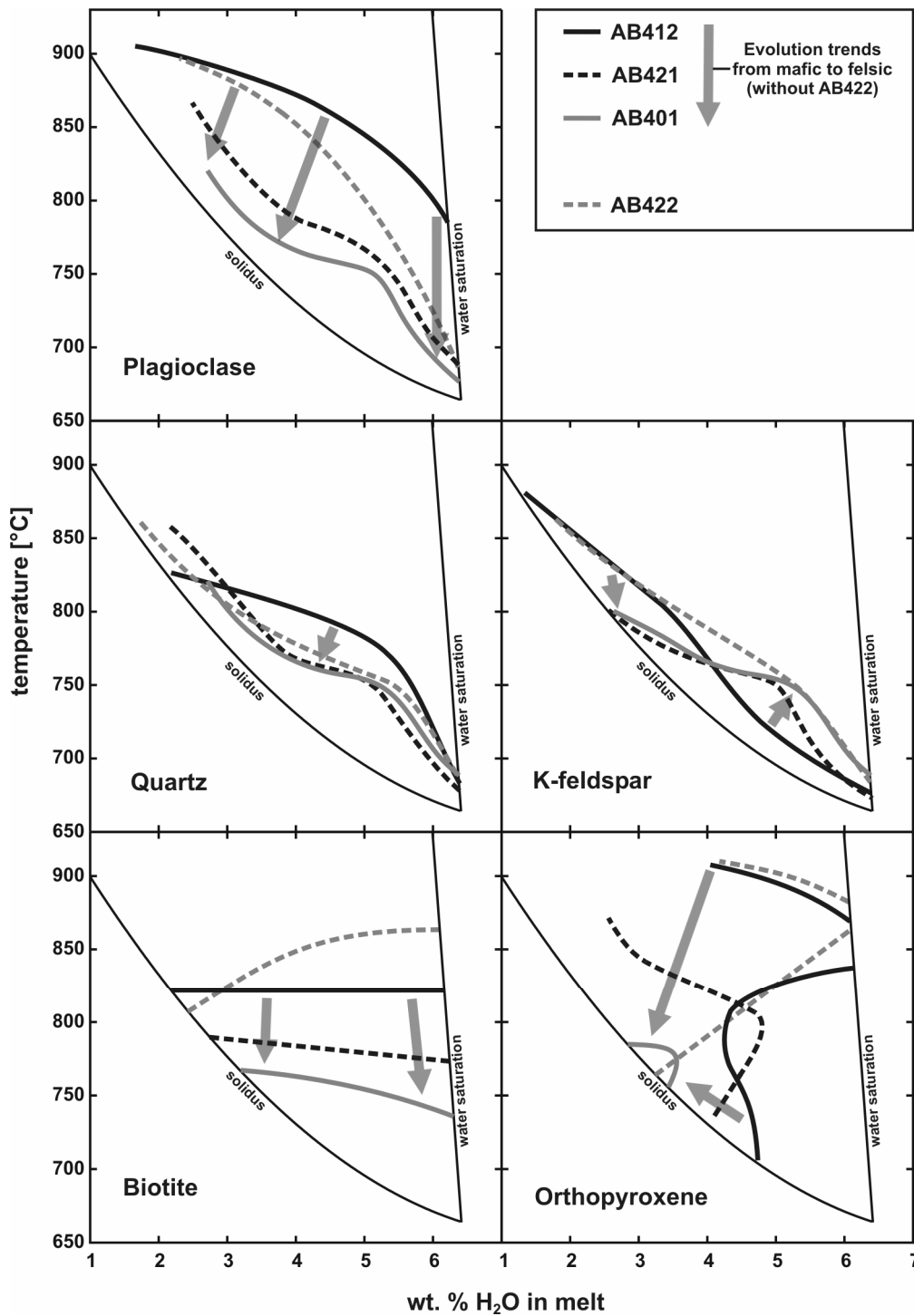


Figure 2.6: Comparison of the experimental determined phase stability curves of plagioclase, quartz, K-feldspar, biotite and orthopyroxene as a function of starting bulk composition in the temperature versus melt H_2O contents phase diagram. AB412 (solid black) and AB422 (dashed grey) after §1; AB421 (dashed black) and AB401 (solid grey) this study. Grey arrows indicate trends for the occurrence of observed phases from the most mafic composition AB412 to the most evolved composition AB401 excluding AB422. Note the broadest stability fields of the K_2O bearing phases K-feldspar and biotite of AB422 compared to all other compositions.

Plagioclase stability field decreases and is shifted to lower temperature from AB412 to AB401 with decreasing bulk CaO contents in the starting material (Table 2.1). Quartz stability only slightly depends on starting composition. Within the resolution of the experiments quartz crystallises at similar temperatures at a given aH₂O in AB422, AB421 and AB401. In the most mafic composition AB412 quartz stability is slightly shifted to higher temperatures at water contents of the melt of 4-5 wt. %. Quartz was not found in experiments with AB412 at 850°C but is expected to crystallise at near solidus conditions but at lower aH₂O compared to AB422 and AB421. K-feldspar stability decreases to lower temperature (from >800°C to ≤775 °C) for H₂O contents of the melt of 3-4 wt. % but is shifted to higher temperatures (≤700°C to 750 °C) for H₂O contents of the melt of ~5 wt. % with increasing K₂O content of the starting material from AB412 to AB401 (Table 2.1), excluding composition AB422. In experiments with AB422 K-feldspar crystallises over the widest range of temperature and aH₂O compared to the other compositions. This is most probably related to the high K₂O content of AB422 (Table 2.1) which may also explain for the stability field of biotite in this composition. Biotite crystallises above 850°C in AB422 at H₂O contents of the melt ≥5 wt. % and above 800°C at lower H₂O contents. In all other compositions maximum biotite crystallisation temperatures are lower and decrease with increasing felsic character of the starting composition (800-850°C for AB412, 775-800°C for AB421 and <775°C for AB401), nearly independently on the melt H₂O content. The orthopyroxene stability field decreases and is shifted towards lower temperature and aH₂O with decreasing bulk FeO and MgO contents.

As discussed below the evolution of stability fields of tectosilicates with increasing felsic character (Figure 2.6) can be explained by considering the phase relationships in the synthetic system Qz-Ab-Or-An-H₂O.

2.5.2 Projection of natural compositions in the ternary system and implications for the crystallisation sequence

Plagioclase, K-feldspar and quartz stabilities can be discussed within the haplogranite system. In Figure 2.7 starting bulk rock compositions are plotted in the isobaric phase diagram Qz-Ab-Or at 200 MPa. The minimum temperature melt composition and temperature in the ternary Qz-Ab-Or system is shifted to higher normative Or contents and temperatures with decreasing aH₂O (Figure 2.7a). Strictly, the Qz-Ab-Or-H₂O system can not be applied to the natural Wangrah Suite granites because they contain normative An (Table 2.1). There are few systematic experimental studies in the system Qz-Ab-Or-An (James & Hamilton, 1969; Whitney, 1975). Using the data of James & Hamilton (1969) at water saturated conditions and 100 MPa and of Holtz et al. (1992) at water undersaturated conditions the positions of the minima projected on the Qz-Ab-Or plane are reported on Figure 2.7a for different Ab/An ratios (diamonds; Ab/An = 10.4, 4.0, 1.4) and aH₂O (crosses). The shift of the position of the minima as a function of both, the Ab/An ratio and the aH₂O, can be extrapolated by a simple regression using these experimental data.

The Ab/An ratios of the Wangrah granites increase from 3 (AB412) to 4 (AB422), 6 (AB421) and 10 (AB401; Figure 2.7a). The corresponding water saturated minima and the line joining the water saturated and undersaturated minima (aH₂O = 1.0 and 0.25) are plotted in Figure 2.7b. The comparison of the projected composition of AB412 on the system Qz-Ab-Or-An-H₂O with the calculated minima for AB412 clearly shows that Ab-rich feldspar (plagioclase) is the first phase in the crystallisation sequence (Figure 2.7b; the bulk composition AB412 has a higher Ab content than the corresponding minima). Quartz is expected to crystallise after Ab-rich feldspar as soon as the residual melt reaches the cotectic line (see dotted curves in Figure 2.7b). This crystallisation sequence is confirmed by the experiments with AB412 with plagioclase as the first tectosilicate phase in the experimentally determined crystallisation sequence (Figure 2.5).

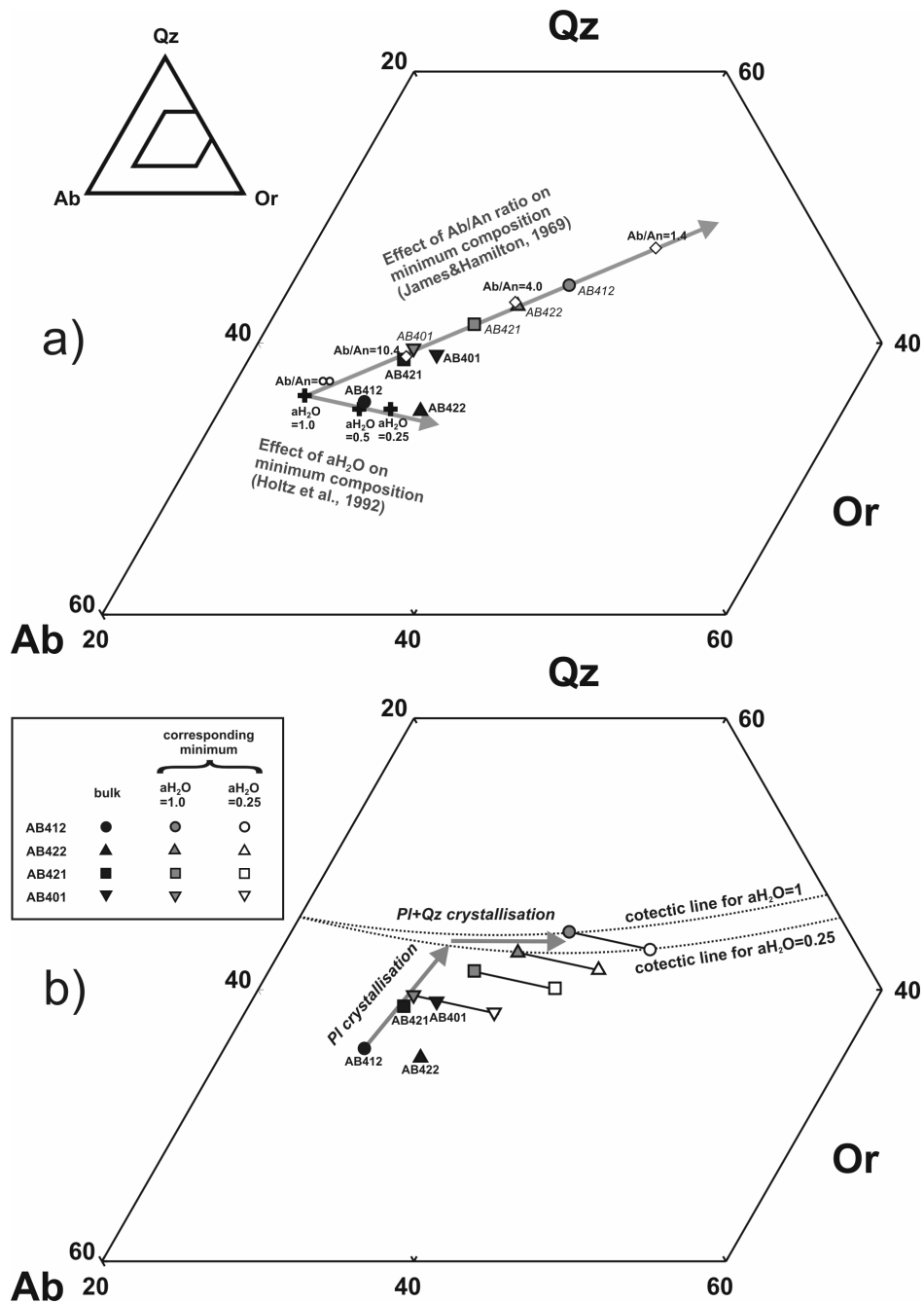


Figure 2.7: Estimated minimum temperature melt compositions in the haplogranitic system QzAbOr for the different starting bulk compositions AB412, AB422, AB421 and AB401 (black symbols) depending on the experimental a_{H_2O} . a) Effect of a_{H_2O} and An content on the minimum temperature melt composition. Crosses: experimental determined minimum temperature melt compositions at $a_{H_2O} = 0.25, 0.5$ and 1.0 after Holtz et al. (1992). White diamonds: experimental determined minimum temperature melt compositions for starting bulk Ab/An ratios of 10.4, 4.0, 1.4 at water saturated conditions after James & Hamilton (1969). Grey symbols: estimated minimum temperature melt composition for the studied bulk compositions at water saturated conditions for bulk Ab/An ratios of 3 (AB412), 4 (AB422), 6 (AB421) and 10 (AB401) assuming that they fall on a regression line of the data of James & Hamilton (1969) and Holtz et al. (1992, with an infinitesimal Ab/An ratio at $a_{H_2O} = 1.0$). b) Estimated minimum temperature melt compositions for a_{H_2O} of 0.25 to 1.0 crystallisation sequence for the studied bulk compositions. White symbols: estimated minimum temperature melt compositions at $a_{H_2O} = 0.25$ assuming that reducing a_{H_2O} at higher bulk An contents has the same effect on minimum temperature melt composition as shown by Holtz et al. (1992, solid lines). Dotted lines: cotectic curves for AB412 corresponding to a_{H_2O} s of 1.0 and 0.25 after Holtz et al. (1992). Grey arrows indicate the crystallisation sequence of AB412 (PI; PI+Qz; PI+Qz+Kfs).

The same crystallisation sequence is expected and observed for AB422 and AB421 because the bulk compositions are higher in normative Ab than the minima (Figure 2.7b). However, the compositional gap between the natural compositions and the corresponding minima decreases with increasing felsic character resulting in a decrease of plagioclase saturation temperatures (Figure 2.7b) and crystallisation temperatures (Figure 2.5).

The bulk composition AB401, projected on the Qz-Ab-Or (-An-H₂O) diagram, is identical with the minimum temperature melt composition at aH₂O ~ 0.7 (Figure 2.7b). This composition has a high Ab/An ratio and the phase relations obtained for the Ca-free system can be used to understand the stability fields of feldspars (Figure 2.8). The vertical line in Figure 2.8 represents the Ab/Or ratio of the minimum temperature melt composition for aH₂O = 0.7. Thus, following the phase relations in the Ca-free system, K-feldspar + quartz are expected to crystallise before Ab-rich feldspar at aH₂O >0.7 whereas Ab-rich feldspar + quartz are expected to crystallise before K-feldspar at aH₂O <0.7. The phase relations of AB401 (Figure 2.2) confirm that plagioclase crystallises at higher temperatures than K-feldspar at low aH₂O (e.g., 3 wt. % H₂O in the melt). In contrast K-feldspar crystallises at higher temperatures than plagioclase at high aH₂O (e.g., 6 wt. % H₂O in the melt). Nearly simultaneous crystallisation of K-feldspar, plagioclase and quartz is observed for melt H₂O contents of 3.5 to 5 wt. %.

The agreement between the synthetic and natural phase relations indicate that AB401 is compositionally close to a minimum temperature melt composition at 200 MPa and H₂O contents of the melt of 3.5 to 5 wt. % (aH₂O 0.5 to 0.7). In addition the Ab/Or ratio of AB401 (Ab47:Or53) corresponds to that observed for the minima in the range aH₂O = 0.7-0.5 (Figure 2.8). Assuming that AB401 is near to a minimum temperature melt composition it is expected that for a particular aH₂O, quartz, plagioclase and K-feldspar crystallise simultaneously at a temperature close to the solidus. From the phase relations in Figure 2.2 this condition is realised at approximately 775°C and a melt H₂O content of ~3.5 wt. %. It has to be noted that this

temperature and water content correspond to the minimum temperature melt composition determined at $a_{H_2O} = 0.5$ and 200MPa by Holtz et al. (1992).

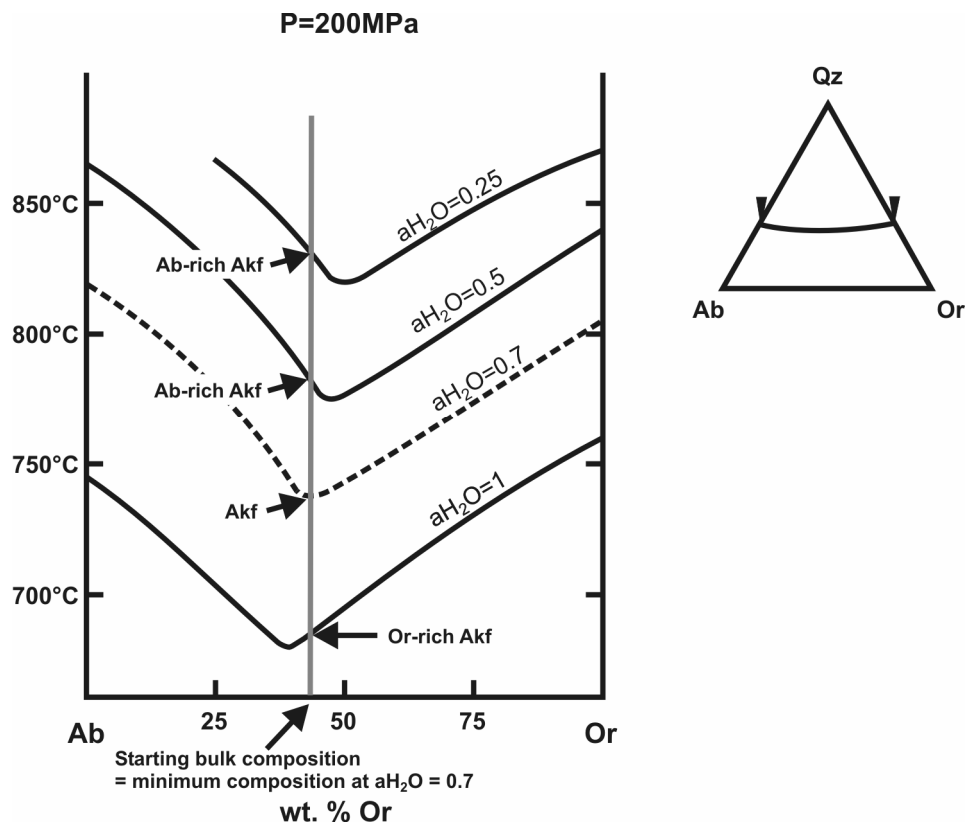


Figure 2.8: Section through the liquidus surface along the cotectic in the system Qz-Ab-Or-H₂O (redrawn after Holtz et al., 1992). Grey vertical line represent a bulk minimum temperature melt composition at $a_{H_2O} = 0.7$. In experiments at $a_{H_2O} < 0.7$ Ab-rich alkali-feldspar is the liquidus phase at high T. At $a_{H_2O} > 0.7$ Or-rich alkali-feldspar is the liquidus phase at low T.

2.5.3 Differentiation by fractional crystallisation

There are several possibilities to model the differentiation assuming that AB422, AB421 and AB401 derive from a parental magma AB412. First, the three felsic compositions can derive directly from AB412 assuming that the residual melts (with compositions AB422, AB421 and AB401) are removed after a certain crystal fraction was formed. Second, crystal fractionation could occur where crystals are chemically isolated from the coexisting melt after their formation. In this case, composition AB421 should derive from AB422 as the parent magma and AB401 from AB421. Third, the differentiation results from a combination of both processes.

AB422

In §1 the formation of AB422 was modelled considering a differentiation by crystal fractionation from AB412 by using experimentally determined phase relations and zircon saturation temperatures. Assuming a parental magma with a composition close to AB412 (King et al., 2001) SiO₂, Al₂O₃, FeO, MgO, CaO, Na₂O concentrations of AB422 can be reproduced after fractionation of 4.7 wt. % orthopyroxene and 8.5 wt % plagioclase. However, the residual of mass balance calculation for K₂O was higher than for all other elements (§1).

The comparison of AB422 with the composition of residual glasses from crystallisation experiments with AB412 can be used to determine the conditions at which AB422 can derive from AB412 (T, aH₂O, and phases involved in fractionation processes). At the appropriate conditions the residual melt composition from AB412 has to be identical to the bulk composition AB422. Figure 2.4a-e shows that it is improbable that AB422 can be generated by crystal fractionation from a parent magma close to AB412. Residual melt compositions of AB412 having K₂O contents similar to AB422 (~5 wt. %) are only observed at melt H₂O contents <3.5 wt. % (Figure 2.4e). However, at these H₂O contents the SiO₂ contents are systematically higher (~76 wt. %) than AB422 (Figure 2.4a). Thus, the high K₂O content of AB422 cannot be explained by a simple crystal fractionation process from AB412. Alternative models are proposed below (§2.5.6).

AB421

Using the same method as described above (comparison of experimental glass compositions with bulk compositions, Figure 2.4) the derivation of AB421 from AB412 or AB422 can be tested. The examination of Figure 2.4a-e shows that residual glasses from AB412 with SiO₂, Al₂O₃, FeO, CaO and K₂O concentrations corresponding to the bulk AB421 have only been obtained in experiments at temperatures between 900 to 850°C with 2 to 3 wt. % H₂O in the

melt. Thus, AB421 can derive from AB412 by crystallisation of magnetite, orthopyroxene and plagioclase according to the phase relations in this T-aH₂O range. Mass balance calculations show that the residual melt composition is close to composition AB421 after extracting 2.1 wt. % magnetite, 3.5 wt. % orthopyroxene and 13.1 wt. % plagioclase from AB412 (Model 1, Table 2.8). Zircon saturation temperature for AB421 is 806°C (Table 2.1) suggesting that biotite may participate to the fractionating phases (Figure 2.5). However, calculation with biotite (Model 2) show that this mineral would play a minor role (<0.5 wt. %) in fractionation processes leading to AB421. Calculations involving quartz and/or K-feldspar did not yield to satisfying results indicating that these minerals were not part of the fractionating assemblage.

The derivation of AB421 from AB422 can be tested by examining Figure 2.4f-k. The residual glass compositions of runs with AB422 do never fit the composition AB421 for all considered elements. The relatively low K₂O content of AB421 (4.66 wt. %), when compared to AB422 (4.95 wt. %), is only observed in runs with a melt H₂O content >4 wt. % (Figure 2.4k). In contrast the CaO content of 0.91 wt. % in AB421 is mainly determined at melt H₂O contents <4 wt. % (Figure 2.4s) except at 750°C, but at this condition the FeO contents of residual glasses are lower (≤1 wt. %) than AB421 (1.64 wt. %, Figure 2.4i). Thus, at the investigated conditions it was not possible to reproduce residual glasses from AB422 with compositions identical/close to AB421.

AB401

Following the same approach as above and using Figure 2.4a-e, it can be shown that AB401 can not derive directly from AB412. In particular the low FeO content of AB401 (0.93 wt. %) is only reproduced at temperatures ≤800°C. At these temperatures the K₂O content of AB401 (5.18 wt. %) is only observed in residual glasses at melt H₂O contents ≤3.5 wt. % (Figure 2.4e).

Table 2.8: Results of mass balance calculations for major element fractional crystallisation

Sample	Parent	Daughter	Calculated	Residual	Calculated	Residual	Subtracted Phases ¹	Source of composition	Fraction wt. %	
	AB412	AB421	Model 1	(r)	Model 2	(r)			Model 1	Model 2
wt. %										
SiO ₂	71.67	76.11	76.08	-0.03	76.10	-0.01	Mt	Run 35 ²	2.11	1.93
TiO ₂	0.55	0.15	0.28	0.13	0.30	0.14	Opx	Run 35	3.49	3.45
Al ₂ O ₃	13.49	12.84	12.81	-0.04	12.80	-0.05	Pl	Run 35	13.08	12.86
FeO	4.13	1.64	1.58	-0.05	1.60	-0.04	Bt	Run 33 ²	-	0.47
MnO	0.08	0.06	0.03	-0.03	0.03	-0.03			18.68	18.71
MgO	0.62	0.23	0.37	0.13	0.34	0.11				
CaO	1.96	0.91	0.93	0.02	0.96	0.05		Σr ²	0.047	0.042
Na ₂ O	3.45	3.40	3.43	0.03	3.44	0.05				
K ₂ O	4.05	4.66	4.73	0.07	4.68	0.02				
cH ₂ O ³	2.5		3.0		3.0					
Sample	AB421	AB401	Model 3		Model 4				Model 3	Model 4
wt. %										
SiO ₂	76.11	77.64	77.61	-0.03	77.62	-0.02	Opx	Run 72	-	0.40
TiO ₂	0.15	0.09	0.08	-0.01	0.10	0.01	Bt	Run 84 ²	3.33	2.90
Al ₂ O ₃	12.84	12.25	12.22	-0.04	12.24	-0.01	Pl	Run 85	13.49	13.40
FeO	1.64	0.93	0.89	-0.04	0.91	-0.02	Qz	Run 72	12.80	12.66
MnO	0.06	0.02	0.03	0.01	0.03	0.01	Kfs	Run 64	11.26	11.68
MgO	0.23	0.05	0.05	0.00	0.03	-0.02			40.89	41.05
CaO	0.91	0.54	0.49	-0.04	0.49	-0.05				
Na ₂ O	3.40	3.29	3.28	-0.01	3.27	-0.02		Σr ²	0.008	0.006
K ₂ O	4.66	5.18	5.15	-0.04	5.15	-0.04				
cH ₂ O ³	3.0		4.7		4.8					

¹Deduced from experimental phase relations (Figure 1.2 and 2.2)

²Due to small crystal size of Mt and Bt in experiments compositions are estimated considering good analyses of neighbouring charges at higher aH₂O. Mt in Run 35 was estimated with the composition of Run 1 and a decrease of Ti-Fe contents to FeO = 80 wt. % and TiO₂ = 10 wt. % to count for the effect of aH₂O. Biotite in Run 33 was estimated with the composition of Run 1 and a decrease of the XMg to 0.34. Biotite in Run 84 was estimated with Run 61 and a decrease of the XMg to 0.35. Note that this procedure was carried out to minimise the residuals and the effect on calculated modal proportions is less than 5%.

³Calculated change of water content after fractionation assuming an initial water content of 2.5 wt. % H₂O for AB412 (according to 2-3 wt. % H₂O see §1.5.1.).

However, the SiO₂ contents of these glasses are too low when compared to AB401 (77.64 wt. %; Figure 2.4a). The residual glass compositions of charges with AB421 are close to composition AB401 for all elements except for K₂O which is too low in most experiments (Figure 2.4l-p). In fact only runs saturated with respect to K-feldspar or close to saturation yield to glasses with high K₂O. This suggests that AB401 corresponds to a melt in equilibrium with K-feldspar in addition to quartz and plagioclase. This is further confirmed by the comparison of AB401 with the minima in the system Qz-Ab-Or-An-H₂O showing that this composition is close to a water undersaturated minimum temperature melt composition (see above). Considering that AB401 can not directly derive from AB412, its parental composition must be already relatively differentiated and can be assumed to be close to AB421. Mass balance calculation show (Table 2.8) that AB401 is obtained after extraction of 3.3 wt. % biotite, 13.5 wt. % plagioclase, 12.8 wt. % quartz and 11.3 wt. % K-feldspar from AB421 (Model 3). Calculation with orthopyroxene (Model 4) show that this mineral may play a minor role (<0.5 wt. %), if any, in fractionation processes leading to AB401, in agreement with the decreasing orthopyroxene stability field from AB421 to AB401 (Figure 2.6).

Table 2.9: Mineral/melt partition coefficients used for fractional crystallisation modelling

	Orthopyroxene 2)	Plagioclase 3)	Biotite 1)	K-feldspar 1)
Rb	0.01	0.011	4.1	2.4
Sr	0.01	4.04	0.29	4.5

1) Nash & Crecraft (1985); 2) Bacon & Druitt (1988); 3) Ewart & Griffin (1994)

Constraints from trace elements

The proportions of modelled mineral assemblages fractionating from AB412 to form AB421 and AB401 as deduced by the mass balance calculations (Table 2.8) can be tested using the trace element distribution of the Wangrah Suite. Rayleigh fractionation is a common method to

describe crystal fractionation processes based on trace element variations. Rb and Sr are useful trace elements to describe fractionation processes involving feldspars and biotite (for partition coefficients see Table 2.9). The composition of all available Wangrah Suite granites and the calculated fractionation trends (with mineral proportions given Table 2.8) are shown in Figure 2.9. The Rb and Sr concentrations of the Eastwood compositions (AB421) confirm that these granites can derive from fractionation following Model 1 and 2 (Table 2.8). The relatively low Rb contents of the Dunskeig granites can only be explained if fractionation of K-feldspar is also involved as confirmed by the trends corresponding to Model 3 and 4.

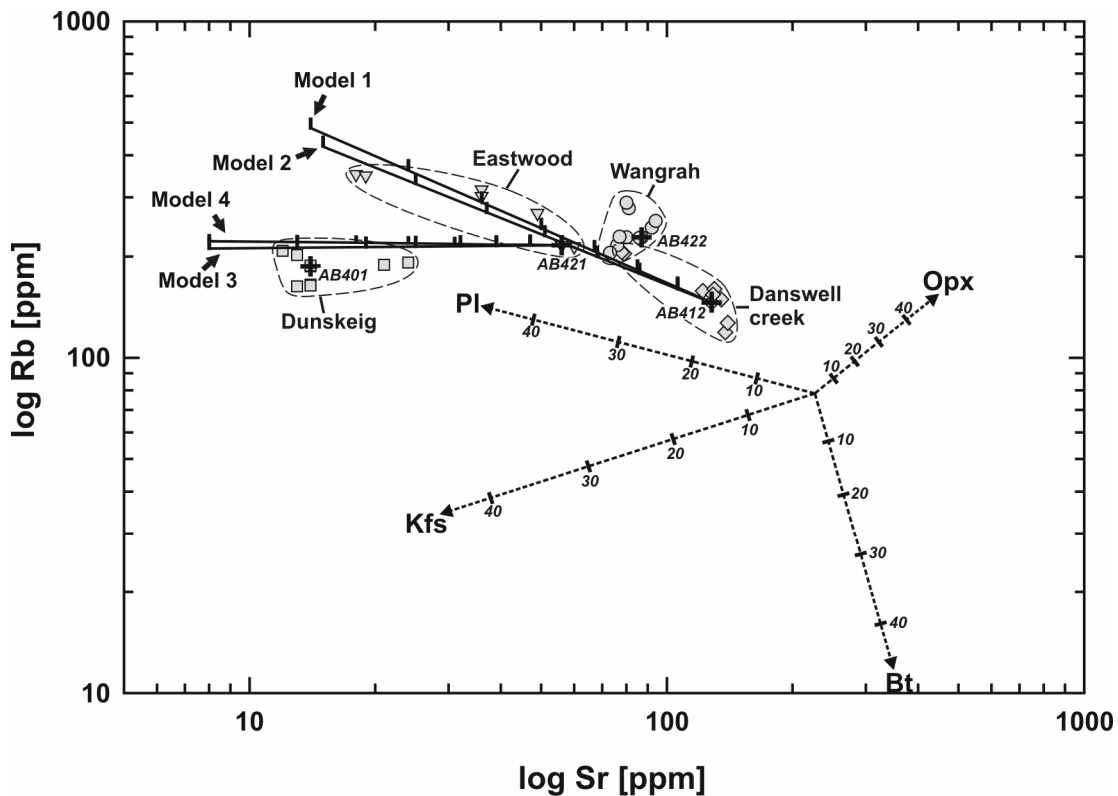


Figure 2.9: Rb versus Sr diagram (logarithmic scale) showing the variation of Wangrah Suite granite samples (source of data: King, 1992; King et al., 1997, 2001). Crosses: experimental studied compositions. Dashed vectors: Rayleigh fractionation trends for Pl, Kfs, Opx and Bt (partition coefficients for Rb and Sr are given in Table 2.9). Solid lines: Rayleigh fractionation trends for experimental determined phases (Model 1 to Model 4). Mass fractions are obtained by mass balance calculations (details in Table 2.8). Vertical marks indicate 10% fractional crystallisation.

2.5.4 Crystallisation and differentiation paths of the Wangrah Suite

As shown above, the compositions AB421 and AB401 can be derived by crystal fractionation from a parent magma close to AB412 and AB421, respectively. Thus, the Danswell Creek granite can be considered as a pluton crystallising from magmas which did not experience a significant fractionation (closed system equilibrium crystallisation) whereas the Eastwood granite may derive from fractionation of magmas similar to the Danswell Creek granite (the assemblages with early crystallised phases may be represented by the MGE). Similarly the Dunskeig granites may derive from magmas similar in composition to the Eastwood granite. For both, the Eastwood and Dunskeig granite a nearly closed system equilibrium crystallisation has to be assumed after separation as residual melts from the parent magma.

The crystallisation of each composition AB412, AB421 and AB401 can be described as a closed system crystallisation as it has been done previously for other granite plutons (e.g. Scaillet et al., 1997) using the experimentally determined phase proportions and the knowledge of the initial water content of the melts. The initial water content for AB412 has been constrained to be 2-3 wt. % with a liquidus temperature at 930°C (§1.5.1). Assuming an initial melt H₂O content of 2.5 wt. % of the primary magma (AB412) the water content increases with crystal fractionation to ~3 wt. % H₂O for composition AB421 (residual melt after crystallisation of 18.7 wt. % minerals) and ~4.7 wt. % H₂O for AB401 (residual melt after crystallisation of 40.9 wt. % minerals, Table 2.8). Such an initial water content for AB421 suggests a liquidus temperature of ~850°C. The An content of natural plagioclase core of An₂₅ in AB421 confirms the reliability of T-aH₂O of the melt at liquidus conditions (Figure 2.3a). The plagioclase compositions obtained in AB401 are not useful to check the water content of 4.7 wt. % H₂O. However, the liquidus temperature of AB401 is bracketed in the range 775 to 760°C for melt H₂O contents between 4 and 5 wt. %, respectively (Figure 2.2).

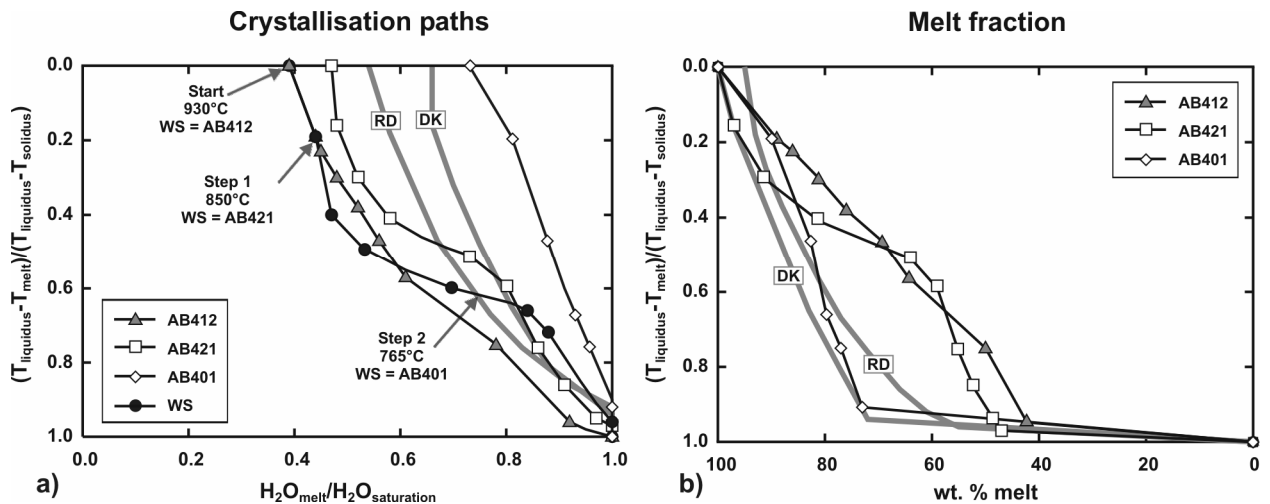


Figure 2.10: Comparison of a) changes of H_2O contents of the corresponding residual melts and b) changes in melt fraction (wt. %) of different granitic compositions during crystallisation. RD and DK after Scaillet et al. (1997). WS: Differentiation path of the Wangrah Suite with the change of H_2O content during crystal fractionation from AB412 (start) over AB421 (step 1) to AB401 (step 2). Note the rapid increase of H_2O over a small temperature range for AB421 and WS compared to the slight increase of H_2O for all other compositions.

The determined crystallisation paths for AB412, AB421 and AB401 are shown in Figure 2.5 and compared in Figure 2.10a. Assuming that H_2O behaves as an incompatible component during crystallisation, (H_2O incorporated in hydrous phases is negligible) the H_2O content of the melt increases with decreasing temperature due to crystallisation (Figure 2.5). The crystallisation paths obtained for AB412 and AB401 are characterised by a nearly linear increase of H_2O during cooling of the magma. In contrast the crystallisation path obtained for AB421 is characterised by a strong increase of H_2O with a factor of >1.5 in a small crystallisation interval of 20% of cooling (temperature interval of 0.4 to 0.6 on Figure 2.10a, corresponding to a temperature drop of 30°C). This strong increase in H_2O is related to the rapid increase of the crystal content due to the income of K-feldspar together with quartz and plagioclase in the crystallisation sequence (Figure 2.5). At temperatures close to liquidus and solidus conditions the water increase during crystallisation is comparable to AB412 and AB421.

The combination of the obtained crystallisation paths for AB412, AB421 and AB401 can be used to model the change of H_2O with temperature assuming a differentiation process starting

from AB412 and leading to AB401. This differentiation path is characterized by two steps at which the residual melt is chemically isolated from the crystals (Figure 2.10a). The first part of the crystallisation path corresponds to that obtained for AB412 because this composition is used as an analog for the parental magma composition with 2.5 wt. % H₂O at 930°C. After isolating (or removing) the crystals at 850°C the residual melt composition corresponds to AB421 and the water content is 3 wt. %. Thus, this chemical system would follow the crystallisation path obtained for AB421. When the water content of the residual melt reaches 4.7 wt. % H₂O at 765°C a second differentiation step is modelled. At this step the residual melt has the composition of AB401. Assuming that this melt is chemically isolated the crystallisation path will follow that of AB401.

The obtained differentiation path (WS; Figure 2.10a) is a combination of the individual crystallisation paths for AB412, AB421 and AB401. The beginning of cooling of the magma leads to small changes of H₂O over ~45% of the crystallisation interval (corresponding to a temperature drop of ~120°C), followed by a strong increase of H₂O by a factor of >1.5 in a small temperature interval of 15% of cooling (corresponding to a temperature drop of 40°C). As emphasized above, this strong increase in H₂O is related to the beginning of the concomitant crystallisation of K-feldspar, quartz and plagioclase in the crystallisation sequence. The last 35% of cooling (100°C) are again characterised by small changes in H₂O until water saturation is reached, slightly above the solidus.

The obtained crystallisation paths differ to crystallisation paths determined by Scaillet et al. (1997) for two different granites (Figure 2.10a), a biotite- muscovite bearing leucogranite (DK; after Scaillet et al., 1995) and a biotite-hornblende granite (RD; after Scaillet et al., 1994). Scaillet et al. (1997) proposed that the magmas of both granites are still composed of 70-80% melt after more than 80% of cooling (Figure 2.10b) due to crystallisation of small amounts of minerals over a large temperature range. This is also valid for the crystallisation path determined

for AB401 (74% melt near to the solidus) but in contrast to AB412 (70% melt after 50% of cooling, Figure 2.10b) and AB421 which can be explained in part by lower water activities at liquidus conditions. Scaillet et al. (1997) examined compositions with higher initial melt H₂O contents ($H_2O_{\text{melt}}/H_2O_{\text{saturation}} > 0.5$). Thus, small crystal proportions are expected at the beginning of cooling and more than 50% crystals are expected at water saturated conditions, in agreement with the results obtained for AB401 (Figure 2.10b). At lower initial H₂O contents ($H_2O_{\text{melt}}/H_2O_{\text{saturation}} < 0.5$), 50% crystals is obtained at higher temperatures and lower water contents of the melt (twice the initial H₂O content) as shown for AB412.

2.5.5 Viscosity of melts

The viscosity of granitic melts decreases with temperature and increases with dissolved H₂O (e.g. Shaw, 1972; Schulze et al., 1996, Johannes & Holtz; 1996) and the empirical model of Hess & Dingwell (1996) can be used to estimate changes in viscosity of the residual melts during cooling of AB412, AB421 and AB401 (initial water content of melts: 2.5, 3.0, 4.7 wt. H₂O, respectively). The calculated melt viscosities along the differentiation paths are always below 10⁶ Pas in a narrow range of 10⁵-10⁶ Pas. In Figure 2.11 calculated viscosities are plotted using dimensionless variables for sake of comparison. With cooling of the magma the viscosities of residual melts increase nearly linearly for AB412 and AB401. Just above the solidus the viscosities are increased by a factor of seven for AB412 and 2.5 for AB401 compared to the initial value. This evolution is similar to that calculated for a two-micas leucogranite (DK, 5.5 wt. % H₂O) and an A-type amphibole bearing granite (RD, 4.5 wt. % H₂O) using the data on phase relations of Scaillet et al. (1997) and the model of Hess & Dingwell (1996). It has to be noted, that the use of different models for viscosity calculation leads to slightly different results. Scaillet et al. (1997) calculated viscosities with the models after Shaw (1972) and Scaillet et al. (1996). For both compositions (RD and DK) Scaillet et al. (1997) determined a slight increase of

viscosity followed by a decrease below the initial value during cooling of the magma. Thus, the models used by Scaillet et al. (1997) predict slightly lower viscosities than the model of Hess & Dingwell (1996), especially in the last 40% of the cooling interval. However, the difference between the two models is not more than one log unit close to the solidus. Although there is no evidence for favouring one of the models, the model after Hess and Dingwell (1996) was applied for all data to compare the changes in viscosity with cooling of all compositions for sake of comparison.

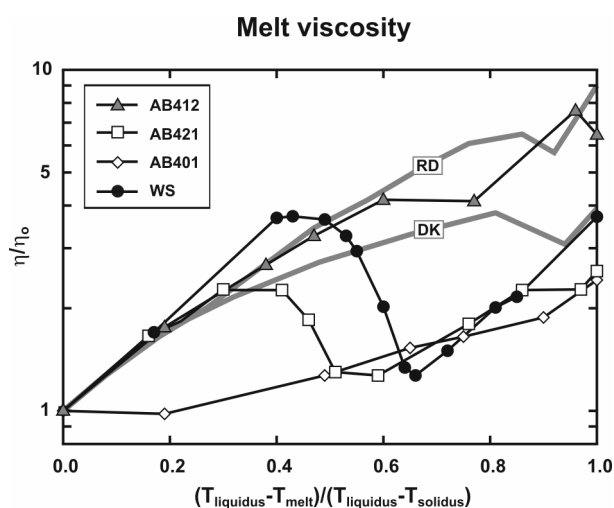


Figure 2.11: Relative changes in melt viscosity during crystallisation. Viscosity calculated after Hess & Dingwell (1996). η_0 is the initial viscosity of the melt. Note the decrease in melt viscosity close to η_0 for AB421 and WS compared to the nearly constant increase in melt viscosity for all other compositions.

In contrast to the other compositions, the viscosity of AB421 first increases by a factor of two at the beginning of the cooling interval (0-30% cooling), then decreases close to the initial value at 50% cooling, and finally increases again until the solidus is reached. The viscosity decrease of the residual melt between 30 to 50% cooling is due to the rapid change of H₂O content of the melt when K-feldspar becomes stable together with quartz and plagioclase (see above). A similar viscosity variation is observed for the two step differentiation path for the Wangrah Suite granites (WS, Figure 2.11) assuming that the crystals are chemically isolated (or removed) from the melt at 20% and 60% cooling (see above §2.5.4). However, the decrease of viscosity in the

cooling interval 40 to 60% is more pronounced than for AB421. Thus, rapid increase in melt H₂O contents during fractional crystallisation processes in a cooling magma can lead to a decrease of the viscosity of the residual melt especially if high amounts of crystals are formed over a small cooling range. Such conditions can be expected when the residual granitic melt reaches a composition close to a water undersaturated minimum temperature melt composition, which is only possible if the initial melts are strongly water undersaturated. It can be noted that this decrease in viscosity of residual melts would be even more pronounced using the model of Scaillet et al. (1996).

2.5.6 Crystallisation of the Wangrah Granite AB422

It has been shown that the Wangrah Granite AB422 can not be the result of simple crystal fractionation processes from a parent magma close to AB412 and that this composition is probably not along a fractionation trend connecting the compositions AB412, AB421 and AB401 (see §2.5.2). In addition the normative Qz-Ab-Or composition of AB422 can not simply be explained by plagioclase fractionation from AB412 (Figure 2.7b). The occurrence of idiomorph hornblende in the natural Wangrah Granite is not predicted from the experiments (hornblende did not crystallise from AB422; Figure 2.5; §1.5.4), suggesting that this composition can not be the result of equilibrium crystallisation process.

Hornblende crystallisation

In §1.5.4. it was suggested that the higher CaO of AB412 compared to AB422 may explain the stability of hornblende in experiments with AB412 and the lack of hornblende in experiments with AB422. In Figure 2.12 the CaO contents of glasses coexisting with hornblende from experiments with AB412 are compared with glasses of runs with AB422, AB421 and AB401 at the same temperatures and melt H₂O contents as a function of SiO₂ content of the glass. Without

exception, at a given SiO_2 content, the CaO contents of glasses coexisting with hornblende in AB412 are higher. As shown in Figure 2.12, the crystallisation of hornblende is not dependent on the CaO content of the melt only (SiO_2 may play a role) and FeO and MgO, also incorporated in hornblende, may influence the stability of hornblende. However, a systematic compositional dependence as shown for CaO could not be determined.

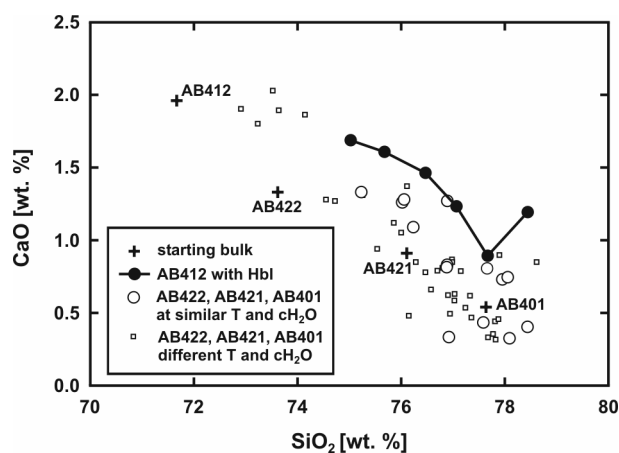


Figure 2.12: CaO versus SiO_2 (in wt. %) of experimental glass compositions. Black circles indicate experimental glasses of AB412 coexisting with hornblende. Open circles are experimental glass compositions of AB422, AB421 and AB401 at the same temperature and melt H_2O contents at which hornblende crystallisation was observed in AB412. Note that these glasses have lower CaO contents as experimental glasses coexisting with hornblende (solid line). Open squares represent glass compositions at different temperature and H_2O contents.

Figure 2.12 clearly show that, except AB412, none of the bulk compositions investigated is expected to lead to the crystallisation of magmatic hornblende. Thus, magmatic hornblende in the Wangrah Granite (AB422) must have crystallised from a melt composition with relatively high CaO contents (probably more mafic than the bulk AB422). This means that part of the minerals in AB422 were not in equilibrium with the surrounding melt at some stage of the magmatic history of the Wangrah Granite.

K₂O contents of granites and the role of magma mixing for the generation of the Wangrah Granite

As shown above (§2.5.3) the high K₂O content of AB422 cannot be explained by a simple crystal fractionation process from AB412. The relative high bulk K₂O content in the Wangrah granites (Figure 2.13, Table 2.1) when compared to the other Wangrah Suite granites are the result of the high K-feldspar content in these rocks. Another feature of the Wangrah Granite is the occurrence of two generations of quartz and local rapakivi-texture which can not be explained by the experimentally determined phase relations (Figure 2.5). The K₂O content of AB422 could result from an interaction of highly evolved partly crystallised K₂O-rich magmas (similar in composition to AB421 or AB401) with a less differentiated melt (AB412). This possible interaction is discussed considering the CaO and K₂O concentrations in granites and experimental glasses (Figure 2.13).

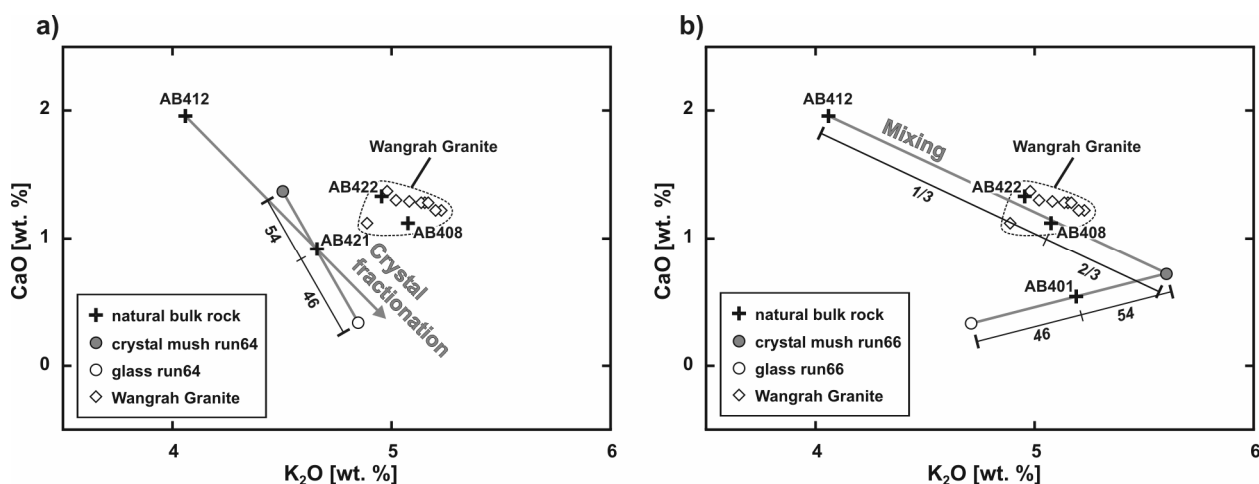


Figure 2.13: Comparison of experimental results of a) run 64 with AB421 at 750°C, 4.9 wt. % H₂O and b) run 66 with AB401 at 750°C, 5.1 wt. % H₂O in CaO versus K₂O diagrams (in wt. %). Numbers in italics indicate crystal/melt proportions in the run (Table 2.2).

Assuming that the highly crystallised K-rich magma is close in composition to AB421 or AB401 and saturated with respect to K-feldspar, the prevailing temperature in this magma should be below 760°C. Experimental products at 750°C and ~5 wt. % H₂O in the melt are

useful to discuss CaO and K₂O distribution between melt and crystalline phases in such highly crystallised magmas because they contain more than 50% crystals including K-feldspar (54 wt. % crystals in runs 64 and 66; Table 2.2).

Figure 2.13a-b shows the composition of the bulk crystalline phases and the residual glasses obtained after 54 wt. % crystallisation of AB421 (Figure 2.13a) and AB401 (Figure 2.13b) at similar conditions (750°C and ~5 wt. % H₂O in the melt). Compared to the bulk composition AB421 (4.66 wt. % K₂O and 0.91 wt. % CaO) the residual glass of run 64 (Figure 2.13a) is enriched in K₂O (4.85 wt. %) and depleted in CaO (0.33 wt. %; Table 2.6) and the composition of the bulk crystalline phases is depleted in K₂O (4.50 wt. %) and enriched in CaO (1.40 wt. %). Figure 2.13a shows that neither a mixing of crystalline phases nor of residual melt from AB421 with a less differentiated melt (AB412) can lead to the Wangrah Granites. In contrast to AB421 the compositions of the residual glass of run 66 (Figure 2.13b) show lower K₂O (4.70 wt. %) and CaO (0.33 wt. %; Table 2.7) contents than the bulk composition AB401 (5.18 wt. % K₂O and 0.54 wt. % CaO) and the bulk crystalline phase composition is enriched in K₂O (5.59 wt. %) and CaO (0.71 wt. %). The natural bulk Wangrah Granite compositions fall on a line connecting the bulk crystalline composition of run 66 and AB412 (Figure 2.13b) which may indicate that the Wangrah Granites result from a mixing/mingling of a less differentiated melt with crystals from a highly crystallised evolved magma with a composition similar to AB401. The proportions of crystals which are necessary to produce the Wangrah Granites vary between 50 to 70 wt. %. It can be noted that the Rb and Sr distributions are consistent with this mixing/mingling hypothesis for the generation the Wangrah granite (Figure 2.9).

One condition which needs to be required to produce AB422 by mixing/mingling processes as assumed above is a high proportion of K-feldspar in the crystalline assemblage. In case of AB401 and AB421 the proportions of K-feldspar in the solid assemblages is 50% and 39%, respectively (run 66 and 64; Table 2.2). This observation combined with the compositions of

melts and crystalline phases (Figure 2.13) suggest that the proportion of K-feldspar in the crystalline assemblage of AB421 was too low to allow the formation of AB422.

Interaction between high temperature melt and low temperature crystal mush: implications for Rapakivi-texture

Using chemical compositions and experimental constraints, the formation of the Wangrah granite requires a mixing/mingling event between a less evolved magma (probably at high temperature) and the crystal fraction of a low temperature K₂O-rich magma.

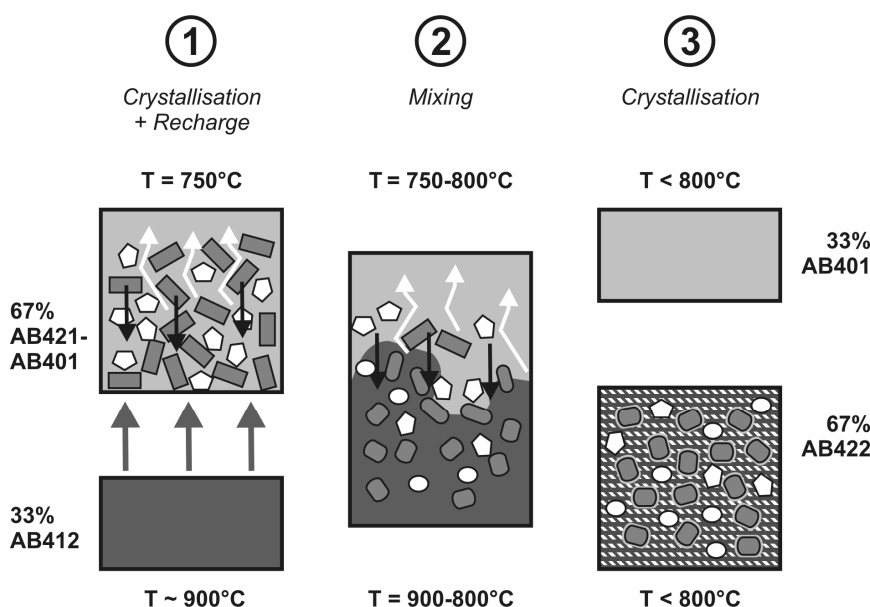


Figure 2.14: Three schematic diagrams illustrating the principle of mixing between high temperature magma (AB412) with low temperature partly crystallised magma (AB421-401) leading to AB22 and the formation of rapakivi-texture. Arrows indicate relative movements of melts (white arrows), crystals (black arrows) and high temperature magma (grey arrows). Grey squares: K-feldspar crystals; white polygons (quartz crystals). **Stage 1** “Crystallisation and Recharge”: A near minimum temperature melt magma composition with a composition between AB421 and AB401 is ~50% crystallised at 750°C leading to a K₂O enriched crystal mush (Figure 2.13, for simplicity only K-feldspar and quartz are mentioned here although plagioclase and biotite may be part of the crystal mush). Due to the higher densities of the crystals (>2.6 g/cm³) compared to the residual melt (<2.2 g/cm³, see Figure 2.15) and the high crystal content, the crystals may sink down and the residual melt is enriched to the top (filter pressing). In this magma system an intrusion of ~900°C hot magma from beneath with a composition of AB412 is assumed. **Stage 2** “Mixing”: If both magmas get into contact the temperature of the low temperature magma increases and K-feldspar and quartz start to dissolve (grey and white ovoids). The mixing temperature is ~800°C. Due to the low density of AB412 (<2.3 g/cm³) the crystals may sink in AB412 or the incoming melt AB412 displays the residual melt of the low temperature magma (percolation). **Stage 3** “Crystallisation”: The final crystallisation takes place in two distinct systems. The residual melt from the low temperature magma crystallises as a part of the Dunskeig granite, compositionally close to AB401. The high temperature magma crystallises along the crystallisation path of AB412 and forms the matrix between the K-feldspar and quartz phenocrysts. Plagioclase rims may crystallise on the K-feldspar ovoids (grey edge on grey ovoids) as the result of either plagioclase crystallisation from the matrix or reequilibration of K-feldspar. A second generation of quartz crystallises from the matrix (rapakivi-texture).

The exact mechanism leading to the segregation of the crystals from the residual melt in the low temperature magma is difficult to constrain and very difficult to produce via modelling (Couch et al., 2001) but may be related to the intrusion of the high temperature magma and to the physical properties of crystal mush (possibly filter pressing, density, viscosity). Although this mechanism can not be constrained from chemical properties of magmas a sketch illustrating the processes which must have occurred is shown in Figure 2.14. In the following the evolution of physical properties (viscosity and density) of melts and magmas assuming a mixing/mingling event between the crystalline assemblage of a partly crystallised magma (such as AB401) and a less differentiated melt (such as AB412) is examined in Figure 2.15. For simplicity in the following discussion this event will be described as “mixing”, although both mixing and mingling processes are involved.

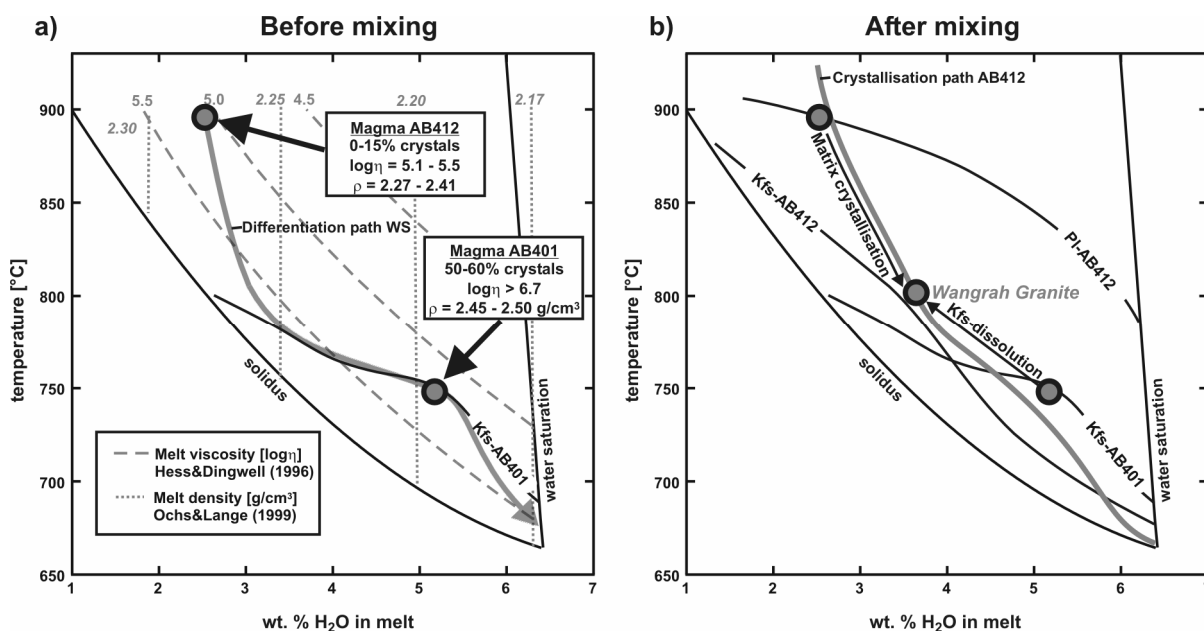


Figure 2.15: Temperature – melt H₂O content diagrams illustrating the physical and chemical conditions of high temperature magma AB412 and low temperature magma AB401 a) before recharge and b) during mixing. Melt densities were calculated after Ochs & Lange (1999). Because the compositional difference between residual melts of AB412 and AB401 are relative small the calculated melt densities are only influenced by the amount of dissolved water and vary between 2.30 to 2.17 g/cm³. Magma densities were estimated with the calculated modal proportions of melts and crystals (Table 2.2) and mineral densities of 3.80 (orthopyroxene), 5.00 (Ti-magnetite), 2.65 (plagioclase), 2.60 (K-feldspar), 2.65 (quartz) and 3.00 g/cm³ (biotite) after Deer et al., 1980. Magma viscosities were estimated using the Einstein-Roscoe equation with melt viscosities calculated after Hess & Dingwell (1996).

The physical properties of the two endmember magmas are shown on Figure 2.15a considering that AB412 is close to the liquidus (900°C) and that the crystal/melt proportion of AB401 is slightly above unity (conditions at 750°C, 200MPa and a melt H₂O content of ~5 wt. %, run 66; Table 2.2). The viscosity of the higher temperature magma is in the range 10^{5.1}-10^{5.5} Pas (0-15 % crystals, respectively) and is lower than that of the low temperature magma which is >10^{6.7} Pas (at crystal contents above 40%, the Einstein-Roscoe formula can not be applied, Lejeune & Richet, 1995). However, the melt viscosities of the high and low temperature magmas are almost identical in the range of 10^{5.0} to 10^{5.2} Pas. The densities of the high and low temperature magmas are 2.27 to 2.41 g/cm³ and 2.45 to 2.50 g/cm³, respectively.

Considering the extremely high viscosity of the low temperature magma, the similar viscosities and densities of high and low temperature melts, an injection of high temperature melt in a low temperature magma chamber will probably not lead to large scale convection processes (Couch et al., 2001) but may favour a percolation of high temperature melt through the crystal mush. In addition filter pressing may enhance the segregation of low temperature melt from the crystals. As discussed in §5.5 differentiation processes may lead to a decrease of melt viscosity in crystallising magmas which may facilitate filter pressing. The bulk density of the low temperature magma is also higher than that of the high temperature melt which may be an important factor for the initiation of whole scale sinking processes in the high temperature melt. This again would facilitate a percolation of high temperature melt through the crystal mush.

Assuming such a percolation of the high temperature magma in the low temperature magma chamber, the resulting temperature increase and the change of the surrounding melt composition lead to melting of part of the crystals, especially K-feldspar. Figure 2.15b shows that the K-feldspar is out of its stability field in composition AB401 if the temperature increases slightly. K-feldspar is also not stable in a bulk composition AB412 at ~800°C corresponding to a magma temperature after mixing of 33% high temperature magma with 67% crystals from low

temperature magma. This resorption of K-feldspar explains the ovoid shape of phenocrysts observed in the natural Wangrah Granite and the rapakivi-textures. The early crystallised quartz phenocrysts may also represent crystals inherited from the low temperature magma. The proportions of high temperature melt and crystals of 33 and 67%, respectively, are realistic considering that these proportions have been calculated for AB408 (Figure 2.13) and this granite show typical rapakivi textures.

The crystallisation of the high temperature melt (contaminated by dissolution products of the crystalline phases) can be described by the modelled crystallisation path for AB412 (Figure 2.15b). Plagioclase is the major phase crystallising from the melt and could crystallise as rims around the K-feldspar ovoids. The rapakivi-texture of the Wangrah granite is therefore attributed to magma mixing processes in agreement with several previous studies (e.g., Hibbard 1981). Another explanation for the plagioclase rims is that the K-feldspar in AB401 is richer in Ab component than those which would crystallise from AB412 (Figure 2.3b). After mixing the K-feldspar from the crystal mush could reequilibrate partially with the less evolved melt resulting in an Ab rich rim around K-feldspar ovoids (following a model similar to that proposed by Dempster et al., 1994).

Magma mixing processes as described above also explain the occurrence of hornblende in the Wangrah granite because the matrix melt composition AB412 contains the required amount of CaO for the crystallisation of hornblende after mixing (Figure 2.12). Such a mixing process explains also the occurrence of two generations of quartz; one crystallised from the high evolved melt AB401 as displayed by the quartz phenocryst, the other crystallised from the more mafic melt AB412 as part of the matrix crystallisation.

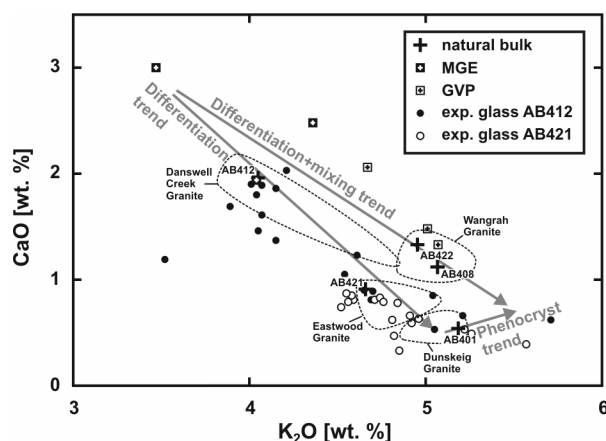


Figure 2.16: Comparison of natural Wangrah Suite granites and enclaves (MGE and GVP) with experimental glass compositions of AB412 and AB421 in the CaO versus K₂O diagram (in wt. %).

In this study all models are based on the assumption that AB412 (corresponding to the Danswell Creek granite) represent the parental melt. However, it is possible that slightly less evolved compositions may play a role in the differentiation history of the A-type granite Wangrah Suite. This possibility was not favoured previously due to the compositional differences and the low volume of rocks with less evolved compositions (King et al., 2001). The presence of microgranular enclaves (MGE) with lower SiO₂ and higher CaO (Figure 2.16) compared to the Danswell Creek Granite (Table 2.1) indicate that batches of more mafic magma were at least involved at some differentiation stages (e.g., Waight et al., 2000; Hibbard et al., 1981, 1981; Vernon, 1991). Successive mixing processes between high temperature melts and K-feldspar bearing crystal mush from high evolved low temperature magma may explain the formation of grey variable porphyry (GVP) enclaves with rapakivi-texture (Figure 2.16). Such enclaves may represent remnants of older mixing events in magma chambers, in which lower proportions of inherited crystals were involved or in which the high temperature melts were similar in composition to MGE.

2.6. Conclusions: Crystal fractionation vs. magma mixing

The investigation of chemical and physical properties of the Wangrah Suite granites suggests that the diversity of granite compositions result from interaction of two main processes, crystal fractionation and/or mixing/mingling of multiple granitic magmas.

AB412, a representative composition from the less evolved Danswell Creek Granite, is suitable as an equivalent of the parental magmas, as proposed by King et al. (2001), with an initial water content of 2.5 ± 0.5 wt. % H_2O . Fractionation of small amounts of magnetite, orthopyroxene and plagioclase (less than 20 wt. %) from AB412 leads to AB421, a composition representative for the Eastwood Granite. Further fractionation of greater amounts of biotite, plagioclase, quartz and K-feldspar from AB421 (approximately 40 wt. %) can lead to compositions such as the most evolved Dunskeig Granite (AB401). The modelled differentiation path from AB412 to AB421 to AB401 is consistent with the major and trace element distribution of the natural rocks. Assuming such crystal fractionation processes from a water undersaturated parental magma (AB412 with 2.5 ± 0.5 wt. % H_2O), it has been demonstrated that the residual melts evolve towards a water undersaturated minimum temperature melt composition (minimum in the system Qz-Ab-Or-An- H_2O). The fractionating mineral assemblage is dominated by the tectosilicates in the order of appearance (plagioclase \rightarrow quartz \rightarrow K-feldspar). The Eastwood and Dunskeig Granites are close in composition to a water undersaturated minimum temperature melt composition at a_{H_2O} between 0.5-0.7 under the prevailing experimental conditions (200MPa).

The crystallisation paths of such water undersaturated evolved magmas are characterised by a strong increase of crystal content over a small range of cooling at relatively high temperatures. Such magmas will become immobile at fairly high temperatures, approximately $70^\circ C$ above the water saturated solidus in the studied samples. In contrast, the residual melts become relative

mobile due to a rapid increase of the water content over a small cooling interval resulting in a decrease of viscosity.

The Wangrah Granite is enriched in K_2O compared to the other granites. This high K_2O content is not predicted from the experimentally determined differentiation trends. A systematic determination of phase relations and crystal/melt proportions of all Wangrah Suite granites clearly shows that the most dominant granite facies of the Wangrah Suite results from mixing processes between a high temperature A-type granitic melt and a highly crystalline low temperature magma. Only new input of high temperature felsic magma (recharge) in a magma chamber containing substantial amounts of K-feldspar (in addition to quartz and plagioclase) can lead to the high K_2O contents of the Wangrah Granite. This recharge process can also lead to the formation of rapakivi-texture.

The origin of the rapakivi-texture by magma mixing (as deduced in the case of the Wangrah granite) is in agreement with previous studies (e.g. Hibbard, 1981, 1991). The occurrence of enclaves in granites with rapakivi-texture underlines the role of a mixing event of felsic and mafic endmembers (Vernon, 1991; Turner & Foden, 1996; Waight et al., 2000; Baxter & Feely, 2002). Such mixing processes between felsic and mafic endmembers which may be genetically related to the granites have also been recognised as an important feature of many Lachlan Fold Belt S-type granites (Elburg & Nicholls, 1995). However, it is emphasised that bimodal magmatism (mafic-felsic) is not required for the formation of rapakivi-texture in the case of the Wangrah Suite. All discussed compositions including the enclaves are felsic (SiO_2 contents >67 wt. %) and are only distinguished in the degree of differentiation. In the Wangrah Granite the formation of rapakivi-texture is related to magmatic processes and not to subsolidus processes as proposed by Dempster et al. (1994). There is no evidence for assuming a pressure variation (ascent) to explain the rapakivi-texture in the Wangrah Granite. This is in contrast to decompression models for the formation of rapakivi granites as proposed by Nekvasil (1991) and

Eklund & Shebanov (1999). A complex structure of K-feldspar ovoids suggesting several resorption events (e.g., Eklund & Shebanov, 1999; Elliot, 2001) can easily be explained by multiple melt injections of primary magma in a differentiating and crystallising magma chamber at isobaric (emplacement) conditions.

3. References

- Anderson, J.L., and Bender, E.E. (1989): *Nature and origin of Proterozoic A-type granitic magmatism in the southwestern United States of America*. *Lithos*, 23, 19-52.
- Asrat, A., and Barbey, P. (2003): *Petrology, geochronology and Sr-Nd isotopic geochemistry of the Konso pluton, south-western Ethiopia: implications for transition from convergence to extension in the Mozambique Belt*. *International Journal of Earth Sciences*, 92, 873-890.
- Bacon, C.R., and Druitt, T.H. (1988): *Compositional evolution of the zoned calcalkaline magma chamber of Mount Mazama, Crater Lake, Oregon*. *Contribution to Mineralogy and Petrology*, 98, 224-256.
- Baxter, S., and Feely, M. (2002): *Magma mixing and mingling textures in granitoids: example from the Galway Granite, Connemara, Ireland*. *Mineralogy and Petrology*, 76, 63-74.
- Berndt, J., Liebske, C., Holtz, F., Freise, M., Nowak, M., Ziegenbein, D., Hurkuck, W., and Koepke, J. (2002): *A combined rapid-quench and H₂-membrane setup for internally heated pressure vessels: Description and application for water solubility in basaltic melts*. *American Mineralogist*, 87, 1714-1726.
- Bogaerts, M., Scaillet, B., Liegeois, J.P., and Vander Auwera, J. (2003): *Petrology and geochemistry of the Lyngdal granodiorite (Southern Norway) and the role of fractional crystallisation in the genesis of Proterozoic ferro-potassic A-type granites*. *Precambrian Research*, 124, 149-184.
- Burnham, C.W., Holloway, J.R., and Davis, N.F. (1969): *Thermodynamic properties of water to 1000°C and 10000 bars*. *Geological Society of America Special Paper.*, 132, 96pp.
- Chappell, B.W., White, A.J.R., and Wyborn, D. (1987): *The importance of residual source material (restite) in granite petrogenesis*. *Journal of Petrology.*, 28, 1111-1138.

- Chou, I.M. (1987): *Oxygen buffer and hydrogen sensor techniques at elevated pressures and temperatures*. In: Barnes, H.L. & Ulmer, G.C. (eds) *Hydrothermal Experimental Techniques*. New York: John Wiley, pp, 69-99.
- Clemens, J.D., Holloway, J.R., and White, A.J.R. (1986): *Origin of an A-type granite: experimental constraints*. *American Mineralogist*, 71, 317-324.
- Collins, W.J., Beams, S.D., White, A.J.R., and Chappell, B.W. (1982): *Nature and origin of A-type granites with particular reference to southeastern Australia*. *Contribution to Mineralogy and Petrology*, 80, 189-200.
- Conrad, W.K., Nicholls, I.A., and Wall, V.J. (1988): *Water-saturated and undersaturated melting of metaluminous and peraluminous crustal compositions at 10 kb: evidence for the origin of silicic magmas in the Taupo Volcanic Zone, New Zealand, and other occurrences*. *Journal of Petrology*., 29, 765-803.
- Couch, S., Sparks, R.S.J. and Carroll, M.R. (2001): *Mineral disequilibrium in lavas explained by convective self-mixing in open magma chambers*. *Nature*, 411, 1037-1039.
- Creaser, R.A., Price, R.C., and Wormland, R.J. (1991): *A-type granites revisited: assessment of a residual-source model*. *Geology*, 19, 163-166.
- Cullers, R.L., Stone, J., Anderson, J.L., Sassarini, N., and Bickford, M.E. (1993): *Petrogenesis of Mesoproterozoic Oak Creek and West McCoy Gulch plutons: an example of cumulate unmixing of a mid-crustal, two-mica granite of anorogenic affinity*. *Precambrian Research*, 62, 139-169.
- Dall'Agnol, R., Scaillet, B., and Pichavant, M. (1999): *An experimental study of a lower Proterozoic A-type granite from the eastern Amazonian craton, Brazil*. *Journal of Petrology*., 40, 1673-1698.
- Deer, W.A., Howie, R.A., and Zussman, J. (1980): *An Introduction to the rock forming minerals*. Longman Group lmt., London, pp 528.

- Dempster, T.J., Jenkin, G.R.T., and Rogers, G. (1994): *The origin of rapakivi texture*. Journal of Petrology, 35, 963-981.
- Devine, J.D., Gardner, J.E., Brack, H.P., Layne, G.D., and Rutherford, M.J. (1995): *Comparison of microanalytical methods for estimating H₂O contents of silicic volcanic glasses*. American Mineralogist, 80, 319-328.
- Eby, G.N. (1990): *The A-type granitoids: a review of their occurrence and chemical characteristics and speculations on their petrogenesis*. Lithos, 26, 115-134.
- Eklund, O., and Shebanov, A.D. (1999): *The origin of rapakivi texture by subisothermal decompression*. Precambrian Research, 95, 129-146.
- Elburg, M.A., and Nicholls, I.A. (1995): *Origin of microgranitoid enclaves in the S-type Wilson's Promontory Batholith, Victoria: evidence for magma mingling*. Australian Journal of Earth Sciences, 42, 423-435.
- Elliott, B.A. (2001). *Crystallization conditions of the Wiborg rapakivi batholith, SE Finland: an evaluation of amphibole and biotite mineral chemistry*. Mineralogy and Petrology, 72, 305-324.
- Emslie, R.F., and Stirling, J.A.R. (1993): *Rapakivi and related granitoids of the Nain Plutonic Suite: geochemistry, mineral assemblages and fluid equilibria*. Can Mineral, 31, 821-847.
- Ewart, A., and Griffin, W.L. (1994): *Application of proton-microprobe data to trace-element partitioning in volcanic rocks*. Chemical Geology, 117, 251-284.
- Frost, C.D., and Frost, B.R. (1997): *Reduced rapakivi-type granites: the tholeiite connection*. Geology, 25, 647-650.
- Frost, C.D., Frost, B.R., Chamberlain, K.R., and Edwards, B.R. (1999): *Petrogenesis of the 1.3 Ga Sherman batholith, SE Wyoming, USA: A reduced, rapakivi-type anorogenic granite*. Journal of Petrology, 40, 1771-1802.

- Haapala, I., and Rämö, O.T. (1992): *Tectonic setting and origin of the Proterozoic rapakivi granites of southeastern Fennoscandia*. Transactions of the Royal Society of Edinburgh, 83, 165-171.
- . (1999): *Rapakivi granites and related rocks: an introduction*. Precambrian Research, 95, 1-7.
- Hess, K.-U., and Dingwell, D.B. (1996): *Viscosities of hydrous leucogranitic melts: A non-Arrhenian model*. American Mineralogist, 81, 1297-1300.
- Hibbard, M.J. (1981): *The Magma Mixing Origin of Mantled Feldspars*. Contribution to Mineralogy and Petrology, 76, 158-170.
- . (1991): Textural anomaly of twelve magma-mixed granitoid systems. In: Didier, J., Barbarin, B. (eds), *Enclaves and granite petrology*. Elsevier, Amsterdam, pp 431-444.
- Holtz, F., Behrens, H., Dingwell, D.B., and Johannes, W. (1995): *Water solubility in haplogranitic melts. Compositional, pressure and temperature dependence*. American Mineralogist, 80, 94-108.
- Holtz, F., Johannes, W., Tamic, N., and Behrens, H. (2001): *Maximum and minimum water contents of granitic melts generated in the crust: a reevaluation and implications*. Lithos, 56, 1-14.
- Holtz, F., Pichavant, M., Barbey, P., and Johannes, W. (1992): *Effects of H₂O on liquidus phase relations in the haplogranite system at 2 and 5 kbar*. American Mineralogist, 77, 1223-1241.
- Housh, T.B., and Luhr, J.F. (1991): *Plagioclase-melt equilibria in hydrous systems*. American Mineralogist, 76, 477-492.
- James, R.S., and Hamilton, D.L. (1969): *Phase relations in the system NaAlSi₃O₈-KAlSi₃O₈-CaAl₂Si₂O₈-SiO₂ at 1 kilobar water vapour pressure*. Contribution to Mineralogy and Petrology, 21, 111-141.

- Johannes, W., and Holtz, F. (1996): *Petrogenesis and experimental petrology of granitic rocks*. Springer Verlag, 335 p.
- King, P.L. (1992): *A-type granites from the Lachlan Fold Belt: a case study and reassessment*. BSc (Hons) thesis, Australian National University, Canberra (unpubl.).
- King, P.L., Chappell, B.W., Allen, C.M., and White, A.J.R. (2001): *Are A-type granites the high temperature felsic granites? Evidence from fractionated granites of the Wangrah Suite*. Australian Journal of Earth Sciences, 48, 501-514.
- King, P.L., White, A.J.R., Chappell, B.W., and Allen, C.M. (1997): *Characterization and origin of aluminous A-type granites from the Lachlan Fold Belt, Southeastern Australia*. Journal of Petrology., 38, 371-391.
- Kretz, R. (1983): *Symbols for rock-forming minerals*. American Mineralogist, 68, 277-279.
- Landenberger, B., and Collins, W.J. (1996): *Derivation of A-type granites from a dehydrated charnockitic lower crust: evidence from the Chaelundi complex, eastern Australia*. Journal of Petrology, 37, 145-170.
- Le Maitre, R.W. (1979): *A new generalised petrological mixing model*. Contribution to Mineralogy and Petrology, 71, 133-137.
- Leake, B.E., Woolley, A.R., Arps, C.E.S., Birch, W.D., Gilbert, M.C., Grice, J.D., Hawthorne, F.C., Kato, A., Kisch, H.J., Krivovichev, V.G., Linthout, K., Laird, J., Mandarino, J., Maresch, W.V., Nickel, E.H., Rock, N.M.S., Schumacher, J.S., Smith, D.C., Stephenson, N.C.N., Ungaretti, L., Whittaker, E.J.W., and Youzhi, G. (1997) Nomenclature of amphiboles Report of the Subcommittee on Amphiboles of the International Mineralogical Association Commission on New Minerals and Mineral Names. European Journal of Mineralogy, 9, 623-642.
- Lejeune, A.M., and Richet, P. (1995): *Rheology of crystal-bearing silicate melts: an experimental study at high viscosities*. Journal of Geophysical Research, 100, 4215-4229.

- Loiselle, M.C., and Wones, D.R. (1979): *Characteristics and origin of anorogenic granites*. Geological Society of America, Abstracts, 11, 468.
- Lumbers, S.B., Wu, T.W., Heaman, L.M., Vertolli, V.M., and MacRae, N.D. (1991): *Petrology and age of the A-type Mulock granite batholith, northern Grenville Province, Ontario*. Precambrian Research, 53, 199-231.
- Martin, H., Bonin, B., Capdevila, R., Jahn, B.M., Lameyre, J., and Wang, Y. (1994): *The Kuiki peralkaline granitic complex (SE China): Petrology and geochemistry*. Journal of Petrology, 35, 983-1015.
- Naney, M.T. (1983): *Phase equilibria of rock-forming ferromagnesian silicates in granitic systems*. American Journal Sciences, 283, 993-1033.
- Nash, W.P., and Crecraft, H.R. (1985): *Partition coefficients for trace elements in silicic magmas*. Geochimica et Cosmochimica Acta, 49, 2309-2322.
- Nekvasil, H. (1991): *Ascent of felsic magmas and formation of rapakivi*. American Mineralogist, 76, 1279-1290.
- Patiño Douce, A.E. (1997): *Generation of metaluminous A-type granites by low-pressure melting of calc-alkaline granitoids*. Geology, 25, 743-746.
- Rajesh, H.M. (2000): *Characterization and origin of a compositionally zoned aluminous A-type granite from South India*. Geological Magazine, 137, 291-318.
- Robie, R.A., Hemingway, B.S., and Fisher, J.R. (1978): *Thermodynamic properties of minerals and related substances at 298.15 K and 1 bar (10⁵ pascals) pressure and at higher temperatures*. US Geological Survey Bulletin, 1452, 456pp.
- Scaillet, B., Holtz, F., and Pichavant, M. (1997): *Rheological properties of granitic magmas in their crystallization range*. In: Bouchez, J.L., Hutton, D.H.W. and Stephens, W.E. (eds.), Granite: from segregation of melt to emplacement fabrics, Kluwer Academic Publishers, Netherlands, pp. 11-29.

- Scaillet, B., Holtz, F., Pichavant, M., and Schmidt, M. (1996): *The viscosity of Himalayan leucogranites: implications for mechanisms of granitic ascent*. Journal of Geophysical Research, 101, 27691-27699.
- Scaillet, B., and Pichavant, M. (1994): *Phase relations of amphibole-biotite bearing granites. II: Effects of fO_2* . Terra Nova, 6, 42.
- Scaillet, B., Pichavant, M., and Roux, J. (1995): *Experimental Crystallization of Leucogranite Magmas*. Journal of Petrology, 36, 663-705.
- Schulze, F., Behrens, H., Holtz, F., Roux, J., and Johannes, W. (1996): *The influence of water on the viscosity of a haplogranitic liquid*. American Mineralogist, 81, 155-1165.
- Shaw, H.R. (1972): *Viscosities of magmatic silicate liquid: an empirical method of prediction*. American Journal of Science, 272, 870-893.
- Shaw, H.R., and Wones, D.R. (1964): *Fugacity coefficients for hydrogen gas between 0 and 1000°C for pressures to 3000 atm*. American Journal of Science, 262, 918-929.
- Sisson, T.W., and Grove, T.L. (1992): *Experimental investigations of the role of H₂O in calc-alkaline differentiation and subduction zone magmatism*. Contribution to Mineralogy and Petrology, 113, 143-166.
- Skjerlie, K.P., and Johnston, A.D. (1992): *Vapor-absent melting at 10 kbar of a biotite- and amphibole-bearing tonalitic gneiss: Implications for the generation of A-type granites*. Geology, 20, 263-266.
- . (1993): *Fluid-absent melting behavior of an F-rich tonalitic gneiss at mid-crustal pressures: Implications for the generation of anorogenic granites*. Journal of Petrology, 34, 785-815.
- Spulber, S.D., and Rutherford, M.J. (1983): *The origin of rhyolite and plagiogranite in oceanic crust: an experimental study*. Journal of Petrology., 24, 1-25.

- Turner, S.P., and Foden, J.D. (1996): *Magma mingling in late-Delamerian A-type granites at Mannum, South Australia*. *Mineralogy and Petrology*, 56, 147-169.
- Turner, S.P., Foden, J.D., and Morrison, R.S. (1992): *Derivation of some A-type magmas by fractionation of basaltic magma: An example from the Padthaway Ridge, South Australia*. *Lithos*, 28, 151-179.
- Vander Auwera, J., Bogaerts, M., Liegeois, J.P., Demaiffe, D., Wilmart, E., Bolle, O., and Duchesne, J.C. (2003): *Derivation of the 1.0-0.9 Ga ferro-potassic A-type granitoids of southern Norway by extreme differentiation from basic magmas*. *Precambrian Research*, 124, 107-148.
- Vernon, R.H. (1986): *K-feldspar megacrysts in granites – phenocrysts not porphyroblasts*. *Earth Sciences Review*, 23, 1-63.
- . (1991): Interpretation of microstructures of microgranitoid enclaves. In: Didier, J., Barbarin, B. (eds), *Enclaves and granite petrology*. Elsevier, Amsterdam, pp 277-292.
- Waight, T.E., Maas, R., and Nicholls, I.A. (2000): *Fingerprinting feldspars phenocrysts using crystal isotopic composition stratigraphy: implications for crystal transfer and magma mingling in S-type granites*. *Contribution to Mineralogy and Petrology*, 139, 227-239.
- Wark, D.A., and Stimac, J.A. (1992): *Origin of mantled (rapakivi) feldspars: experimental evidence of a dissolution- and diffusion-controlled mechanism*. *Contribution to Mineralogy and Petrology*, 111, 345-361.
- Watson, E.B., and Harrison, T.M. (1983): *Zircon saturation revisited: temperature and composition effects in a variety of crustal magma types*. *Earth and Planetary Science Letters*, 64, 295-304.
- Whalen, J.B., Currie, K.L., and Chappell, B.W. (1987): *A-type granites: geochemical characteristics, discrimination and petrogenesis*. *Contribution to Mineralogy and Petrology*, 95, 407-419.

Whitney, J.A. (1975): *The effects of pressure, temperature and XH_2O on phase assemblage in four synthetic rock compositions*. Journal of Geology, 83, 1-31.

Wyborn, D., and Owen, M. (1986) Araluen, N.S.W.- 1:100 000 Geological Map Commentary. Australian Government Publishing Service. Departement of Resources & Energy, and Bureau Mineral Resources, Geology & Geophysics. Canberra.

LEBENS LAUF

KEVIN KLIMM

PERSÖNLICHE ANGABEN:

- Anschrift: Lampestr. 2, 30449 Hannover
- Tel.: 0511 / 391204
- Geburtstag: 16. Dezember 1973
- Geburtsort: Kassel
- Familienstand: ledig
- Staatsangehörigkeit: deutsch

AUSBILDUNG/BERUF

1980 - 1984	Grundschule	Vellmar
1984 - 1990	Gesamtschule Ahnatal	Vellmar
1990 - 1993	Goethe - Gymnasium Abitur `93	Kassel
1993 - 1994	Zivildienst beim CVJM – Gesamtverband	Kassel
1994 - 2000	Studium der Mineralogie	Uni Hannover
02/2000	Diplom-Mineraloge Thema: „Schmelz- und Kristallisationsexperimente mit einer Amphiboltzusammensetzung“	
Seit 03/2000	Promotion und Wissenschaftlicher Mitarbeiter (FB Geowissenschaften)	Uni Hannover